PROCESSING AND MECHANICAL BEHAVIOR OF ULTRAFINE GRAIN MATERIALS

Thesis by
Mohit Kumar Jain

In Partial Fulfillment of the Requirements
for the Degree of Doctor of Philosophy

California Institute of Technology
Pasadena, California

1995
(submitted November 28, 1994)

to my grandparents

ACKNOWLEDGEMENTS

Looking back at my last five years at Caltech, I realize that I have had the good fortune of being in the company of some of the most brilliant, nice and helpful people I have ever met. I am grateful to them for playing an important role in my personal and professional growth.

My advisor, Dr. Tom Christman, was an unending source of inspiration, support and encouragement. His contagious enthusiasm and optimism kept me going during the difficult and frustrating times of my research. I am particularly grateful to him for being a caring mentor and for always being there to answer all my eccentric and often naive questions.

My research would have been of significantly inferior quality, if not for the help of Carol Garland. She helped me develop an appreciation for electron microscopy. I can't thank her enough for teaching me the systematic approach to research, for her ever willingness to share immense practical knowledge of electron microscopy and for her help in the interpretation of data. Furthermore, she was a good friend and was always willing to talk or listen.

I am far more grateful than a few words can express, to Prof. Ravichandaran for his kindness, friendship and generosity. I am thankful to Prof. T. Vreeland, Jr. and Andrew Mutz for building the Keck Dynamic Compaction Facility (a truly incredible piece of equipment) that made initiation of this research possible and for providing valuable insights into my research.

Several coworkers deserve my appreciation for various reasons: Barry Krueger, Kent Heady, Cho-Jen Tsai, Zheng Gao, Hugh Bruck, Yoshio Abe, Atakan Peker, Joe Holzer, Jürgen Eckert, Tab Stephens, Dale Conner, Charles Witham, Karina Montilla, Liubo Hong, Mo Li and Dave Lee for providing assistance in and around the lab and for innumerable stimulating discussions on various scientific issues. Dr. Channing Ahn for sharing his expertise and his help in the dark room and with the microscopy, Pam Albertson for the help in dealing with Caltech's beauracracy and Mo Li and Yoshio Abe for providing company during the many late hours spent in the lab.

I am thankful to Kannan Rangaramanujam, Ramana Murty, Neilay Dedhia, Ashish Bansal and Siddhartha Valluri, for being understanding roommates and good friends. I would also like to thank Dave Lee for being a good friend, for interesting me into the kind of food I never thought I would like and for familiarizing me with the intricacies of football and baseball. I am also thankful to him for carefully proofreading this thesis. I thank you all for providing the necessary distraction and keeping me from going insane.

I would not be where I am today without the support and sacrifices of my family, especially my grand parents, my uncle and aunt. I thank them for instilling in me the value of hard work and persistence, for their support and guidance and most of all for believing in me through all the disappointments.

This research would not have been possible without the financial support of Caltech Consortium in Chemistry and Chemical Engineering and National Science Foundation through grants DMR-9116570 and DMR-9396132. I am also thankful to Prof. Naresh Thadhani, Georgia Institute of Technology for his support and encouragement.

And finally, I would like to express my gratitude to God (if you exist) for giving me the opportunities and breaks so many other deserving people didn't get.

ABSTRACT

The mechanical behavior of ultrafine grain Fe-28Al-2Cr and 304 stainless steel was examined by conducting conventional mechanical testing and pre- and post-deformation microstructural characterization on bulk samples.

Shock wave consolidation was used to produce a fully-dense nanophase Fe-28Al-2Cr (grain size = 80 nm) intermetallic compound. In tension, the nanophase intermetallic failed in a brittle fashion with failure strength comparable to the coarse grain intermetallic of similar composition. However, the nanophase intermetallic yielded at 2.1 GPa during quasi-static compressive deformation and deformed to true strains greater than 1.4 without work hardening. The elastic-perfectly plastic behavior of nanophase Fe-28Al-2Cr is significantly different from that of coarse-grained intermetallic of the same composition, which yielded at 0.25 GPa and works hardened to $\approx$1.5 GPa before failure (at true strain of about 0.37). Microstructural examination before and after compressive deformation revealed that a significant portion of the microstructure refined to 10 nm grains surrounded by amorphous material. A similar grain refinement process was observed in 80 nm Fe-28Al-2Cr produced by ingot metallurgical technique.

A novel thermo-mechanical processing technique was developed for the production of a ultrafine grain 304 stainless steel (grain size = 200 nm). The key steps to this processing technique involved (1) formation of ultrafine dislocation cell structure, and (2) the conversion of dislocation cells into grains with medium to high misorientation by initiating grain boundary sliding in the microstructure. The ultrafine grain steel (grain size = 200

nm) was about six times stronger (σ_y = 1700 MPa) than coarse-grained steel of the same composition. Grain size hardening behavior of 304 stainless steel was also investigated over a broad range of grain sizes (200 nm to 200μm).

TABLE OF CONTENTS

LIST OF FIGURES

LIST OF TABLES

CHAPTER I

INTRODUCTION

Materials with fine microstructure are of great technological importance, because the mechanical properties of materials are known to improve with decreasing grain size. These properties include higher strength and better formability due to reduced superplastic temperatures.

The fine grain materials can be broadly categorized into three classes: (i) conventional fine grain materials with grain size ranging from 1–10 μm, (ii) sub micron grain materials or ultrafine grain materials with grain sizes ranging from 100 nm to 1 μm, and (iii) a relatively new class of materials called nanophase materials with grain sizes less than 100 nm.

Several powder and ingot metallurgical processing techniques exist for the processing of conventional fine grain materials in bulk form. Ridley [1] describes some of these techniques for a wide range of materials. However, processing of sub micron grain and nanophase materials in bulk form has proved to be a difficult task due to the highly metastable nature of these microstructures. As a result very little mechanical property data is available for materials with grain sizes finer than 1 μm. Therefore, the goals of this research was to produce nanophase and submicron grain microstructure in bulk materials and investigate the associated mechanical behavior of these materials.

1.1 Mechanical Properties

1.1.1 Strength

The yield strength of materials increases with decreasing grain size as grain boundaries

act as barriers to the motion of dislocations. An inverse square root dependence of the yield strength with grain size (Equation 1) is generally observed for most materials [2]:

$$\sigma_y = \sigma_o + \frac{k}{\sqrt{d}}, \quad (1)$$

where σ_y is the yield stress, σ_o is the frictional stress, k is a positive material constant and d is the grain size in the material. The dislocation pile up mechanism proposed by Hall and Petch is widely believed to adequately describe the hardening behavior of materials with decreasing grain size [3-5]. This mechanism predicts inverse square root dependence of yield stress on the grain size. However, the validity of the Hall-Petch relationship is not completely verified. Baldwin [6] has pointed out that the general scatter normally observed with the mechanical strength and grain size data, in many cases, gives equally good linear fit between σ_y and $d^{-\frac{1}{3}}$ or d^{-1} as with σ_y and $d^{-\frac{1}{2}}$. Several other mechanisms of grain size hardening exist that predict $d^{-\frac{1}{3}}$, $d^{-\frac{1}{4}}$ and d^{-1} dependence of yield strength on grain size [6-8].

1.1.2 Superplasticity

Superplasticity is a phenomenon in which polycrystalline materials exhibit large tensile ductilties. Superplastic deformation is generally observed in materials with fine and stable grain sizes at temperatures above 0.5 T_m. The empirical relationship between strain rate, stress, and grain size for materials exhibiting superplastic behavior is [1]:

$$\dot{\epsilon} = A\frac{DGb}{kT}(\frac{b}{d})^p(\frac{\sigma}{G})^n, \quad (2)$$

where $\dot{\epsilon}$ is the strain rate, A is a mechanism dependent constant, D is the appropriate temperature dependent diffusion constant, G is the shear modulus, T is the temperature, b is the burgers vector, d is the grain size, σ is the stress, p is a grain size exponent

that ranges from 1 to 3, and n is the stress exponent that also ranges from 1 to 3. Various theories have been proposed to explain this type of behavior [9]. In most cases a decrease in grain size results in lowering of superplastic temperature. This behavior is also predicted by most of the models of superplasticity.

1.2 Submicron Grain Materials

Traditionally, rapid solidification has been the most common method for the generation of ultrafine grain microstructures. These microstructures can be easily obtained in the form of powders or thin foils by rapidly quenching a wide variety of materials. Since powders and foils find little use in structural applications, the consolidation of these powders into bulk form is required. However, inevitable grain growth during powder consolidation by conventional techniques (as they require exposure of powders to high temperautures $> 0.6\ T_m$ for extended periods of time), makes retention of microstructure almost an impossible task. There are only a few instances reported in literature, where microstructure significantly finer than 1 μm were produced by traditional powder metallurgical techniques.

The ingot metallurgical techniques for the production of submicron grain microstructures in bulk materials are of special interest as they provide a cost efficient method of producing these microstructures without residual porosity. The absence of porosity is quite critical to good mechanical properties of materials. Valiev et al. [10-16] have demonstrated that equiaxed grain microstructures with grain sizes as fine as 100 nm can be produced in several metals and intermetallic compounds by subjecting them to large torsional strains (e $\approx$ 7) at room temperature. In some instances annealing at higher temperature after deformation is required to obtain these microstructures. Although, submicron grain microstructure can be produced in a wide variety of materials (Cu, Ni, Mg

alloy, Al alloy, Ni_3Al, Mo etc.) by this processing technique, the large strains required during processing severely limits the size of the product that can be processed by this technique. Moreover, most materials are incapable of sustaining such large deformations under normal conditions; therefore this processing needs to be carried out under large uniaxial pressures to prevent premature fracture, which further limits the size of the product.

We are aware of only two other ingot metallurgical techniques for production of materials with grain sizes substantially finer than 1 μm. These techniques are very material specific, i.e., they work for only a narrow class of materials. Nevertheless, they are quite important technologically as they require significantly less deformation in comparison to Valiev's technique.

Sherby's technique: This patented processing route [17-19] can yield equiaxed grain microstructures as fine as 500 nm in several ultrahigh carbon steels ($>$ 1.2% C). A typical processing would involve vaccum melting of an ultrahigh carbon steel (1.6 wt% C, 1.6 wt% Al, 0.6 wt% Mn, 1.5 wt% Cr and balance Fe). The as-cast billet is then annealed at 1150°C. This billet is hot rolled to a strain of 86.5% in eight passes as it cools from 1150°C to 850°C (i.e., above the A_1 temperature). The microstructure of the ingot at this point consists of pearlite colonies about 2-5 μm in size with an even distribution of pro eutectoid carbide particles within the pearlite matrix. The inter lamellar spacing in the pearlite colonies is about 100 nm. The ingot is further rolled about 40% in two passes below 780°C (i.e., below the A_1 temperature), while cooling to 680°C. The pearlite at this point is heavily deformed and consists of very high dislocation density, which provides a large driving force for spherodization. For spherodization, this billet is annealed at 750°C for 45 minutes followed by air cooling. This results in spherodization of carbide particles and formation of about 500 nm equiaxed grain microstructure with carbide

particles at the grain boundaries that restrict grain growth at high temperatures. This steel exhibits superplasticity at temperatures as low as 700^0C [17]. Similar techniques have been developed by Sherby et al. for other high carbon steel with slightly coarser microstructures [18,19].

Moore and Morris [20] have developed an aluminum alloy (Al-5wt%Ca-5wt%Zn) that contains about 20 vol.% $CaZnAl_3$ particles. An equiaxed grain microstructure as fine as 500 nm can be obtained in this alloy by recrystallization. The processing involves direct chill casting of this alloy with the average velocity of front about 1 mm/sec. The ingot produced in this manner was rolled to a strain of 95% at 500^oC and further cold rolled to a strain of 65%. The fine grain microstructure can be formed by annealing of this heavily deformed ingot.

Since the above mentioned techniques are very material specific, i.e., they work only for a very narrow class of materials, a need exists for the development of new techniques for the processing of these microstructures in other bulk materials. Motivated by some of our research on nanophase materials using shock wave consolidation techniques (described in Chapter 2 and 3), we have developed a processing technique for the formation of ultrafine grain microstructures in 304 stainless steel. This technique is based on the idea that misorientation among the dislocation subgrains can be increased by initiating grain boundary sliding among the subgrains.

1.3 Nanophase Materials

In the early eighties a novel vapor condensation technique ("cold finger technique") was developed by Birringer and Gleiter at University of Saarbrucken, Germany for the production of very fine (nano sized) particles [21]. With this technique it became possible to produce a new class of highly metastable materials known as nanophase materials

(polycrystals with grain size < 100 nm). Since then, other techniques such as, mechanical milling, electrochemical precipitation, biosynthesis etc., have been used to produce these materials. Gleiter [22,23] noted that a significant fraction of atoms (2 to 50%) in these materials are present at or in close vicinity of grain boundaries. As a result, these materials have been proposed, and in some cases shown, to possess different characteristics than their coarse-grained counterparts; including, decreased strength [21-23,8,9-11], increased strength [24-28], increased ductility [32,33], decreased ductility [25], increased diffusion kinetics [21-23,34], altered magnetic and electronic properties [21-23], etc. For recent reviews of nanophase materials see references [21-23]. The unique properties of these materials are considered to be a consequence of the small microstructural size scales and the large grain boundary volumes.

Nanophase materials are of particular interest for structural applications as it has been predicted and corroborated by initial reports that otherwise brittle materials such as intermetallic compounds and ceramics with nanophase microstructures, can exhibit significant ductility at ambient and near ambient temperatures [21]. The initial experiments by Karch, Birringer and Glieter [32] on the mechanical properties of these materials have reported significant amount of formability in CaF_2 and TiO_2 at 100°C and 180°C respectively. This is of tremendous technological importance as limited room temperature ductility has been one of the major obstacles to the introduction of intermetallics and ceramics in high temperature applications. In addition, significant improvement in strength has also been predicted for nanophase materials. However, this issue is the subject of considerable debate within the scientific community as the limited experimental data available regarding the mechanical strength of these materials is quite contradictory.

Predicting trends in mechanical properties for nanophase materials is difficult because some of the extrapolations from coarse-grained materials to their nanophase counter-

parts are contradictory. The contradictions exist because the extrapolations are based on different assumed local deformation mechanisms; e.g., dislocation motion and creep mechanisms. The presently available experimental results and theoretical developments have not been able to isolate clearly the active deformation mechanisms to resolve these apparent contradictions.

Predictions of increased strength and decreased ductility for nanophase materials result from dislocation pile-up mechanism (Hall-Petch) [3-5]. Nieman, Weertman and Siegel [25] have reported increased strength and decreased ductility in nanophase Cu and Pd at room temperature *during tensile deformation*, while Nieman, Weertman and Siegel [4], Hughes et al. [26], and Jang and Koch [27] have found increasing hardness with decreasing grain size. Several authors [24,25,35] have employed Hall-Petch mechanisms to explain these trends. *However, direct experimental evidence for dislocation motion in general and dislocation pile-up mechanisms in particular is absent* [24-27].

Decreased strength and increased ductility are predicted based on diffusive, or creep, mechanisms of deformation because of the shorter diffusion distances and the abundance of faster diffusion paths (grain boundaries)[21-23,29-33]. Chokshi et al. [29], Chang et al. [30], and Lu, Wei and Wang [31] reported decreasing hardness with decreasing grain size in nanophase materials. In addition, Karch et al. [32] have reported increased formability in nanophase CaF_2 and TiO_2 foils at 80 °C and 180 °C respectively, while Hahn et al. [33] have reported 60% ductility in 99% dense TiO_2 at 600 °C under far-field compression loading. Coble and other diffusive creep mechanisms have been used most often to explain these trends [36-39];

$$\dot{\epsilon} \propto \frac{\sigma}{d^n}, \tag{3}$$

where, n is a material constant between 1 and 3, $\dot{\epsilon}$ is the strain rate and σ is the applied stress. *However, as with the dislocation mechanisms cited above, clear microstructural evidence for any given creep mechanism is lacking.*

The determination of deformation mechanisms in nanophase materials has been hampered by several stubborn experimental problems. Primary among these problems is the production of fully-dense nanophase material of sufficiently large size to perform traditional mechanical characterization tests. This has led to experiments on porous material (up to 20% porosity in some cases) using samples that are too small for easy post-deformation microstructural examination [24-37,29-32]. In addition, some of the deformation experiments have been performed at conditions where densification and grain growth are occurring simultaneously during the test [33]. The coupling of deformation, densification and grain growth have made it difficult to interpret the macroscopic mechanical response observed in these experiments [33].

One of the goals of this research was to produce fully dense nanophase materials in sufficient quantity so that a better understanding of the deformation mechanism controlling the mechanical behavior of these materials with nanophase microstructures can be gained. Fe-28Al-2Cr was chosen as a candidate material for this study as there is a significant technological interest in enhancing the room temperature ductility of Fe_3Al based intermetallic compound. Conventional methods of powder consolidation cannot be employed for nanophase materials, because they involve high temperatures (at least $0.6T_m$, T_m = the melting temperature) for extended times. Exposure of nanophase powders to such high temperatures leads to significant grain growth that makes it difficult to retain a nanophase microstructure. Hence shock wave compaction technique was used to consolidate nanophase Fe-28Al-2Cr powders.

This thesis consists of six chapters. Chapter 2 primarily deals with synthesis of fully

dense nanophase Fe-28Al-2Cr intermetallic compound by shock wave consolidation and investigation of mechanical behavior of this material. In addition, operating deformation mechanisms in nanophase Fe-28Al-2Cr are explored. In Chapter 3, microstructure refinement observed in nanophase Fe-28Al-2Cr and Fe-28Al-5Cr is further explored in coarser grain microstructures and in nanophase microstructure that were obtained by ingot processing. In Chapter 4 a novel thermo-mechanical processing technique for the generation of ultrafine grain microstructures (grain size $\approx$ 200 nm) in 304 stainless steel is discussed, while chapter 5 explores mechanical behavior and operating deformation mechanisms in ultrafine grain 304 stainless steel at low and intermediate temperatures using compression experiments.

References

[1] N. Ridley, Mat. Sc. Tech. 6, 1145 (1990).

[2] R. W. Armstrong, Met. Trans. 1, 1170 (1970).

[3] E. O. Hall, Proc. Phys. Soc. London B64, 747 (1951).

[4] N. J. Petch, J. Iron Steel Inst. 174, 25 (1953).

[5] A. H. Cottrell, The Mechanical Properties of Matter, John Wiley & Sons, New York, NY, 282 (1964).

[6] W. M. Baldwin Jr., Acta Met. 6, 139 (1958).

[7] H. Conrad, Acta Met. 11, 75 (1963).

[8] L. Bragg, Nature 149, 511 (1963).

[9] J. W. Edington, K. N. Melton and C. P. Cutler, Prog. Mat. Sc. 21, 61 (1976).

[10] R. Z. Valiev, N. A. Krasilnikov and N. K. Tsenev, Mater. Sci. engng A137, 35 (1991).

11] N. A. Smirnova, V. I. Levit, V. I. Pilyugin, R. I. Kuznetsov, L. S. Davydova and V. A. Sazonova, Fizika Metall. 61, 1170 (1986).

[12] R. Z. Abdulov, R. Z. Valiev and N. A. Krasilnikov, J. Mater. Sci. Lett. 9, 1445 (1990).

[13] R. Z. Valiev, E. V. Kozlov, Y. F. Ivanov, J. Lian, A. A. Nazarov and B. Baudelet, Acta Met., 42, 2467 (1994).

[14] A. N. Vergazov, V. A. Likhachev and V. V. Rybin, Fiz. metal. metalloved., 42, 1241 (1976).

[15] R. Z. Valiev, A. V. Korznikov and R. R. Mulyukov, Mat. Sci. Engng., A168, 141 (1993).

[16] J. Langiullaume, F. Chmelik, G. Kapelski, F. Bordeaux, A. A. Nazarov, G. Canova, C. Esling, R. Z. Valiev and B. Baudelet, Acta Met., 41, 2953 (1993).

[17] O. D. Sherby, D. W. Kum, T. Oyama and J. Wadsworth, "Ultrahigh Carbon Steels Containing Aluminum", U.S. patent # 4,769,214 (September 6, 1988).

[18] O. D. Sherby, C. M. Young, B. Walser and E. M. Cady, Jr., "Superplastic Ultrahigh Carbon Steel", U.S. patent # 3,951,697, (April 20, 1976).

[19] O. D. Sherby and T. Oyama, "Ultrahigh Carbon Steel Alloy & Processing Thereof", U.S. patent # 4,533,390 (August 6, 1985).

[20] D. M. Moore and L. R. Morris, Mat. Sc. Engng., 43, 85 (1992).

[21] R. Birringer, Mat. Sc. Engg. A117, 33 (1989).

[22] H. Gleiter, Prog. Mat. Sci. 33, 223, (1989).

[23] H. Gleiter, Nanostructured Materials, 1, 1, (1992).

[24] G. W. Nieman, J. R. Weertman, R. W. Siegel, Scripta Met. 23, 2013 (1989).

[25] G. W. Nieman, J. R. Weertman, R. W. Siegel, Scripta Met. 24, 145 (1990).

[26] G. D. Hughes, S. D. Smith, C. S. Pande, H. R. Johnson, R. W. Armstrong, Scripta Met. 20, 93 (1986).

[27] J. S. C. Jang, C. C. Koch, Scripta Met. 24, 1599 (1990).

[28] T. G. Nieh, J. Wadsworth, Scripta Met. 25, 955 (1991).

[29] A. H. Chokshi, A. Rosen, J. Karch, H. Gleiter, Scripta Met. 23, 1679 (1989).

[30] H. Chang, H. J. Hofler, C. J. Altstetter, R. S. Averbach, Scripta Met. 25, 1161 (1991).

[31] K. Lu, W. D. Wei, J. T. Wang, Scripta Met. 24, 2319 (1990).

[32] J. Karch, R. Birringer and H. Gleiter, Nature 330, 10 (1987).

[33] H. Hahn, R. S. Averbach, Nanostructured Materials, 1, 95 (1992).

[34] S. Schumacher, R. Birringer, H. Gleiter, Acta Met. 37, 2485 (1989).

[35] T. G. Nieh, J. Wadsworth, Scripta Met. 25, 955 (1991).

[36] F. R. N. Nabarro, Bristol Conference on Strength of Solids, p. 75 (1948).

[37] M. F. Ashby, R. A. Verrall, Acta Met. 21, 149 (1973).

[38] R. L. Coble, J. Appl. Phys. 34, 1679 (1963).

[39] C. Herring, J. Appl. Phys. 21, 437 (1950).

CHAPTER II

SYNTHESIS, PROCESSING AND DEFORMATION OF BULK NANOPHASE Fe-28Al-2Cr INTERMETALLIC

2.1 Introduction

As mentioned in Chapter 1, predictions of significantly improved mechanical properties of nanophase materials (polycrystals with grain size less than 100 nm) are based on small microstructural size scales and large grain boundary volumes [1-3]. However, the available experimental evidence regarding the mechanical behavior of these materials is limited and often contradictory [4-13]. Furthermore, very little is known about the deformation mechanisms that control the mechanical behavior of these materials. The research effort in this area has been hampered by the problems with consolidation of nanophase materials due to the highly metastable nature of nanophase powders. Traditional powder metallurgical techniques of consolidation generally require exposure of powders to high temperatures ($> 0.6\ T_m$) for extended periods. It was initially believed that nanophase powders can be successfully consolidated by these techniques at much lower temperatures to avoid significant grain growth due to faster diffusion coefficients and smaller size scales in these materials. However, most of the efforts to produce fully dense and well bonded nanophase material by conventional powder consolidation techniques have been largely unsuccessful [4-7,9-12]. In addition, the "cold finger technique" is a slow process for production of nanophase powders. These problems have led to experiments on porous samples that are too small

to perform traditional mechanical characterization and pre- and post-deformation microstructural characterization. All these factors have made the interpretation of mechanical data and identification of the operating deformation mechanisms a difficut task.

These problems in the present investigation were overcome by producing nanophase powder by high energy ball milling and consolidation of these powders by shock wave compaction.

The production of powder precursors is a crucial step in the processing of nanophase materials. The nanophase powders for most previous mechanical studies were produced by the cold finger method pioneered by Gleiter et al. [1-3]. The rate of powder production by this route is slow and the nanometer size powder particles are subject to significant agglomeration that hinders consolidation. The present work uses high energy ball milling (mechanical attrition) to produce relatively large quantities of nanophase material with the powder size remaining at the micron size scale [17,18]. This technique has proven effective for the production of a wide variety of nanophase materials, e.g., [17,18].

Shock wave compaction was used in this study and is well suited for consolidation of powders with such metastable microstructures. The very large pressures present in shock waves can fully densify the compacts. Furthermore, the shock wave preferentially deposits energy at the particle boundaries where deformation and particle-particle bonding are required [19-23]. Since the interior of the particles remains relatively cold and the particle surfaces quench rapidly, alteration of the original metastable microstructure is reduced.

The aim of this research was to produce bulk, fully-dense nanophase materials for subsequent deformation studies. An intermetallic compound Fe-28Al-2Cr was

chosen, because there is a significant technological interest in enhancing the room temperature ductility of Fe_3Al based intermetallic compounds. Furthermore, Fe-28Al-2Cr intemetallic has limited room temperature ductility and good oxidation resistance. A limited amount of ductility is essential for recovery of compact after shock wave consolidation. In addition, significant amount of literature is available regarding the deformation of these alloys (for a review see reference [25]). Both tension and compression deformation and failure mechanisms are explored coupled with systematic x-ray and transmission electron microscope examinations. The results are interpreted in relation to previous work on nanophase metals and ceramics and available theories of grain boundary strengthening and superplasticity.

2.2 Experimental Procedure

2.2.1 High Energy Ball Milling

The coarse grained Fe-28Al-2Cr alloy powder (powder diameter = 50-100 μm) for this investigation was obtained from Idaho National Engineering Laboratory, Idaho Falls, ID. Nanophase microstructures were produced by high energy ball milling in a SPEX 8000 shaker mill. Preliminary studies of microstructural refinement were made by milling 8 gms of powder for 2, 4, 6, 8, 16, 36, 70 hrs. The grain size in the powder was monitored by the broadening of x-ray diffraction peaks (details of the procedure are discussed below). The grain size saturates after 8 hours of ball milling, and all the results presented in this chapter are for powder milled for 8 hours. For each ball milling operation, 8 gms of powder with 20 gms of hardened steel balls were sealed in a hardened steel vial. All powder handling and the ball milling were carried out in an argon glove box to minimize oxygen

contamination.

Contamination of the powder during ball milling was checked by chemical spectrographic methods. In addition, a small amount of as-milled Fe-28Al-2Cr powder was remelted in an arc-melter. Specimens for compression tests were made in the same manner as described below and are referred to in this report as "as-cast" material. The response of the as-cast material is compared to the results available in the literature for Fe-28Al-2Cr.

2.2.2 X-ray Diffraction and Electron Microscopy

X-ray diffraction (XRD) patterns were collected on an Inel CPS-120 diffractometer system using Co Kα radiation (λ = 1.7902Å) and a curved position sensitive detector (PSD) spanning 127^o in 2θ. The system consisted of a curved blade anode in flowing mixture of 85% Argon and 15% Ethane gas. A schematic of this diffractometer system is shown in Figure 2.1. An incident beam monochromator is used to remove K_β radiation and the system has an equivalent resolution of 0.03^o in 2θ. Grain sizes of the ball milled powders were determined by the analysis of x-ray peak broadening. The widths of diffraction peaks were calculated by fitting with a Lorentzian function. Grain sizes were computed by assuming that both the strain component as well as the grain size component of broadening are Guassian. The detailed procedure of this analysis is described in [17,24].

Microstructures of undeformed and deformed specimens were examined by transmission electron microscopy (TEM). Most of the samples for TEM were made by electro-jet-thinning at -25^{o}C in an 80% methyl alcohol and 20% perchloric acid solution at 12.5 volts and 66 milliamps. Additional TEM foils of the deformed specimens were made by ion milling. The ion milling was performed at -197^{o}C

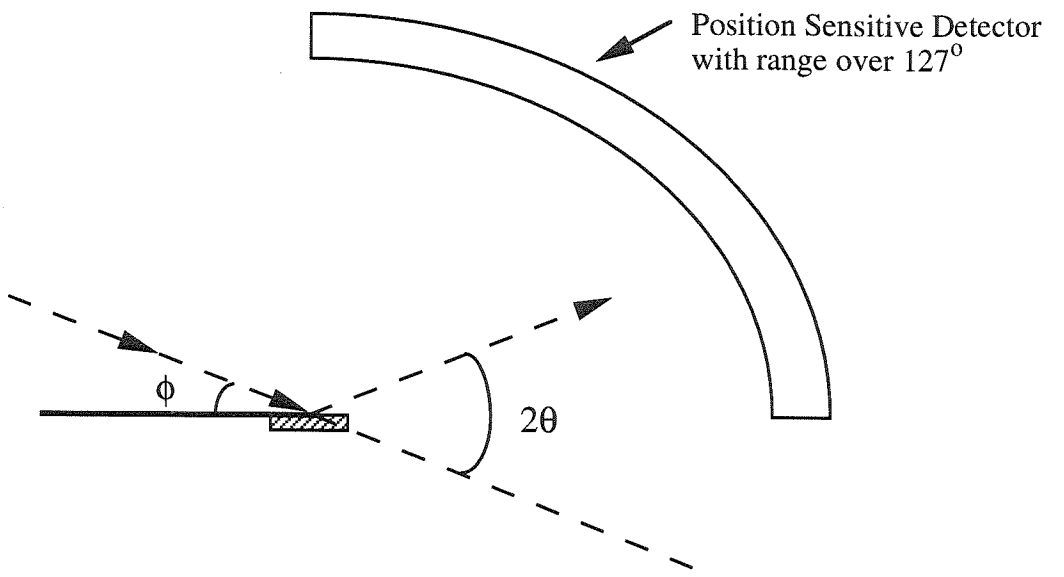

Figure 2.1 Schematic of Inel CPS-120 diffractometer system.

to minimize damage to the microstructure due to local heating. Most of the TEM samples of the deformed material were oriented with the loading direction perpendicular to the foil. Two foils with the loading direction in the plane of the foil were prepared by ultramicrotomy to characterize the morphology of the deformed grains. After thinning, the foils were stored in methyl alcohol to minimize surface oxidation. TEM studies were performed on a Philips EM430 and Philips EM301 microscopes operating at 300 and 100kV respectively.

The fracture surfaces of the specimens failed in tension were examined on a Hitachi HHS–2R scanning electron microscope.

2.2.3 Shock Consolidation

Shock consolidation of the nanophase powders was performed using the Keck Dynamic Compaction Facility that uses a 3m long and 35 mm diameter (ID) cannon barrel. A 31.5 mm diameter flyer plate carried by a nylon sabot is accelerated

in the evacuated barrel and impacts the powder sample. The smokeless shotgun powder (nitrocellulose) that was ignited by electrically heated tantalum wire was used to generate propellant gas. The flyer plate acceleration is essentially complete within the first 2m of the barrel. The velocity of the flyer plate is measured by timing the interval between interruption of two light beams 4.035 cm apart shining across in the barrel extension that is screwed to the end of the barrel. Two optical cable carry light from a tungsten filament lamp to the barrel extension and shine it on the receiving fibers that are located opposite to the incident light cables in the barrel extension. The receiving fibers are connected to light activated switches. A CIRCUITMATE universal counter UC10 is used to count the cycles during the interval one switch is closed and the other is open.

The sample is contained in a hardened steel target connected to the end of a barrel through the barrel extension. A schematic of the flyer plate and target assembly is shown in Figure 2.2. A nearly one-dimensional shock wave, and therefore well defined shock conditions, are generated in this manner. The distance between the powder that is to be impacted and the light beams that are used to measure flyer plate velocity is less than 6 inches. Hence measured velocity is very close to the impact velocity.

A maraging steel (Vascomax 350) sleeve containing gunpowder and ignition wire screws to the breach block and fits closely into the breech. The barrel is sealed from the breech by the sabot and hence the gunpowder is not evacuated with the barrel. The breech is shrink-fit into the breech reinforcements and is under compressive load. Both breech and the breech reinforcements are made of C300 maraging steel.

The recovery system is designed to decelerate the target in a controlled manner

and consists of momentum trap, industrial and automotive shock absorbers. The momentum trap consists of one aluminum plate 3 inch in diameter and two inches in length and two steel plates 3" in diameter and 0.75" in thickness. The three plates are screwed togather and the aluminum plate is separated from the steel plates by 1/4" thick sheet of rubber. The momentum trap is held between the target and industrial and automotive shock absorbers, respectively.

For adequate recovery of the compact, the release wave, which originates from the rear of the flyer plate should overtake the initial shock wave within the sample. Beyond this crossover point the powder is effectively consolidated by the nylon sabot and is mostly unbonded. Since the sample containment fixture is not impacted, the pressure at the sample edges releases radially in the sample and the containment fixture. This produces no increase in pressure or shock energy due to the "wrap around" waves that occur when the powder as well as the target fixture is impacted. This design enables adequate recovery of compacts without cracks.

The end of the barrel, barrel extension, target and the recovery system is housed in a recovery tank. The recovery tank is evacuated prior to firing to prevent noise from escaping from the tank. This also helps in achieving a better vacuum in the barrel. Since a good vacuum is hard to achieve in the recovery tank, separate vaccum system is used for the barrel from that of the recovery tank. The barrel and the powder are typically evacuated to less than 50 mtorr.

The ball milled powder was pressed in the cavity of the target to 30,000 lbs. The relative density of the green compact (before compaction) was 54.7% of bulk. A 5 mm thick 303SS flyer plate was employed for the compaction. This compaction was done with a flyer plate velocity of 1.25 Km/sec. Flyer plate velocity was measured just before impact by timing the interruption of two light

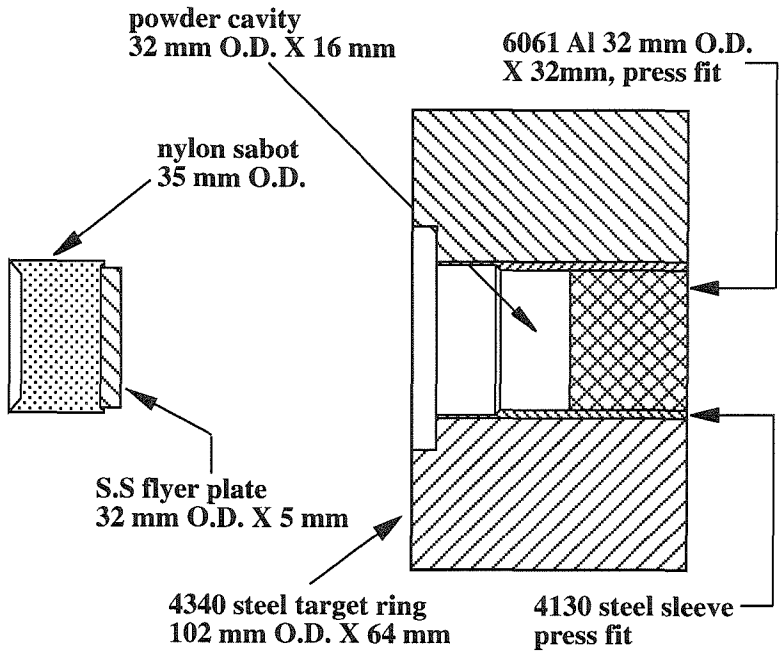

Figure 2.2 Target fixture and flyer plate assembly used in the shock consolidation. Note that only the sample, and not the containment assembly, is impacted.

beams separated by 40.35 mm. Prior to impact, the barrel and the target were purged with argon and then evacuated to 0.025 torr. Density measurements were performed on the compact and a cast alloy of the same composition by weighing the samples in toluene and air. A more detailed description of the facility and procedures used can be found in [20-22].

2.2.4 Mechanical Testing

For tensile tests, "dog-bone" shaped specimens, Figure 2.3(b), were cut from a strip parallel to the shock direction by electro-discharge-machining (EDM). Before testing, the flat sides of the tensile specimens were polished down to 6 μm using diamond paste. These specimens were pulled to failure in a fixture

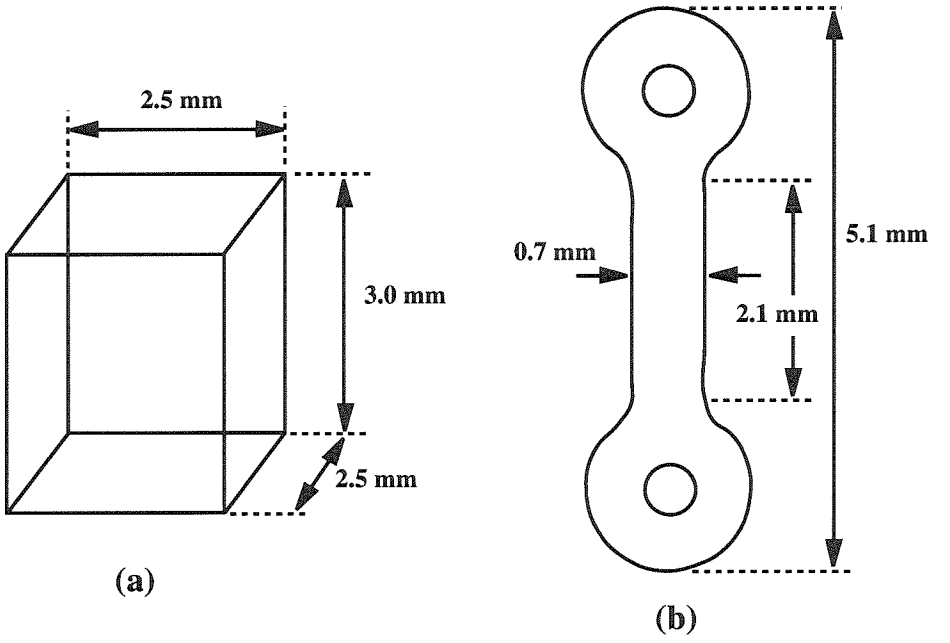

Figure 2.3 Sample geometries used for the compression (a) and tension (b) testing. The compression samples were cut with a diamond saw and all surfaces were polished to 600 grit emery paper. The tension samples were EDM and polished with 6 μm diamond paste.

designed to minimize bending stresses [22]. Compression testing was performed on almost cubic specimens cut by a diamond saw, Figure 2.3 (a). All surfaces of the specimens were polished with 600 grit emery paper. The specimens were sandwiched between two WC blocks and then compressed at a cross head speed of 0.02 in/min on an Instron model 4204 load frame. The tests were stopped at a true strain $\approx$ 1.4 (engineering strain $\approx$ 0.75) because the load required for further deformation exceeded the capacity of the load frame. Plastic strain was obtained by unloading the sample and measuring its height at various intervals during the test. The tensile tests were repeated 5 times and the compression tests about 10 times. The results reported are averages of these tests and the scatter in the results is less than 5%.

2.3. Experimental Results

2.3.1 Ball Milling Results

The X-ray diffraction peaks for Fe-28Al-2Cr alloy continue to broaden with ball milling for up to 8 hours and saturate thereafter. Characteristic x-ray diffraction patterns for the as-received and as-milled powders are shown in Figure 2.4. This figure demonstrates that there are no crystal structure changes occurring during processing and is an example of the data used in the line broadening analysis. The grain size determined by x-ray line broadening in the powder ball milled for 8 hours was $\approx$ 16 nm. Contamination of the powder during ball milling and powder handling was minimal (Fe content increased $\approx$ 1%, C content increased $\approx$ 0.16%, and O content increased $\approx$ 0.18%).

2.3.2 Shock Consolidation Results

A disc 32 mm in diameter and $\approx$ 10 mm in thickness was obtained after shock consolidation (one half of the compact is shown in Figure 2.5). A polished cross-section (parallel to the shock direction) of the compact was examined by optical microscopy for residual porosity. No evidence of porosity was found at magnifications up to 400$\times$. The density of the compact as measured by the Archimides method was found to be 6.546 gm/cm^3. This density is more than 99.9% of the as-cast alloy of the same composition, whose density (measured by the same method) was 6.550 gm/cm^3.

Only the top $\approx$ 6 mm of the compacted disc was found useful. The tensile samples made out of the bottom part of the compacted disc failed at a very low stress (less than 100 MPa). This suggests that the release wave caught up to the shock wave about 6 mm into the compact. Beyond 6 mm the powder was

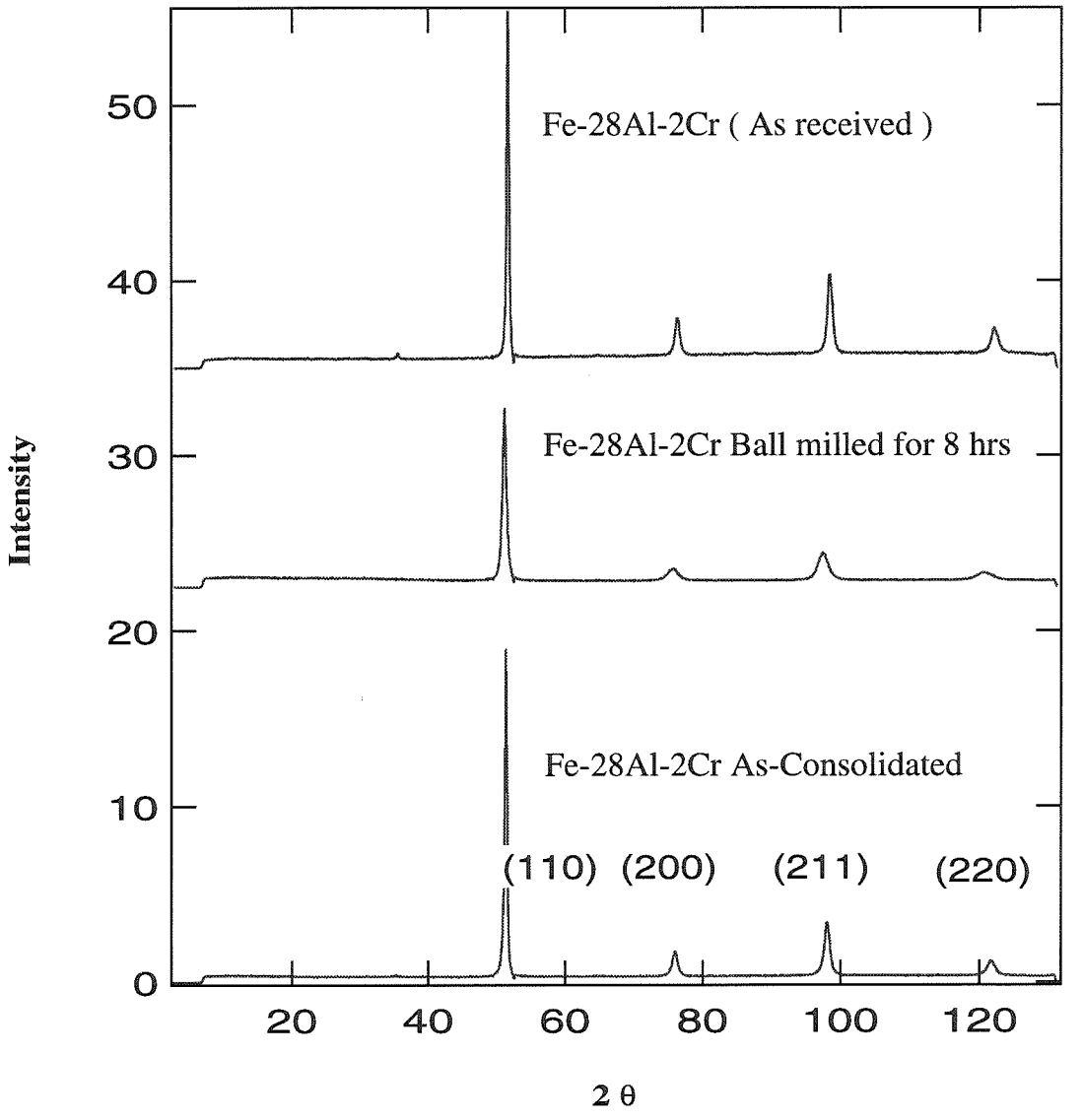

Figure 2.4 X-ray diffraction patterns for the as-received powder, the as-milled powder, and the as-consolidated material. X-ray line broadening analysis gives a grain size of $\approx$ 16 nm for the as-milled powder.

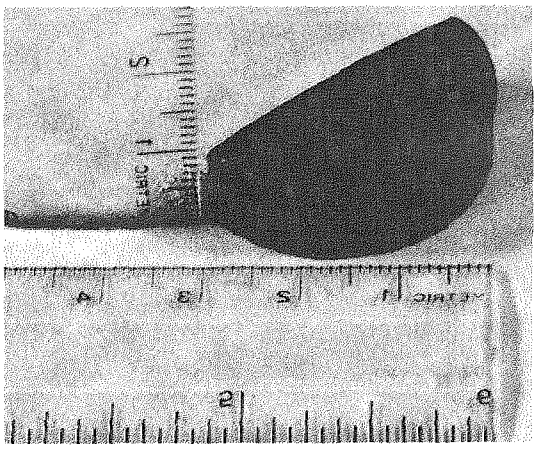

Figure 2.5 Picture of a cross-sectioned compact. The top surface was impacted by the flyer plate. No evidence of porosity was observed by optical or electron microscopy techniques.

effectively consolidated by the nylon sabot and was therefore not fully bonded. All the further mechanical testing and microstructural characterization described in this chapter was performed on samples derived from the top 6mm of the shocked compact.

2.3.3 As-Consolidated Microstructure

Typical dark and bright field TEM images of the as-consolidated microstructure are shown in Figure 2.6. The grains are equiaxed and the grain size distribution ranges from 60 to 120 nm with an average grain size of $\approx$ 80 nm. No evidence of texture was found in the shocked compact as foils perpendicular and parallel to the shock direction revealed similar microstructures. The (001) superlattice peak in the x-ray diffraction pattern (not easily distinguished at the scale shown in Figure 2.4) of the shocked Fe-28Al-2Cr indicates the presence of order in the microstructure. No evidence of porosity was observed and no evidence of a dissimilar powder-powder boundary was seen. 6 TEM samples were examined in this condition.

The dislocation density appeared to be "low" in this microstructure; however, as discussed in Section 4, quantitative determination of dislocation densities in these ultrafine microstructures is difficult. For the remainder of this report, the as-consolidated microstructure will be refered to as Type A.

2.3.4 Deformation Behavior

In tension this material could not sustain any plastic deformation and failed in the elastic region of the stress strain curve. The stress required for failure in tension was 0.65 GPa and the fracture surface has the conchoidal topology characteristic of grain boundary fracture, Figure 2.7. It is noteworthy that the failure strength of the nanophase Fe-28Al-2Cr is comparable to the ultimate tensile strength of the corresponding coarse grained alloy (0.64 GPa) that is known to fail by intergranular mechanisms. In addition, the powder size (50 - 1000 μm) is approximately that traditionally found for the as-cast grain size. This suggests that the mode of failure is interparticle decohesion (powder-powder debonding). This is not surprising, because it is unrealistic to expect an interparticle strength superior to that of the cast grain boundary strength. Details of the fracture process on the size scale of the grain size cannot be determined from the experiments performed.

In compression the nanophase Fe-28Al-2Cr alloy yielded at 2.1 GPa and did not fail even after true plastic strains of $\approx$ 1.4. The true stress-true plastic strain curves are shown in Figure 2.8 and the inset is a photograph of a specimen before and after deformation. Also shown in Figure 2.8 is the as-cast alloy that yielded at 0.27 GPa and continued to strain harden until failure at a true plastic strain of 0.3. A specimen was considered to have failed when cracks were visible by the naked eye away from the sample edges. The as-cast results of the present study

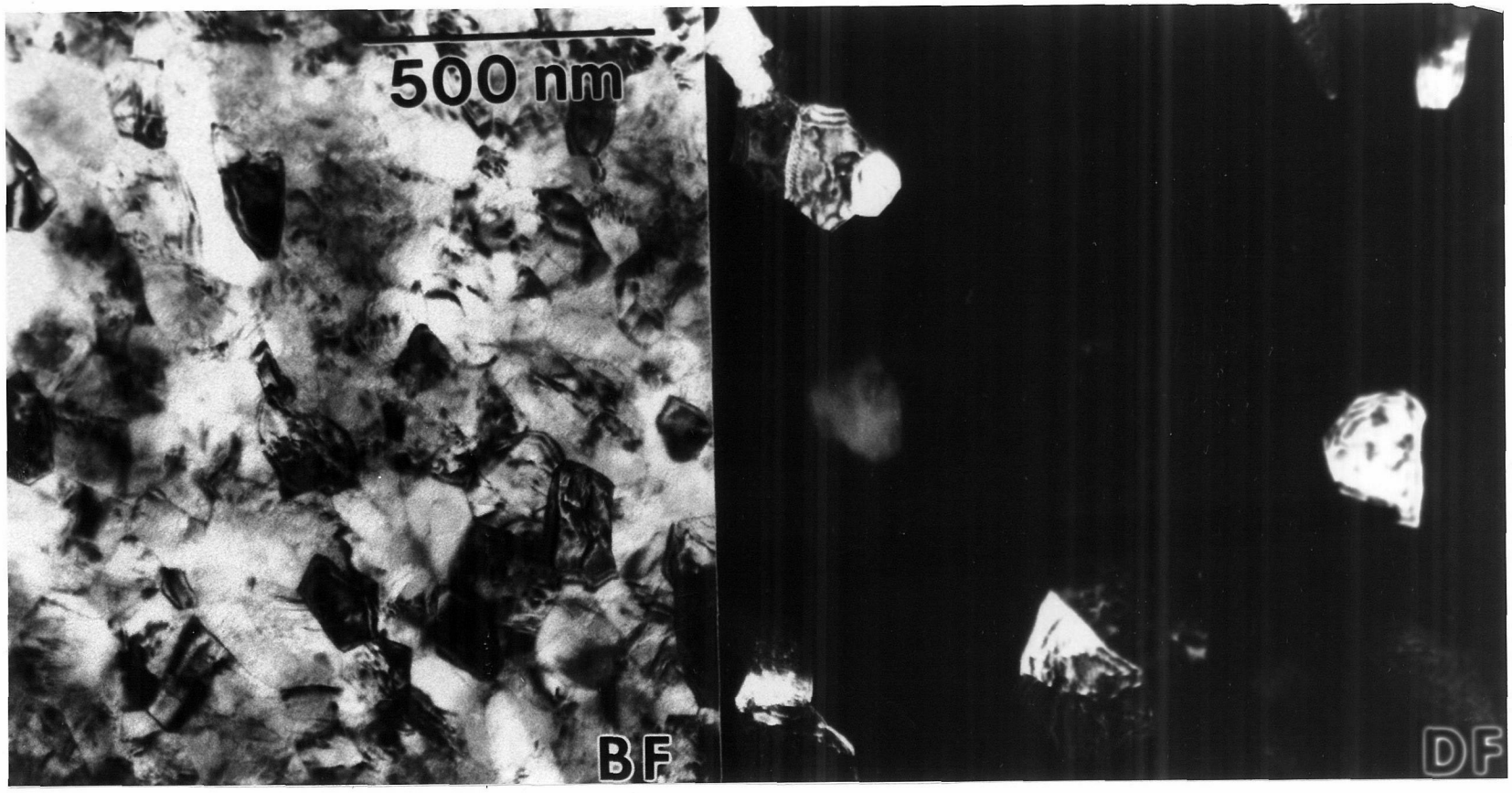

Figure 2.6 Bright field and dark field TEM images of as-consolidated microstructure. Image analysis gives an average grain size of ≈ 80 nm. No texture or porosity was observed. The defect density within the grains appears to be low.

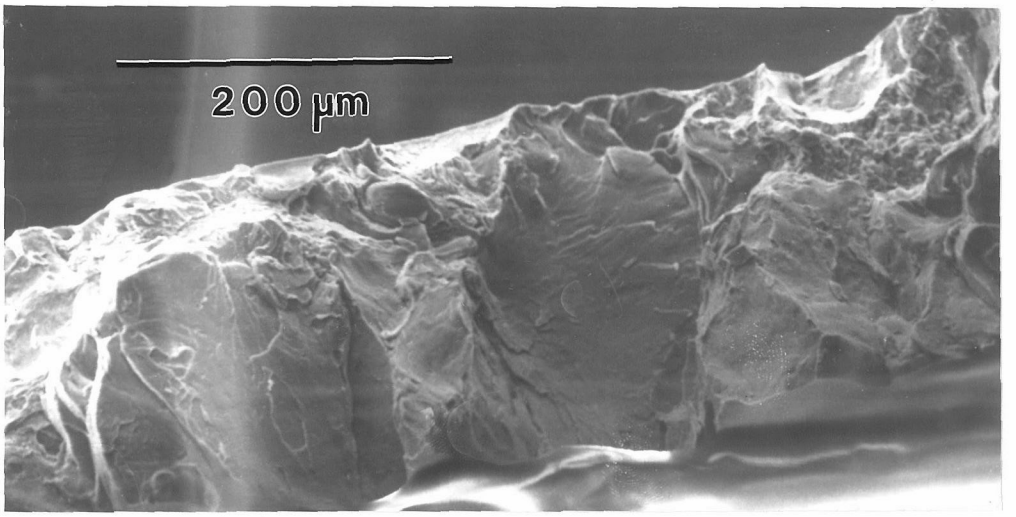

Figure 2.7 SEM image of the tensile fracture surface. The fracture surface is characteristic of interparticle fracture. The size scale of the powder particles corresponds well with the features on the fracture surface.

are very similar to those reported in the literature for Fe-Al-Cr intermetallics of this composition [25].

2.3.5 Post-Deformation Microstructural Characterization

The microstructure of the nanophase Fe-28Al-2Cr (in the plane perpendicular to the loading axis) deformed to a true compressive strain of 1.4 had two distinct constituents. Representative TEM images of these constituents are shown in Figures 2.9–2.12. The first region (Figure 2.9) consisted of grains with diameter $\approx$ 200 nm. (The 200 nm grain size microstructure will be refered to as Type B.) These grains are severely deformed and show a very high dislocation density. The dislocation density is fairly uniform and a cellular dislocation structure (typical of severely cold worked materials) is observed in some grains. The grains in the Type B microstructure are "pancaked" grains of Type A microstructure. This was confirmed by TEM micrographs taken transverse to the loading direction, Figure

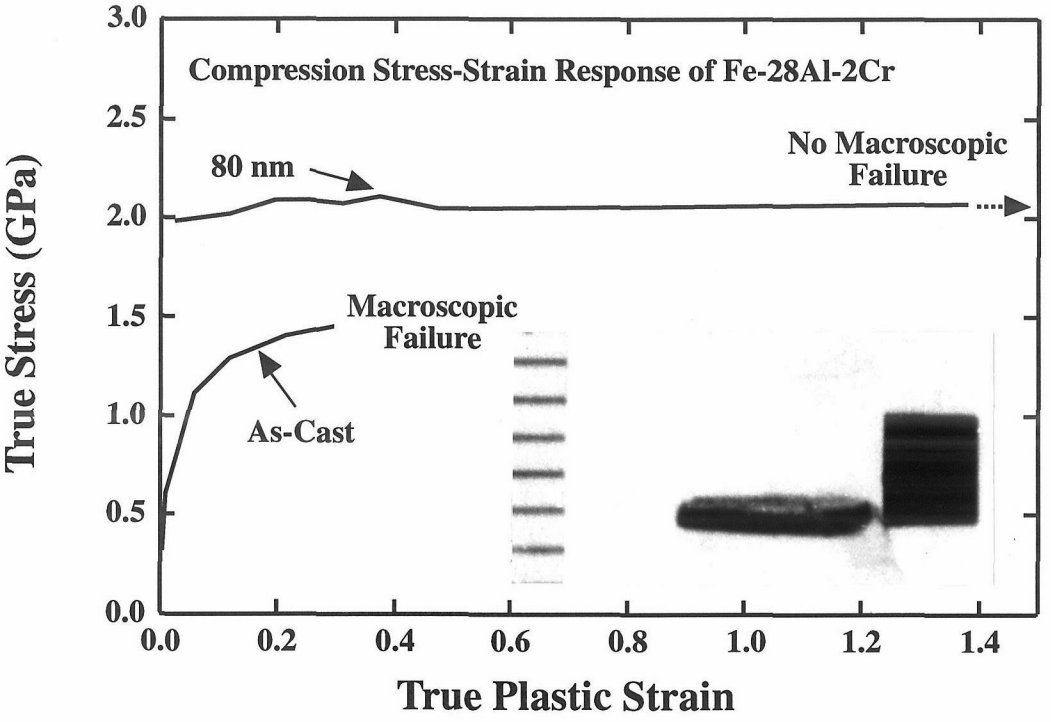

Figure 2.8 The true stress - true plastic strain compression response for the nanophase and as-cast Fe-28Al-2Cr. The as-cast response is similar to that reported in the literature for Fe-28Al-2Cr [25]. The nanophase material showed no evidence of strain hardening or failure despite plastic strains greater than 1.4. The inset shows a sample before and after compression testing.

2.10. The change in the grain morphology from Type A to Type B microstructures matches the macroscopic imposed deformation.

In the second region, a mixture of an amorphous and a crystalline phase is evident from the selected area diffraction pattern. The high magnification image (Figure 2.12) of this region reveals that the 10–15 nm grains are surrounded by an amorphous boundary. (The 10–15 nm grain size microstructure will be referred to as Type C.) It is also evident from the dark field image (Figure 2.11) of a bigger cross-section of a Type C region that there is no orientation relationship among neighboring grains. The Type C region showed no evidence of dislocations or

other structural defects; however, observations of dislocations at these grain sizes is difficult. The chemical composition of each of these regions as determined by EDAX analysis did not reveal any segregation between Type B and Type C regions.

It should be emphasized that no transitional microstructural states or intermediate grain sizes were observed. In addition, Type B and Type C microstructures were observed directly adjacent to each other. These observations suggest that the transition between Type B and Type C microstructures is discontinuous and distinct.

The volume fraction of Type B and Type C regions could not be calculated by examination of the TEM foils. Although both regions were observed in all foils, the volume fraction varied with the sample preparation procedure. The foils made by electropolishing had a majority of Type C regions, while samples made by low temperature ion milling contained a majority of the Type B microstructure. No other microstructural aspects (e.g., grain sizes within Type B or Type C microstructures) varied with sample preparation technique. Preferential thinning of materials with distinct microstructural variations is not unusual and does not make the observed microstructures suspect (with the singular exception of conclusions regarding the volume fractions). Attempts to examine the microstructure by etching and optical microscopy were unsuccessful.

2.4 Discussion

2.4.1 Synthesis and Processing

The fabrication of large pieces of fully dense Fe-28Al-2Cr nanophase alloy was

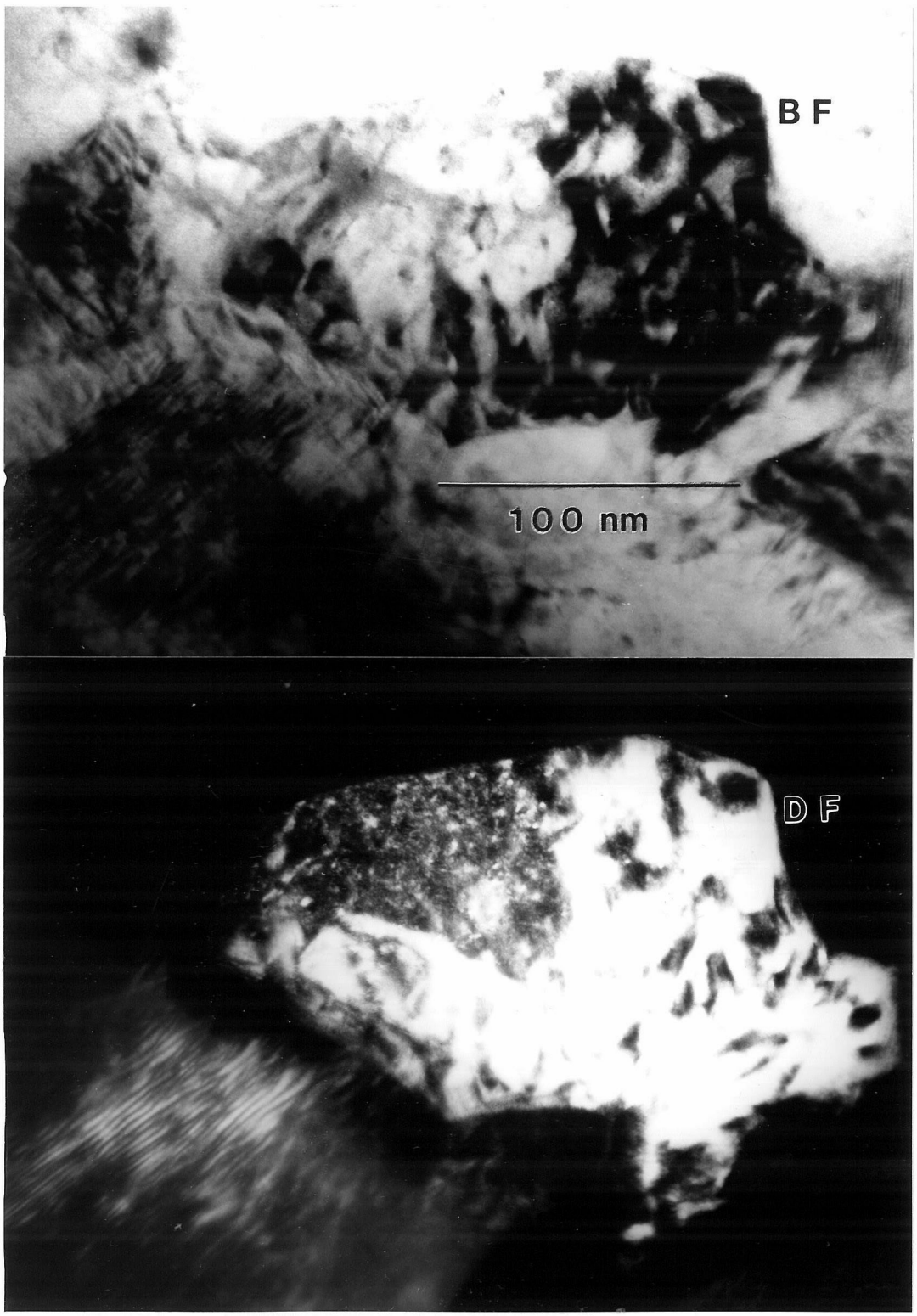

Figure 2.9 A bright field - dark field TEM image of the 200 nm diameter grains of the deformed microstructure. Note the increase in defect density compared to Figure 2.6.

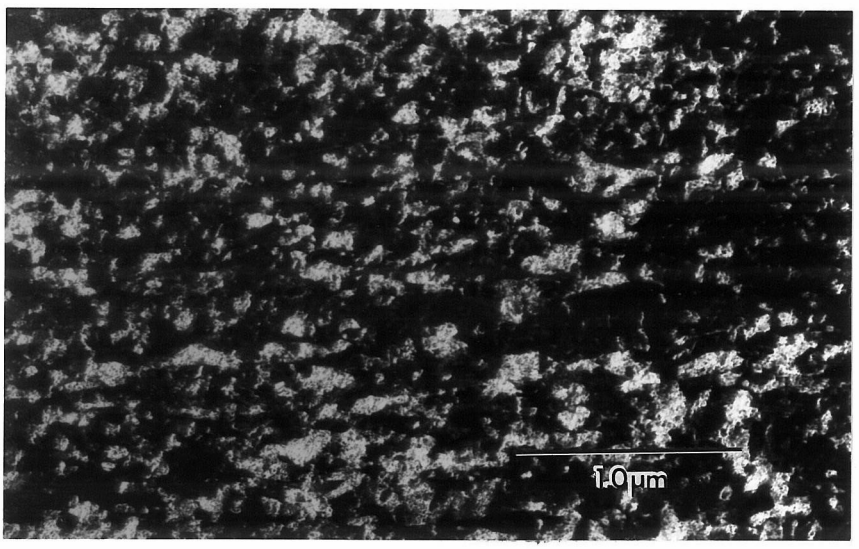

Figure 2.10 A dark field TEM image of the Type B microstructure in the plane parallel to the loading axis. Note the pancaked grains.

demonstrated by using high energy ball milling, to generate large amounts of nanophase powder, and shock compaction, to consolidate the nanophase powder effectively. All subsequent mechanical testing and microstructural examinations were dependent on successful consolidation. It should be noted, however, that commercialization of these processing procedures will be hampered primarily because of the complexity and expense involved with shock consolidation.

Shock consolidation of nanophase Fe-28Al-2Cr powder produced a fully dense compact, while retaining a nanophase microstructure. Thermodynamic and shock hugoniot data is not available for this alloy; but using data for steels, the predicted

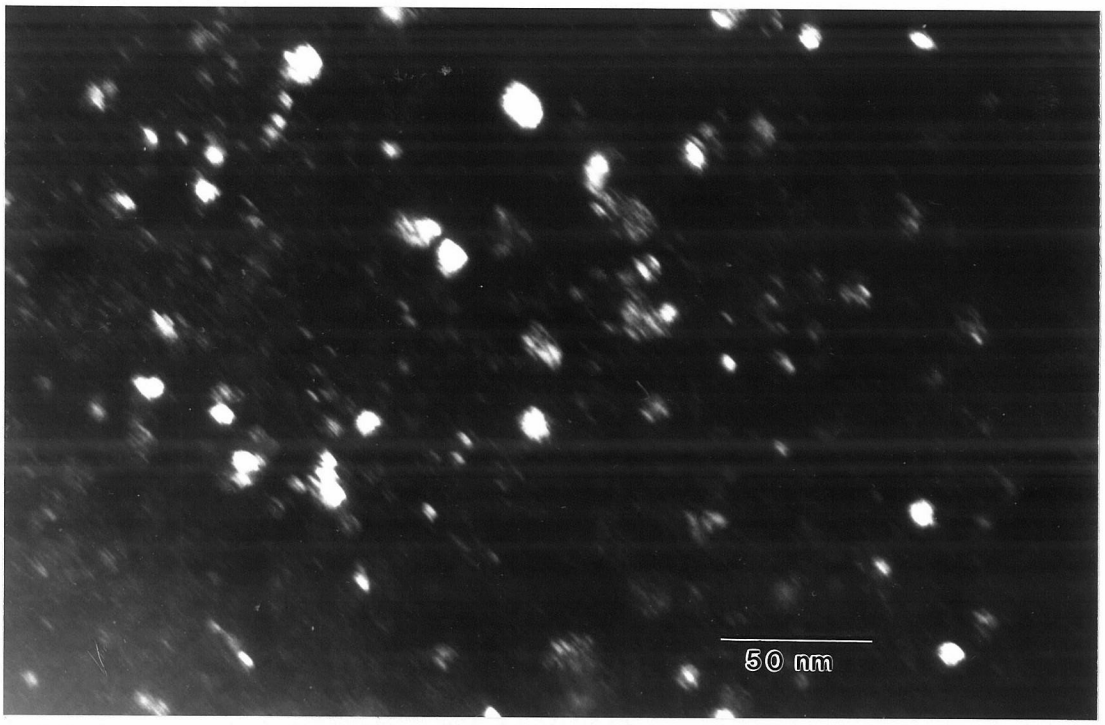

Figure 2.11 Low magnification dark field TEM image of the 10-15 nm grains. Note the large area occupied by these finer grains and the random orientation of the grains.

stress in the shock wave would be $\approx$ 10 GPa [19] with a melt volume fraction of 15%. Since this pressure is more than three times the room temperature yield strength, it is sufficient to fully densify the material. The microstructure produced by shock consolidation was fairly uniform with no clear indications of a rapidly solidified interparticle zone. This suggests two possibilities: (i) the percentage of rapidly solidified zone in the microstructure is much less than that estimated by the shock equations (using the thermodynamic and shock hugonoit data for steel), or (ii) the microstructure of the interparticle zones is controlled by the homogeneous temperature. Further investigation into both the shock consolidation process and the behavior of the nanophase material under these conditions is required to clarify this issue.

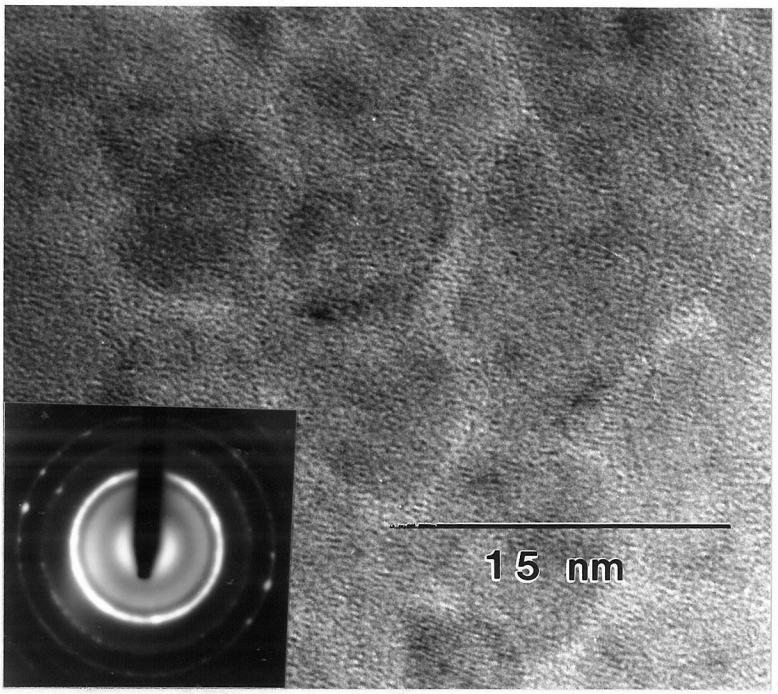

Figure 2.12 High resolution TEM images of the 10-15 nm grains. Note the large volume fraction of amorphous phase and the amorphous halo present in the diffraction pattern.

The homogeneous temperature during shock consolidation can be calculated from available theories, again using the shock parameters for steels, to be 550°C [19]. The compact should homogenize to this temperature within a few μs after the passage of the shock wave and cools quickly to ambient temperatures. Therefore, during consolidation, the powders are subjected to a time-temperature distribution containing very large spatial and time gradients. The extrapolation of traditional grain growth data to times on the order of ms is not very well understood and is worth further investigation; however, these calculations provide some insight into the shock consolidation conditions.

The low dislocation densities observed in the as-consolidated nanophase Fe-28Al-2Cr microstructure (Type A) are typical of well annealed materials. This is in

sharp contrast with the extremely high dislocation densities (similar to those in severely cold worked materials) observed for other shock compacted materials [23]. The very low defect density in the as-consolidated nanophase Fe-28Al-2Cr alloy appears to be a result of grain growth that occurs during consolidation. Analysis of dislocations and dislocation structures in ultrafine microstructures is a difficult experimental task because the orientation of a particular grain is unknown. The orientation of the grain is a necessary input parameter in the traditional analysis of standard TEM imaging methods for dislocations. To obtain a diffraction pattern from a single grain, the diffraction aperture must be smaller than the grain size which is difficult for these small grain sizes. Therefore, the contrast in the TEM images that we are attributing to dislocations is an interpretation and not definitive.

2.4.2 Deformation Mechanisms

The tension-compression anisotropy observed in nanophase Fe-28Al-2Cr appears to be a consequence of the competition between interparticle failure and plastic deformation. Interparticle failure in nanophase Fe-28Al-2Cr occurs at a similar stress to the failure of coarse grained Fe-28Al-2Cr ($\approx$0.65 GPa) where grain boundary failure has been shown to be the active mechanism. Plastic deformation is activated in nanophase Fe-28Al-2Cr at 2.1 GPa during room temperature compressive loading. In macroscopic compression loading, the local tensile stresses acting across powder - powder boundaries are reduced in magnitude from the macroscopic stress by a factor roughly proportional to the Poisson's ratio and, thus, brittle failure mechanisms are suppressed. This suppression results in an increase in compressive brittle failure stresses compared to tensile brittle failure stresses and has been well documented for many brittle materials, e.g., ceramics

and concrete [26]. In nanophase Fe-28Al-2Cr, the increase in the compressive brittle failure stress is of sufficient extent to allow the activation of plastic deformation. The absence of strain hardening during plastic deformation reduces the tendency for brittle failure and superplastic compressive flow occurs. In macroscopic tension, the local tensile stresses across powder - powder boundaries are roughly equal to the macroscopic stress and plasticity cannot be achieved.

The results suggest that deformation in 80 nm Fe-28Al-2Cr occurs in a two-stage process: first, the entire grain deforms by a dislocation generation mechanism (Type A to Type B transitions), and second, part of the microstructure collapses from the Type B microstructure into the Type C microstructure and deforms further by grain boundary sliding. The term "collapse" is used here because of the sudden and discontinuous nature of the grain size reduction. The microstructural evidence for dislocation deformation comes from changes in the observed dislocation density and the "pancaking" of the grains (compare Type A to Type B microstructures). The microstructural evidence for grain boundary sliding in Type C regions comes from the absence of dislocations and the presence of a "core-mantel" microstructural morphology. Details of these deformation mechanisms are discussed in Sections 4.3 and 4.4.

It is noteworthy that the present results on nanophase Fe-28Al-2Cr are consistent with the trends for a wide variety of other nanophase materials. We observed an increase in tensile strength and a decrease in tensile ductility as is reported for nanophase Cu and Pd [5]. In compression, we observed increased plastic flow that would not be expected in coarse grained material until significantly higher temperatures, as seen in nanophase TiO_2 and CaF_2 [12]. These trends have been attributed to different deformation mechanisms (Hall-Petch dislocation mecha-

nisms for the metals and diffusion activated creep mechanisms for the ceramics), e.g., [1-3]. In the present study, they are the result of competition between deformation and failure mechanisms. Whether or not similar events are occurring in these other materials cannot be determined from the available experimental evidence.

Contamination of the powders during ball milling does not appear to be affecting the comparison of the present results to those available in the literature for Fe-28Al-2Cr. This is evidenced by the similarity between the mechanical properties of the as-cast material examined here and the Fe-28Al-2Cr results in the literature [25].

2.4.3 Dislocation Deformation in Nanophase Fe_3Al

There are several dislocation models available that are capable of predicting increased strength with decreasing grain size. The relationships between grain size and yield strength for these models generally follow the experimentally well established coarse grained observation given by equation 1. Another common feature of most models is production and motion of dislocations in the microstrain region before macroscopic yielding. Dislocation generation before macroscopic yielding has been well documented for many metallic materials [27]. Experimental verification of one particular model depends on detailed knowledge of the dislocation distributions which is difficult to obtain for coarse grained materials and effectively impossible for nanophase materials. However, close inspection of the implications of these models can provide some insight into the most probable strengthening mechanism.

The traditional "Hall-Petch" mechanism [15-17] is based on dislocation pile-ups where the limiting event is the propagation of strain across the grain boundary.

Several mechanisms have been proposed for this propagating event; however, fundamental to all of these models is the concentration of stress at or near the grain boundaries. The concentration of the applied stresses at the grain boundaries raises questions about the applicability of these models for nanophase Fe-28Al-2Cr, because Fe-28Al-2Cr has a grain boundary failure stress (0.65 GPa) that is well below the macroscopic flow strength (2.1 GPa). Dislocation pile-up mechanisms are more likely (but not required) in materials where the grain boundary strength is greater than the flow strength; a condition that holds for most coarse-grained metallic materials.

Li [28] developed a model for grain boundary strengthening (schematically shown in Figure 2.13) based on dislocation generation from grain boundary ledges, Figures 2.13(a) and (b). A variety of other grain boundary sources are suggested by Hirth [34], and Price and Hirth [33]. The emitted dislocations produce a Taylor dislocation forest, Figure 2.13(c). The flow strength of the material is then determined by the stress required to move additional dislocations through the forest. The macroscopic yield strength is given by

$$\sigma = \sigma_o + \alpha\mu b\left(\frac{8m}{\pi d}\right)^{\frac{1}{2}}, \tag{1}$$

where, σ is the shear yield strength (taken to be half the axial flow strength), σ_o is the coarse grained shear flow strength, α is a constant, μ is the shear modulus, m is the ledge density, and d is the grain size. This equation gives the well known inverse square root grain size relationship; however, it does not require dislocation pile-ups, and the corresponding grain boundary stress concentrations, to be present. By comparison with experiments, Li discusses some appropriate

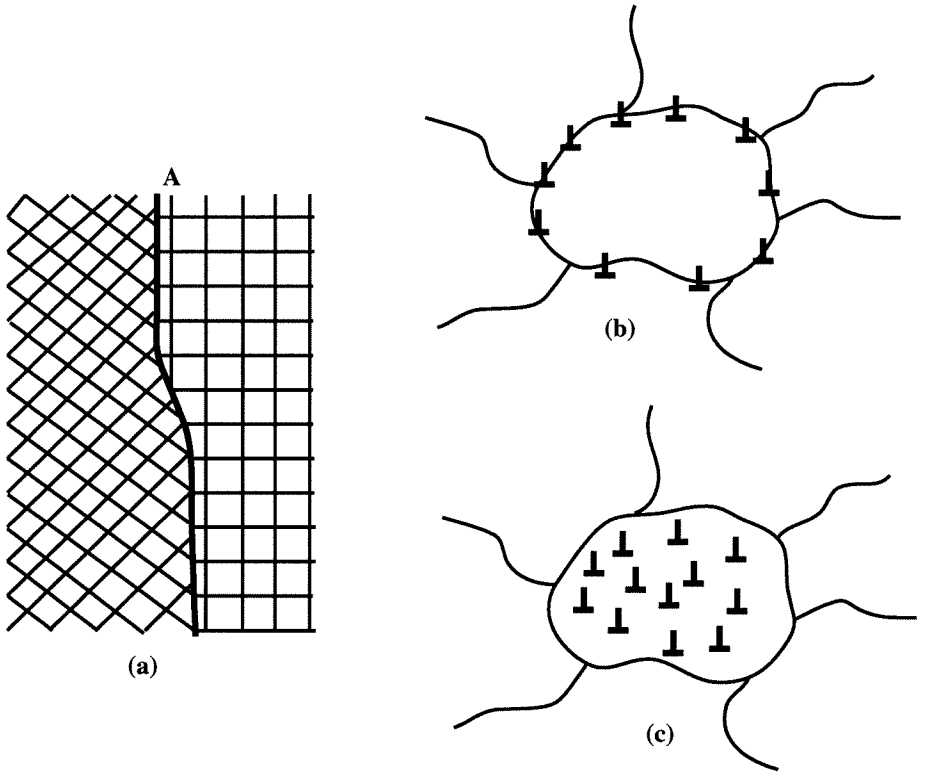

Figure 2.13 Schematic of the grain boundary dislocation generation and forest hardening mechanism described by Li [28]. Figure (a) shows a grain boundary ledge, or dislocation source. Figure (b) shows the distribution of sources before deformation and Figure (c) shows the dislocation forest after microstraining has occurred. For nanophase materials the forest would be expected to cover the entire grain.

values for the ledge density parameter, m. The values reported for Fe, Al, and Al-3% Mg are $mb = 0.02$ to 0.2, $mb = 0.1$, and $mb = 0.2$, respectively. The value for the constant α ranges from 0.2 to 0.4 depending on the dislocation distributions and the calculations of dislocation densities [35-38]. A rough check of the validity of the model can be made using the following parameters: $mb = 0.2$, $b = 0.25$ (an approximate nearest neighbor distance for Fe-28Al-2Cr), $d = 80$, $\sigma_o = 0.25$ (the coarse grained strength), and $\mu = 70$ (all length terms in nm and stress terms in GPa). For these parameters, equation 1 gives an axial flow strength of 1.3 to

2.5 GPa (depending on the choice of α) which is in agreement with the observed flow strength of 2.1 GPa.

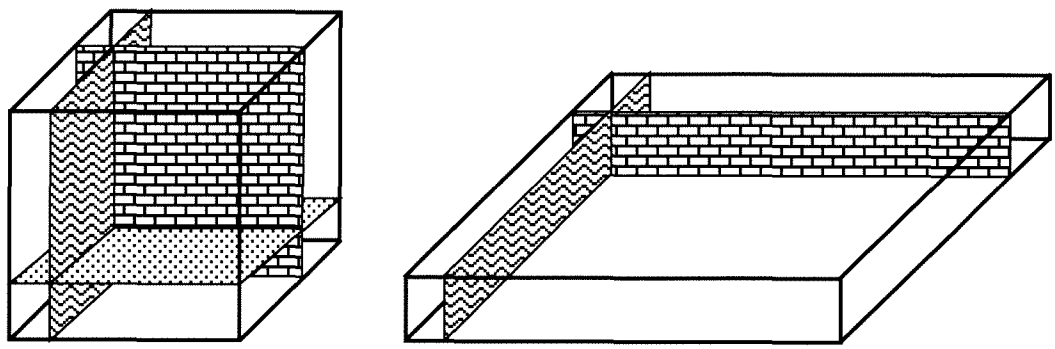

Figure 2.14 Distribution of dislocation cell boundaries for (a) 3-d and (b) 2-d dislocation array configurations used for dislocation spacing calculation in the cell boundaries. The dislocations on a given plane are assumed to lie parallel to one another in a configuration similar to the classical low angle tilt boundary. The sequence of cell boundaries section the grain into cubes. The 2-dimensional array corresponds to a severely "pancaked" microstructure.

The presence of the dislocation forest can also be used to explore the collapse process (from Type B microstructures to Type C microstructures) by comparing the energetics and atomic structure of dislocation arrays and grain boundaries. The dislocation density can be predicted using the following equation (also used by Li in the derivation of equation 1);

$$\sigma = \sigma_o + \alpha\mu b\rho^{(1/2)}. \tag{2}$$

A dislocation density of $\rho = 7 \times 10^{12}\text{cm}^{-2}$ is obtained with $\alpha = 0.2$. In the early stages of deformation the dislocations can be assumed to be distributed

homogeneously in three dimensions throughout the grain because the dislocation sources (i.e., grain boundaries) are well distributed throughout the material. After strains of 1.4, however, the grains have "pancaked" to a condition where the small dimension of the grain, d_s, approaches 10-15 nm. The correlation between d_s and the collapsed grain size suggests that only a 2-dimensional network of grain boundaries must be formed to collapse the "pancaked" grain, not the 3-dimensional network required in an equiaxed grain with the same dislocation density. This process is schematically shown in Figure 2.14. (It is noteworthy that equation (2) has been shown to be valid for strains up to 20% [35].)

If one assumes that ρ does not change during deformation, which is reasonable given equation 2 and no experimentally observed strain hardening, then the average dislocation separation in the dislocation boundaries can be approximated for the two- and three-dimensional planar dislocation arrays under the following assumptions:

- The grain is a rectangular parallelopiped for the two-dimensional case and a cube for the three-dimensional case as shown in Figure 2.14.
- The dislocations are distributed on a two or three-dimensional array of planes that create cubes of size d.
- The dislocations are uniformly spaced on all planes.
- The dislocation density is given by equation 2.

Under these assumptions, the average dislocation spacings are $\approx$ 2.5 nm or $10b$ for the 2-dimensional case and $\approx$ 3.75 nm or $15b$ for the 3-dimensional case. Dislocation core radii are generally considered to be up to $\approx 4b$ [36]. Thus at a separation of $8b$ the dislocation cores are overlapping. Therefore, the 2-

dimensional dislocation planar array approaches the condition of core overlap.

This results in an average misorientation of $\approx$ 4 degrees in 3-D case and the average misorientation of $\approx$ 6 degrees in the 2-D case. However, the average misorientation among the grains in Type C microstructure was clearly significantly higher. This indicates that the rearrangement of dislocations into the cell walls alone is not enough for the formation of fine grain structure. This suggests parallel or serial operation of some other mechanism that can cause increase in misorientation among dislocation cells (subgrains).

McQueen et al. [53,54] has observed significant grain boundary migration and conversion of some of low angle cell boundaries into medium to high angle boundaries during the high temperature deformation (torsion) of aluminum when separation between the grain boundaries approaches twice the dislocation cell size. This process is also known as "geometrical dynamic recrystallization". However, no direct evidence for operation of such process is available from present investigation. Moreover, McQueen et al. have observed conversion of only a fraction of low angle cell boundaries into medium or high angle boundaries, while the misorientation for the rest of the cell boundaries did not change significantly during deformation. Nevertheless, in the present investigation, we have observed pockets of Type C and Type B microstructures, and the misorientation among all the grains in Type C microstructure were large (significantly greater than 6°). This together with the core-mantle morphology of the Type C microstructure suggests that the conversion of subgrains into grains takes place by superplasticity mechanisms. The conversion of low angle boundaries into high angle grain boundaries has been observed to take place by during superplastic deformation by several authors in several different alloy systems. This mechanism is further discussed in

the next section.

It is not clear from the present results whether there are other microstructural features that might affect grain refinement process. Anti-phase boundaries or solute concentrations represent two such features. Evaluation of the x-ray superlattice peaks and the TEM observations were inconclusive regarding the presence and distribution of anti-phase boundaries. Definitive statements are not possible regarding these potentially complicating issues.

2.4.4 Grain Boundary Sliding in Nanophase Fe-28Al-2Cr

Deformation by grain boundary sliding requires a limited amount of grain shape changes to accommodate local geometrical constraints [49]. This point has been discussed in detail by Ashby and Verrall [50] and Gifkins[51,52] in the development of their respective grain boundary sliding models. This local deformation can be achieved by a wide variety of mechanisms, including, dislocation motion and atomic diffusion. It is important to emphasize that the changes in grain shape are due to *local compatibility constraints* and do not contribute substantially to the macroscopic strain. Therefore, these local deformations are not geometrically related to the macroscopic deformation; i.e., the changes in grain shape are not similar to the macroscopic deformation.

A "core-mantel" type deformation mechanism (schematically shown in Figure 2.15) would appear to be the most appropriate for the Type C microstructure. In this model, the "core" of the grain does not deform and the near-grain-boundary region, or "mantel", deforms to accommodate local geometrical constraints. The deformation of the "mantel" is due to local constraints and does not directly reflect the macroscopic deformation. The thickness (per grain) of "mantel" that is required for grain boundary sliding is $\approx 0.07d$, which is about that observed for

the thickness of the amorphous layer relative to the 10 nm grains [52]. Additional evidence that grain boundary sliding is active stems from the randomly oriented high angle grain boundaries that are observed. The calculations presented in Section 4.3 would suggest particular misorientations between grains (i.e., 6 degrees). The randomly oriented grains observed in the Type C microstructure suggests local grain rotation and sliding processes.

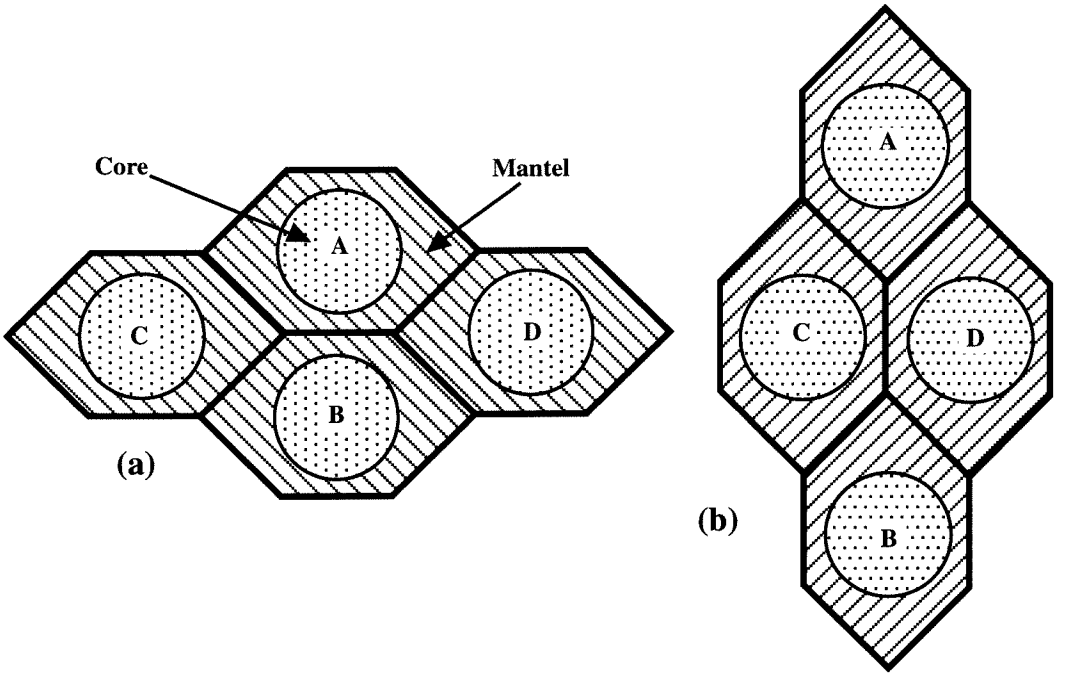

Figure 2.15 A schematic of "core-mantel" grain boundary sliding. The "core" does not deform and all compatibility constraints are met by deformation of the "mantel". Macroscopic strain is produced in the vertical direction by moving from state (a) to state (b).

A series of equations for the strain rates produced during "core-mantel" grain boundary sliding have been developed by Gifkins. The specific functional relationship between strain rate, applied stress, grain size, etc. intimately depends on

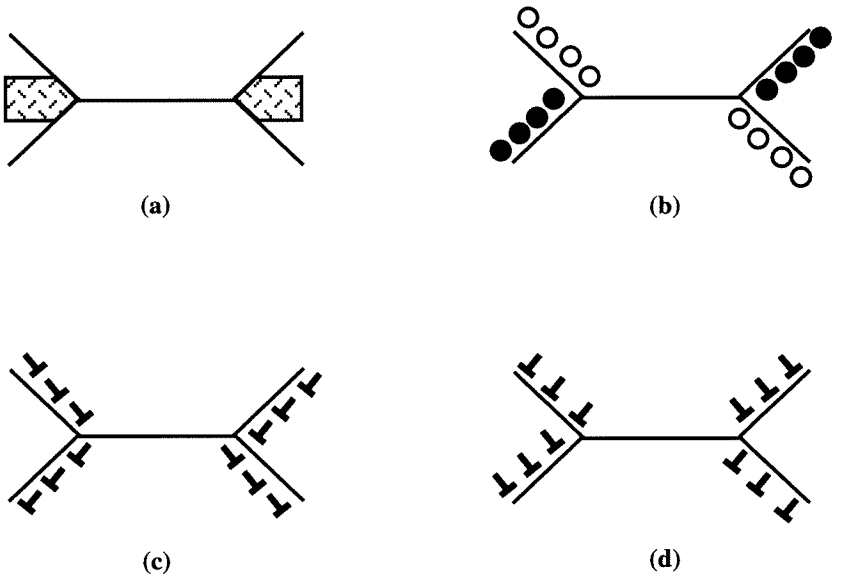

Figure 2.16 Schematic of local deformation mechanisms responsible for compatibility strains during grain boundary sliding as modelled by Gifkins. Figure (a) is triple point folding, Figure (b) is atomic diffusion, Figure (c) is dislocation climb, and Figure (d) is dislocation glide.

the details of the deformation mechanism within the "mantel". Gifkins [51,52] developed equations for four such mechanisms; (i) triple point folding (Figure 2.16(a)), (ii) atomic diffusion (Figure 2.16(b)), (iii) dislocation climb (Figure 2.16(c)), and (iv) dislocation glide (Figure 2.16(d)). However, all these models predict strain rates that are several order of magnitudes lower than used in the present investigation. The mechanism (grain boundary sliding) is qualitatively supported by the microstructural observations, but the quantitative modelling does not appear to be accurate. The activation of a "creep" deformation mechanism at room temperature and quasi-static loading rates (10^{-3} /sec) is unusual for an intermetallic material. Further work in this area is clearly required.

A subtle difference between the microstructure shown in Figure 2.15 and that experimentally observed is the absence of a sharp grain boundary in the Type

C microstructure. Throughout the deformation process described in references [51,52] a clearly defined grain boundary exists. In the Type C microstructure, however, the grain boundary is significantly thicker than those observed for coarse grained microstructures (i.e., the grain boundary represents a volumetric region not a planar region). It is not presently known how this microstructural difference will affect the local deformation mechanisms. Creep experiments should provide more insight into these local deformation mechanisms. With detailed knowledge of the nanophase Fe-28Al-2Cr deformation kinetics, more accurate models of nanophase grain boundary sliding can be formulated.

2.5 Conclusions

1. Large compacts (32 mm diameter and 6 mm thick) of 80 nm nanophase Fe-28Al-2Cr were successfully produced using high energy ball milling and shock consolidation.

2. Nanophase Fe-28Al-2Cr displayed brittle behavior in tension (σ_f = 0.65 GPa) and superplastic behavior in compression ($\sigma_y = 2.1GPa$). Compared to coarse grained material, the tensile failure strength is similar and the compressive flow strength is increased by approximately 1 order of magnitude.

3. The tension-compression anisotropy is caused by a competition between interparticle failure mechanisms and dislocation deformation mechanisms.

4. The compressive yield behavior can be quantitatively and qualitatively modelled well by the grain boundary strengthening theory proposed by Li [28]. This theory focusses on grain boundary production of dislocations and subsequent forest hardening.

5. A collapse of the microstructure is observed during deformation from an 80 nm grain size to a 10 – 15 nm grain size. This change in grain size is accompanied by a change from dislocation deformation mechanisms to grain boundary sliding.

6. The collapse of the microstructure can be modelled well by comparing the atomic structure and energetics of dislocation arrays to that of grain boundaries.

7. TEM results suggest that grain boundary sliding occurs by a "core-mantel" type mechanism. Existing models for this type of deformation do not appear to be quantitatively accurate and further work into nanophase grain boundary sliding is required.

References

[1] H. Gleiter, Prog. Mat. Sci. 33, 223 (1989).

[2] H. Gleiter, Nanostructured Materials 1, 1 (1992).

[3] R. Birringer, Mat. Sc. Engg. A117, 33 (1989).

[4] G. W. Nieman, J. R. Weertman, R. W. Siegel, Scripta Met. 23, 2013 (1989).

[5] G. W. Nieman, J. R. Weertman, R. W. Siegel, Scripta Met. 24, 145 (1990).

[6] G. D. Hughes, S. D. Smith, C. S. Pande, H. R. Johnson, R. W. Armstrong, Scripta Met. 20, 93 (1986).

[7] J. S. C. Jang, C. C. Koch, Scripta Met. 24, 1599 (1990).

[8] T. G. Nieh, J. Wadsworth, Scripta Met. 25, 955 (1991).

[9] A. H. Chokshi, A. Rosen, J. Karch, H. Gleiter, Scripta Met. 23, 1679 (1989).

[10] H. Chang, H. J. Hofler, C. J. Altstetter, R. S. Averbach, Scripta Met. 25, 1161 (1991).

[11] K. Lu, W. D. Wei, J. T. Wang, Scripta Met. 24, 2319 (1990).

[12] J. Karch, R. Birringer, H. Gleiter, Nature 330, 10 (1987).

[13] H. Hahn, R. S. Averbach, Nanostructured Materials, 1, 95 (1992).

[14] E. O. Hall, Proc. Phys. Soc. London B64, 747 (1951).

[15] N. J. Petch, J. Iron Steel Inst. 174, 25 (1953).

[16] A. H. Cottrell, The Mechanical Properties of Matter, John Wiley & Sons, New York, NY, 282 (1964).

[17] E. Hellstern, H. J. Fecht, Z. Fu and W. L. Johnson, J. Appl. Phys. 65, 305 (1989).

[18] H. J. Fecht, E. Hellstern, Z. Fu and W. L. Johnson, Met. Trans. 21A, 2333 (1990).

[19] W. H. Gourdin, Prog. in Mat. Sc. 30, 39, (1986).

[20] B. R. Krueger, A. H. Mutz and T. Vreeland Jr, J. Appl. Phys. 70, 5362 (1991).

[21] P. Kasiraj, Ph.D. Dissertation, California Institute of Technology, (1984).

[22] A. H. Mutz, Ph.D. Dissertation, California Institute of Technology, (1992).

[23] N. N. Thadani, A. H. Mutz, P. Kasiraj and T. Vreeland Jr., in "Metallurgical Applications of Shock-Wave and High-Strain-Rate Phenomena", edited by Murr, L. E., Staudhammer, K. P., and Meyers, M. A. (Marcel Dekker, New York, (1986).

[24] H. P. Krug and L. E. Alexander, in "X-ray Diffraction Procedures for Polycrystalline and Amourphous Materials", 2nd ed., John Wiley & Sons, New York, NY (1974).

[25] C. G. McKamey, J. H. DeVan, P. F. Tortorelli and V. K. Sikka, J. Mater. Res. 6, 1779 (1991).

[26] R. W. Hertzberg, "Deformation and Fracture Mechanics of Engineering Materials", 3rd ed., p. 23, John WIley & Sons, New York, NY (1989).

[27] T. Malis and K. Tangri, Acta Met. 27, 25 (1979).

[28] J. C. M. Li, Trans. TMS-AIME, 227 247 (1963).

[29] J. E. Bailey and P. B. Hirsch, Phil. Mag. 5, 485 (1960).

[30] A. S. Keh, in "Direct Observation of Imperfections in Crystals", edited by J. B. Newkirk, and J. H. Wernick, p. 213, Interscience, New York, NY (1962).

[31] D. V. Wilson and J. A. Chapman, Phil. Mag. 8, 1543 (1963).

[32] P. J. Worthington and E. Smith, Phil. Mag. 9, 211 (1964).

[33] C. W. Price and J. P. Hirth, Mater. Sc. Engg. 9, 15 (1972).

[34] J. P. Hirth, Met. Trans. 3, 3047 (1972).

[35] T. Narutani and J. Takamura, Acta Met. Mater. 39, 2037 (1991).

[35] D. Hull and D. J. Bacon, in "Introduction to Dislocations", 3rd ed., p. 77, Pergamon Press, (1984).

[37] W. T. Read and W. Shockley, Phys. Rev. 78, 275 (1950).

[38] J. H. Van Der Merwe, Proc. Phys. Soc. A63, 616 (1950).

[39] J. Eckert, J. C. Holzer, C. E. Krill III and W. L. Johnson, J. Mater. Res. 7, 1751 (1992).

[40] J. Eckert, J. C. Holzer, C. E. Krill III and W. L. Johnson, J. Mater. Res. 7, 1980 (1992).

[41] J. Eckert, J. C. Holzer and W. L. Johnson, Scripta Met. 27, 1105 (1992).

[42] L. E. Murr, in "Interfacial Phenomena in Metals and Alloys", TechBooks, Herndon, VA (1975).

[43] D. G. Morris and M. A. Morris, Acta Met. Mater. 39, 1763 (1991).

[44] Y. A. Abe and W. L. Johnson, unpublished results, California Institute of Technology, Pasadena, CA (1992).

[45] D. M. Cutrer and W. L. Johnson, unpublished results, California Institute of Technology, Pasadena, CA (1992). D. M. Cutrer,, Sc.B. Thesis, California Institute of Technology, Pasadena, CA (1992).

[46] R. W. Hertzberg, in "Deformation and Fracture Mechanics of Engineering Materials", 3rd ed., p. 114, John WIley & Sons, New York, NY (1989).

[47] W. L. Johnson, unpublished results, California Institute of Technology, Pasadena, CA (1992).

[48] R. Z. Valiev, N. A. Krasilnikov and N. K. Tsenev, Mater. Sci. Eng., A137 35 (1991).

[49] J. W. Edington, K. N. Melton and C. P. Cutler, C. P., Prog. Mat. Sci. 21, 61 (1976).

[50] M. F. Ashby and R. A. Verrall, Acta Met. 21, 149 (1973).

[51] R. C. Gifkins, Met. Trans. 7A, 1225 (1976).

[52] R. C. Gifkins, J. Mat. Sci. 13, 1926 (1978).

[53] J. K. Solberg, H. J. McQueen, N. Ryum and E. Nes, Phil. Mag. A, 60, 447 (1989).

[54] H. J. McQueen, J. K. Solberg, N. Ryum and E. Nes, Phil. Mag. A, 60, 473 (1989).

CHAPTER III

DEFORMATION INDUCED GRAIN REFINEMENT IN Fe-Al-Cr BASED INTERMETALLIC COMPOUNDS

3.1 INTRODUCTION

3.1.1 Fe-28Al-2Cr

The experimental observations from Chapter 2 indicate that grain refinement takes place in ≈80 nm grain size Fe-28Al-2Cr during compressive deformation. In addition, it has been demonstrated by several other authors that microstructures as fine as 100 nm can be produced in a wide range of metals and alloys by deforming them to true strains of 7 (99.9%). A significant amount of work has been performed in this area by a Soviet research group (Valiev et al. [1-4]) and a few others [5,6].

It is of interest to investigate the possibility, whether the above two processes can be combined to produce fully dense nanostructured Fe-28Al-2Cr intermetallic compound with an average grain size of about 10 nm. This processing route would not require any powder precursors and hence may provide an efficient way of producing nanostructured Fe-28Al-2Cr. In addition, the bulk nanophase intermetallic produced by this technique would not be expected to contain any residual porosity observed in powder metallurgical processed nanophase materials. However, there are several key issues that need to be resolved to determine the feasibility of this non powder metallurgical processing route for the synthesis of 10 nm Fe-28Al-2Cr in bulk form.

It is not known whether any signatures are required for the refinement of microstructure in 80 nm Fe-28Al-2Cr, because the grain size of the refined microstructure (≈ 10 nm)

following compresive deformation was very close to the grain size of the ball milled powder used for shock consolidation. Hence, it is quite possible that some kind of signatures (such as antiphase boundaries or in other forms) of the original microstructure ($\approx$ 16 nm) were left behind after the grain growth that occurred during the shock consolidation process. The role of these signatures (if any) in the deformation induced refinement process needs to be ascertained in order to determine the feasibility of producing nanostructured Fe-28Al-2Cr by a non-powder metallurgical technique. The 80 nm microstructure in Fe-28Al-2Cr for this investigation was obtained by recrystallization of heavily deformed ingot.

3.1.2 Fe-28Al-5Cr

It is generally very difficult to obtain microstructures with grain sizes of the order of $\approx$100 nm in bulk materials. Currently available techniques for generating $\approx$100 nm grain size microstructures in bulk samples either require powder consolidation by non conventional techniques or large amounts of plastic deformation (i.e. engineering strains of up to 99.9%). These considerations result in a serious limitation on the size of the products that can be produced by these techniques. The refinement of microstructure in Chapter 2 was attributed to formation of dislocation cells followed by grain boundary sliding (or cell sliding) among the cells that resulted in increased misorientation among the dislocation cells and their conversion into grains. However, it is not clear whether similar mechanisms can cause grain refinement in coarser microstructures (coarser than 80 nm). Because, if this is true, then this technique can be used to successively refine the microstructure starting from easily produced micron size microstructures in several steps to nanophase microstructures.

Fe-28Al-5Cr intermetallic compound with an average grain size of 175 nm produced by shock wave consolidation was used for this investigation. The 175 nm Fe-28Al-5Cr was

first deformed at various temperatures and various strain rates to obtain dislocation cell structure. The finest cell structure formed in 175 nm Fe-28Al-5Cr was coarser than 10 nm. The strain rate during deformation by grain boundary sliding is given by following equation:

$$\dot{\epsilon} = A\frac{DGb}{kT}(\frac{b}{d})^p(\frac{\sigma}{G})^n, \quad (1)$$

where $\dot{\epsilon}$ is the strain rate, A is a mechanism dependent constant, D is the appropriate temperature dependent diffusion constant, G is the shear modulus, T is the temperature, b is the burgers vector, d is the grain size, σ is the stress, p is a grain size exponent that ranges from 1 to 3 depending on the mechanism, and n is the stress exponent that also ranges from 1 to 3 depending on the model. It is clear from Equation 1 that for a given stress and strain rate, the temperature at which grain boundary sliding can take place increases with increase in grain size. Since the grain boundary sliding for 10 nm Fe-28Al-2Cr takes place at room temperature, the grain boundary sliding in the coarser microstructure would be expected to take place at higher temperature. The samples of Fe-28Al-5Cr with dislocation cell structure were deformed at higher temperatures and low strain rates with the intention of initiating grain boundary sliding among the dislocation cells.

3.2 Experiments and Results

3.2.1. Formation of ≈ 80 nm Microstructure in Fe-28Al-2Cr

It was found that recrystallization at 500°C can result in formation of ≈80 nm equiaxed grain microstructure in Fe-28Al-2Cr. Hence recystallization of heavily deformed Fe-28Al-2Cr intermetallic was used to obtain ≈80 nm microstructure in the present study as the samples produced in this manner would not be expected to contain any signatures of 10

nm microstructure. Valiev et al. [7] have also reported formation of submicron equiaxed grain microstructure in heavily cold deformed Ni_3Al by recrystallization treatment.

An approximately 10 gm ingot of Fe-28Al-2Cr was alloyed from constituent metals (obtained from CERAC, WI) of purity better than 99.9% by arc melting in a water cooled copper hearth. The ingot was kept in molten state for three minutes and then turned over and remelted again. This step was repeated twice to attain proper mixing of constituent elements. This ingot was then induction melted in a water cooled copper boat to give it irregular elongated rod-like shape for rolling.

It was found that lowering the temperature of deformation results in decrease of recrystallization temperature for Fe-28Al-2Cr and the rolling at room temperature resulted in lowering of recrystallization temperature to 500°C. But, Fe-28Al-2Cr is an intermetallic compound and only has limited room temperature ductility; as a result, it cannot be deformed extensively at room temperature. However, it was found that its ductile to brittle transition temperature decreases with increasing texture and results in increased ductility at lower temperatures. Hence the temperature of deformation was reduced as the ingot accumulated texture.

It was also found that the ductile to brittle transition temperature for Fe-28Al-2Cr in the as-cast state was between 450^0C and 500°C. The as-cast Fe-28Al-2Cr ingot prior to annealing treatment for recrystallization was deformed in the following manner: rolling from a cross section of 0.3" × 0.3" to 0.2" × 0.2" at 500°C, further rolling to 0.12" × 0.12" at 400°C, to 0.105" × 0.105" at 300°C, to 0.090" × 0.090" at 200°C and to 0.074" × 0.074" at 100°C. The total plastic strain to this point corresponds to ≈93%. The rolling of ingot at lower temperatures was found necessary to achieve lowering of recrystallization temperature. The Fe-28Al-2Cr wire at this point was room temperature ductile and could be rolled at room temperture. This wire will be referred to as RP2

in the rest of this chapter. The RP2 wire was then annealed at 500°C for 2 hrs for recrystallization.

3.2.2. Grain Refinement in 80 nm Fe-28Al-2Cr Produced by Ingot Metallurgical Route

Several almost cube shaped compression test samples were prepared out of annealed RP2 wire. These samples were deformed at room temperature and nominal strain rate of 9.5 $\times$ 10^{-3} sec^{-1} to an engineering strain of 70% and further rolled to a strain of 60% at room temperature. This corresponds to a total strain of 82%. The microstructure of the sample deformed in this manner was examined by transmission electron microscopy. Most of the microstructure was typical of heavily deformed metals, i.e., it contained a very high density of dislocations. However, a small fraction (approximately 2-3%) of the microstructure consisted of very fine grains (average grain size 6-7 nm) surrounded by amorphous phase. A micrograph of this microstructure is shown in Figure 3.1. The microstructure of the annealed RP2 wire deformed to 70% strain, as examined by TEM, consisted of very high dislocation density and no trace of fine grain structure.

Due to the small size of the RP2 wire the microstructure of the RP2 wire annealed at 500°C for 2 hrs could not be examined. However, to get an approximate idea of microstructure of the annealed RP2 wire. The RP2 wire was annealed at 500°C for 2 hrs and then deformed at the same temperature at the crosshead speed of 0.02"/min to an engineering strain of ≈66% and its microstructure was examined by TEM. Most of the microstructure was again typical of heavily deformed materials, nevertheless approximately 10-15% of the microstructure consisted of grains ranging from 100-150 nm. This suggests that about 10-15% of microstructure in the annealed (at 500°C fo 2 hrs) RP2 wire consists of ≈ 100 nm grains.

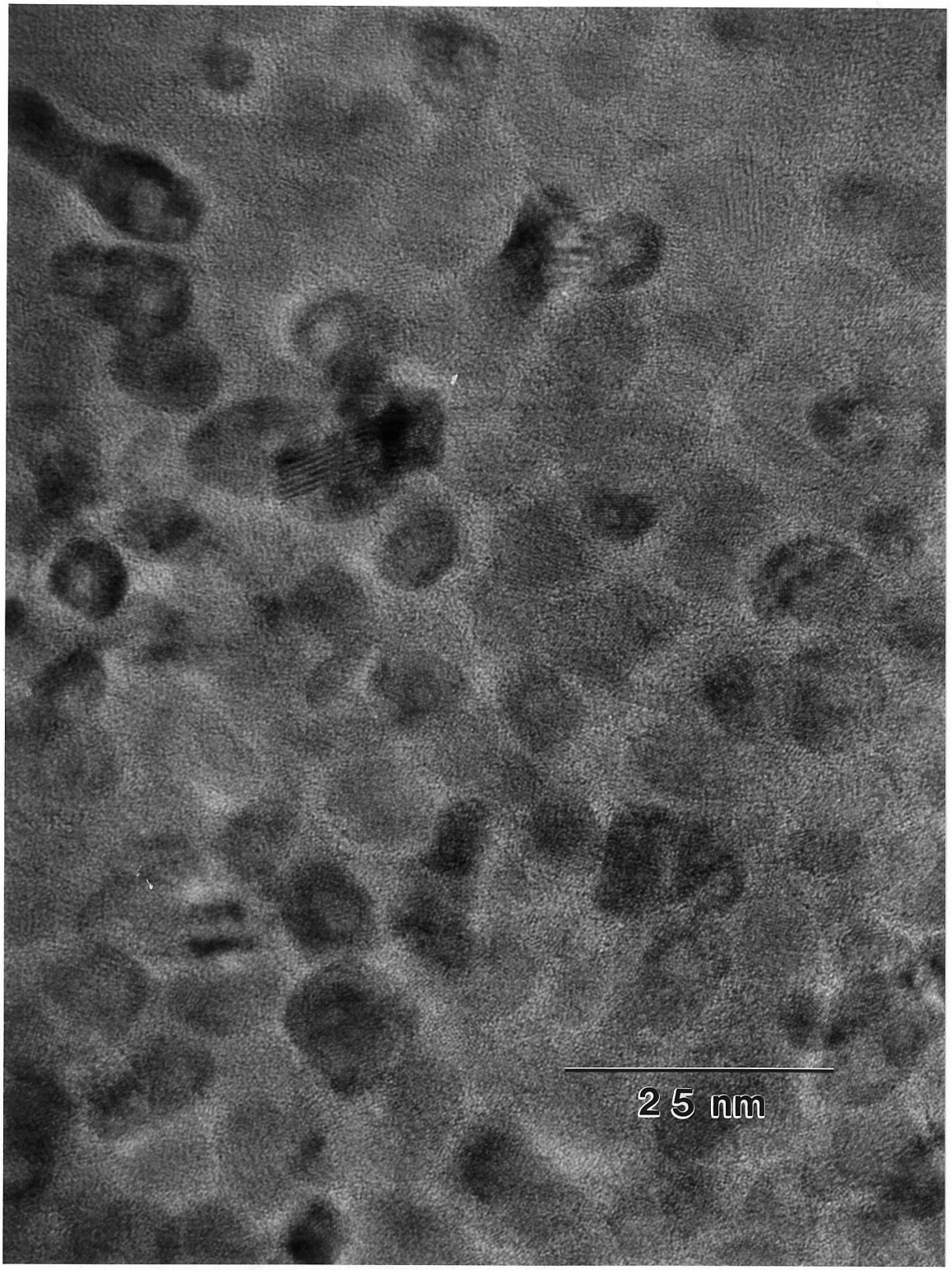

Figure 3.1 Microstructure in a small fraction of RP2 ingot that was annealed at 500°C for 2h and then deformed at room temperature. Note the thin layer of amorphous phase surrounding crystalline grains approximately 6-7 nm in size.

A piece of RP2 wire was also rolled at room temperature into a foil 0.010" in thickness. This foil was also annealed at 500°C for two hours. The microstructure of this foil was also examined by TEM. Approximately 60% of the microstructure was typical of the heavily deformed metals, while the rest consisted of the equiaxed grains with an average grain size of 100 nm.

3.2.3. Shock Wave Consolidation of Nanophase Fe-28Al-5Cr Powders

The coarse grain Fe-28Al-5Cr alloy powder for this investigation was obtained from Idaho National Engineering Laboratory, Idaho Falls, ID. Nanophase microstructures were produced by high energy ball milling in a SPEX 8000 shaker mill as described in Chapter 2. The ball milling for 8 hrs at room temperature resulted in a microstructure with a grain size of $\approx$ 13 nm. Nanophase Fe-28Al-5Cr powder produced by ball milling was shock consolidated as described in the previous chapter. The consolidation was performed with a flyer plate velocity of 1260 m/sec. A fully dense compact approximately 32 mm in diameter and about 10 mm in thickness was obtained after shock consolidation. Optical examination of this compact at 400$\times$ revealed no evidence of any porosity. Most of the microstructure of the compact after consolidation as examined by TEM was typical of well annealed material. It consisted of clean equiaxed grains with no evidence of disloctions inside them. This microstructure is shown in Figure 3.2. The average grain size in the compact was $\approx$175 nm. A small volume fraction (approximately 10%) of the microstructure had elongated grains approximately 150 nm wide and 500-1000 nm long. The presence of this microstructure was attributed to the molten region around the particle boundaries during shock consolidation processing.

3.2.4. Deformation Behavior of $\approx$175 nm Fe-28Al-5Cr

Several almost cube shaped samples approximately 2.5 mm in size, were made out of the

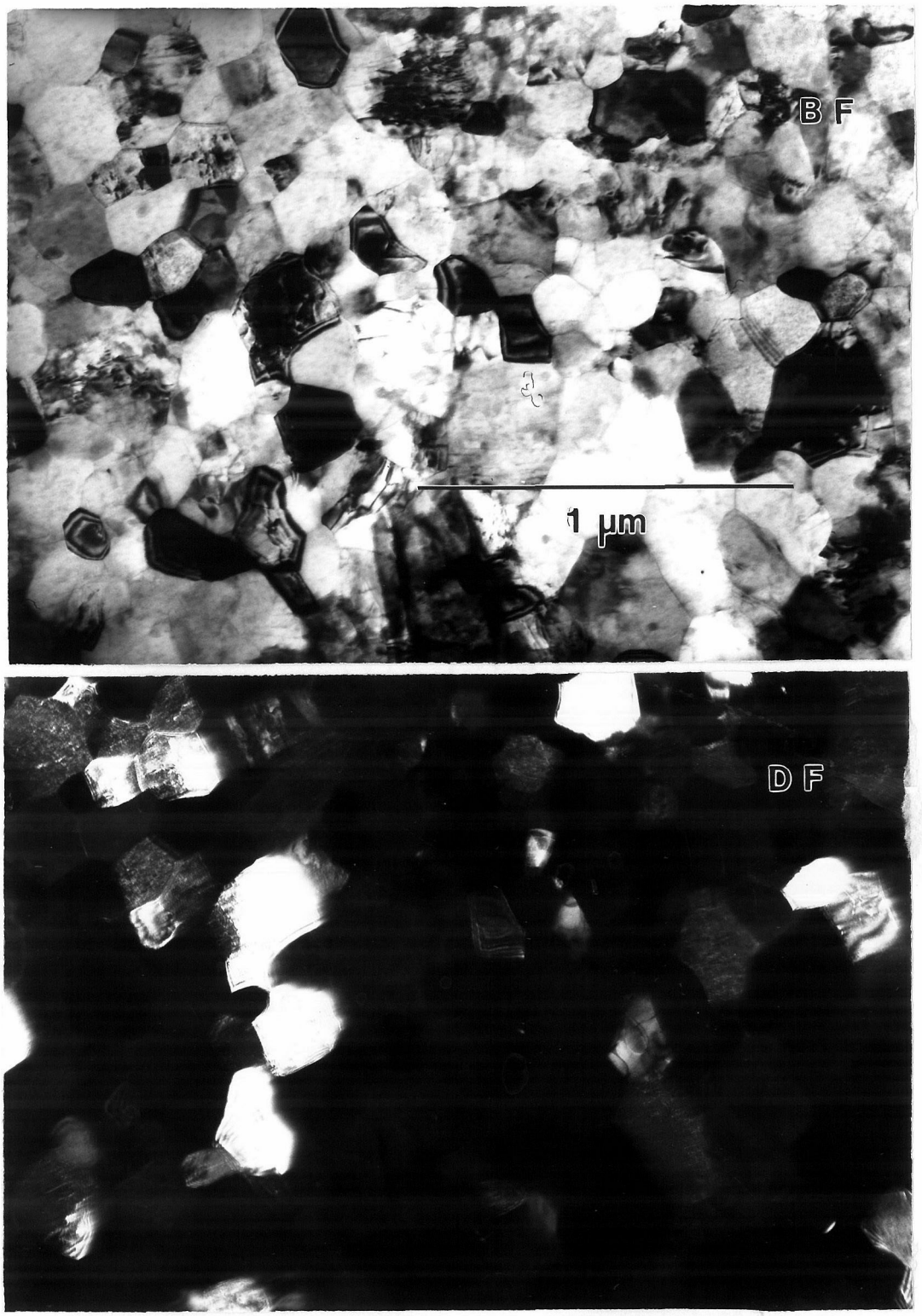

Figure 3.2 Microstructure of as consolidated Fe-28Al-5Cr (a) bright field image, (b) dark field image. The average grain size in the microstructure is about ≈175 nm.

consolidated compact. These samples were deformed at room temperature and 450°C and strain rate ranging from 4.3×10^{-3} to 1.2×10^{-2} sec^{-1} on an Instron 4204 load frame. The stress strain curve of the sample deformed at room temperature to an engineering strain of ≈33% and a nominal strain rate of 5.5×10^{-3} sec^{-1} is shown in Figure 3.3. The 175 nm Fe-28Al-5Cr intermetallic during room temperature deformation in compression yields at about 2.1 GPa and strain hardens very quickly to 2.5 GPa and deforms without strain hardening thereafter. The microstructures after deformation as examined by TEM are shown in Figure 3.4 and 3.5. The microstructure of the sample deformed at room temperature was typical of heavily deformed materials and consisted of very high dislocation density, while the microstructure of the sample deformed at 450°C was similar except that the dislocations formed a cellular network ranging in size from 40 to 100 nm.

The formation of 40-100 nm dislocation cells suggested that if the deformation is carried out at an appropriate strain rate and temperature then these cells may slide and form high angle grain boundaries. In addition, Equation 1 suggests that temperature of deformation for grain boundary sliding would have to be higher than room temperature as grain boundary sliding in ≈10 nm Fe-28Al-2Cr was observed at room temperature (assuming the material constant do not change significantly from Fe-28Al-2Cr to Fe-28Al-5Cr).

Hence a sample of 175 nm Fe-28Al-5Cr was deformed at 450°C and nominal strain rate of 4.0×10^{-3} sec^{-1} to an engineering strain of 68% and was further deformed 60% at the same temperature and nominal strain rate of 2.2×10^{-2} sec^{-1}. The lower strain rate deformation was carried out with the intention of initiating grain boundary sliding. The microstructure after deformation was surprisingly different from those observed after the previous treatment. The microstructure after deformation in this sample consisted

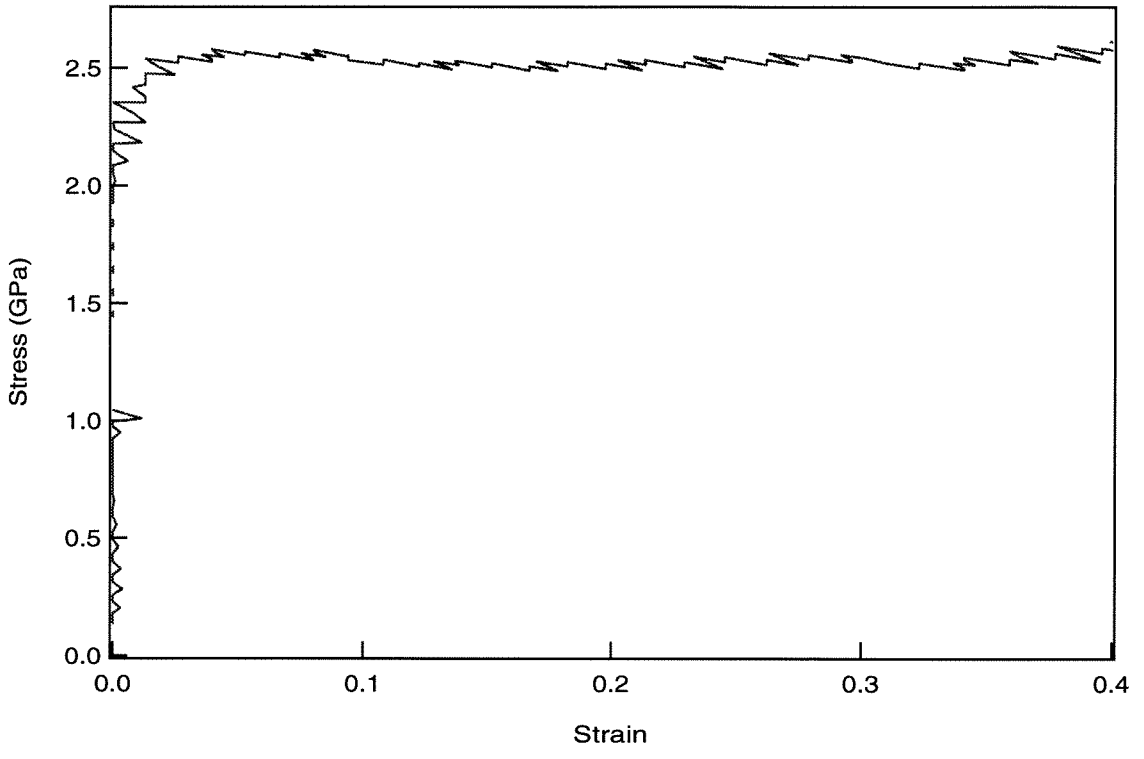

Figure 3.3 Stress-strain curve of ≈175 nm Fe-28Al-5Cr for deformation at room temperature and nominal strain rate of 5.5×10^{-3} sec^{-1}. Note the elastic perfectly plastic behavior of the stress-strain curve.

primarily of two regions: (i) about one half * of the microstructure consisted of heavily deformed structure similar to that in Figure 3.5, while (ii) the other half contained mostly dislocation free grains (Figure 3.6) ranging from 30-80 nm in size.

Another sample was deformed to an engineering strain of ≈75% at 450°C and nominal strain rate of 9.9×10^{-4} sec^{-1}. The microstructure after the deformation consisted of a mixture of 30-80 nm equiaxed grains and regions of very high disloction density. However, the fraction of the fine grained microstructure was significantly less than obtained

* The estimates on volume fraction of microstructure reported here are based on TEM examination of foils, hence should be treated with caution. These estimates are intended to construct a qualitative picture of the development of microstructure.

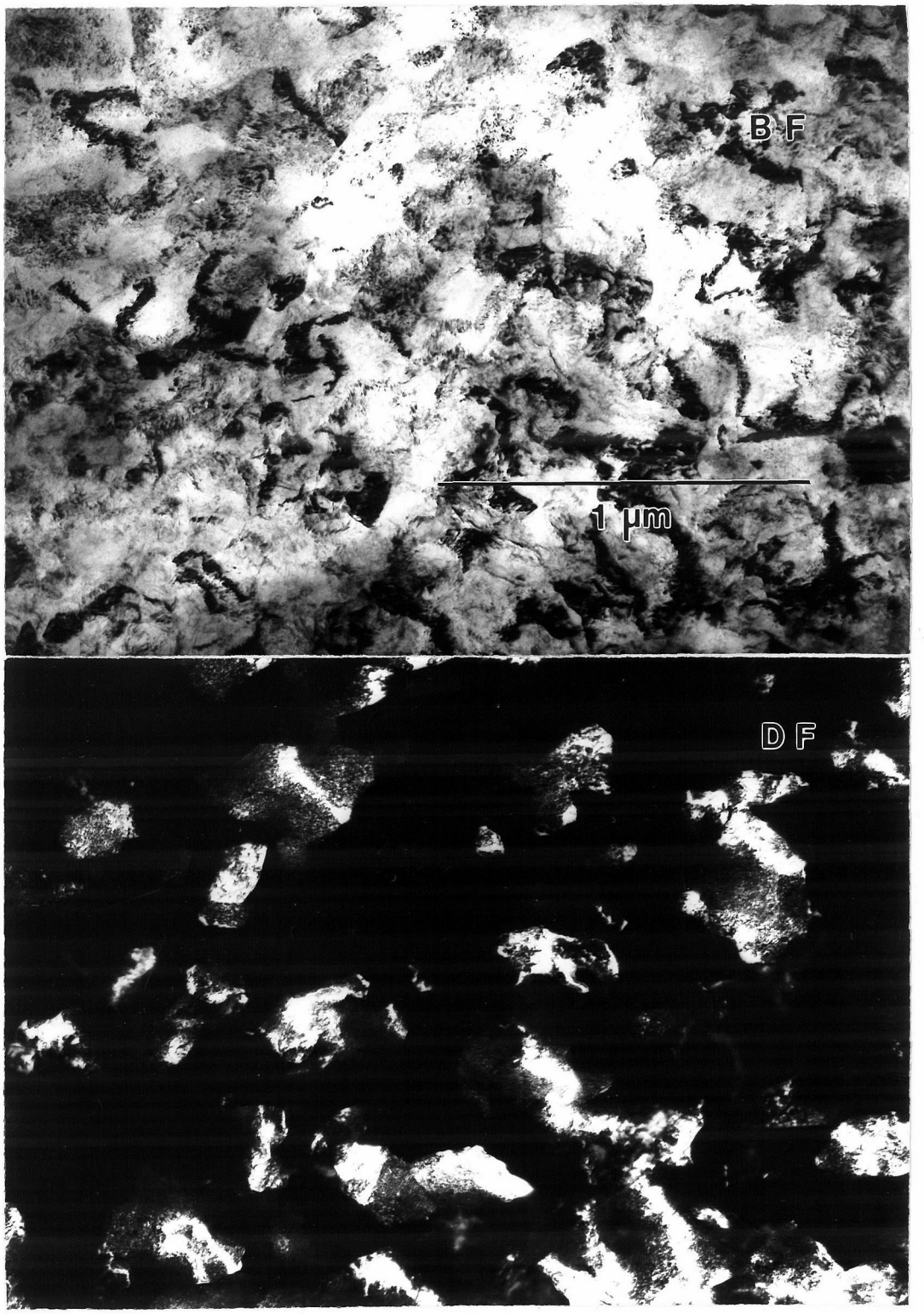

Figure 3.4 Microstructure of ≈175 nm Fe-28Al-5Cr deformed 84% at room temperature and nominal strain rate of 1.45×10^{-2} sec^{-1}: (a) bright field image, (b) dark field image. Note the high dislocation density in the microstructure.

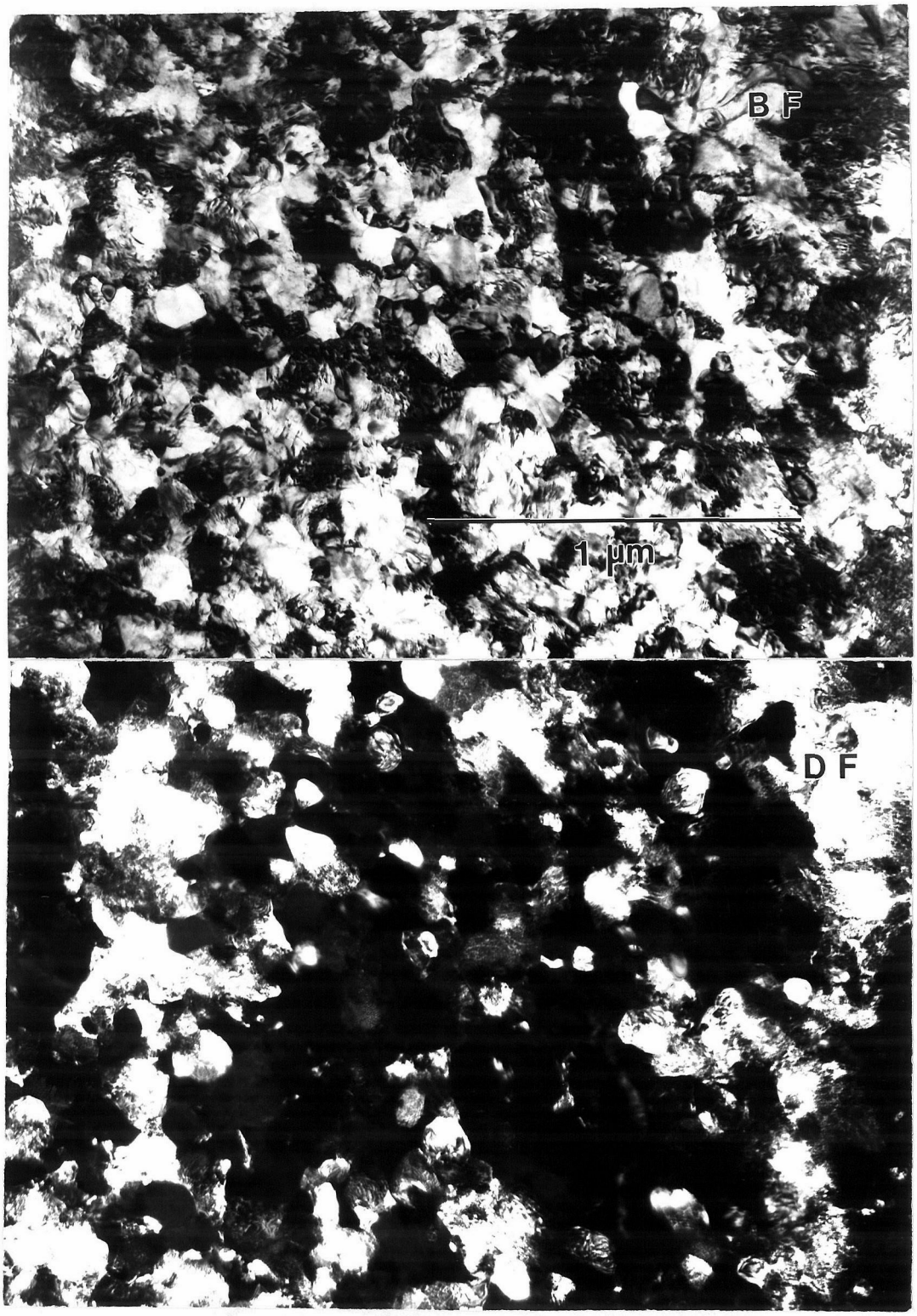

Figure 3.5 Microstructure of ≈175 nm Fe-28Al-5Cr deformed 68% at 450°C and nominal strain rate of 4.0×10^{-3} sec^{-1}: (a) bright field image, (b) dark field image. Note the high dislocation density and the fine dislocation cell structure.

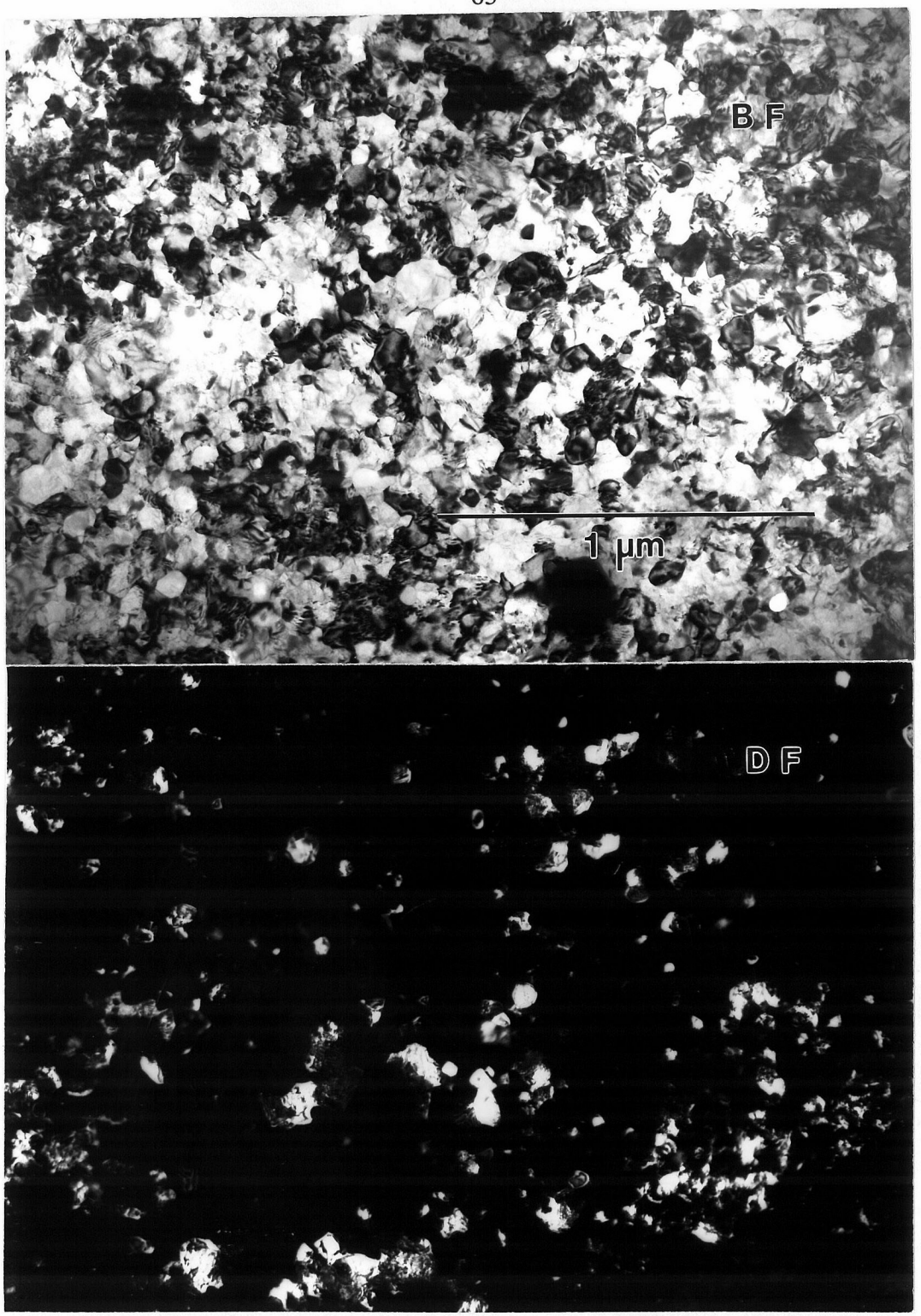

Figure 3.6 Microstructure of ≈175 nm Fe-28Al-5Cr deformed 68% at 450°C and nominal strain rate of 4.0×10^{-3} sec^{-1} and further deformed 60% at nominal strain rate of 2.2×10^{-3} sec^{-1}: (a) bright field image, (b) dark field image. The microstructure is a mixture of relatively defect free grains, approximately 30-80 nm in size and bigger grains with much higher dislocation density.

from the previous treatment.

To check if recrystallization is the cause of grain refinement, another 175 nm grain size Fe-28Al-5Cr sample was deformed to 75% strain at room temperature and nominal strain rate of 9.6×10^{-3} sec^{-1} and then annealed at 450°C for 2 hours. Most of the microstructure of this sample also consisted of very high dislocation density. Nevertheless, about 25% of the microstructure consisted of a fine structure with very sharp boundaries. This microstructure is shown in Figure 3.7. It is not clear at present whether these are high angle or low angle boundaries.

3.3 Discussion

3.3.1 Grain Refinement in 100 nm Fe-28Al-2Cr

Since ≈100 nm microstructure in a fraction of Fe-28Al-2Cr was obtained by recrystallization treatments on an ingot that was produced by alloying constituent elements in the molten state, it can be concluded that the ingot did not contain any signatures of 7 nm microstructure. The formation of 7 nm microstructure in a small fraction of this ingot after compressive deformation suggests that signatures of the 7 nm microstructures are not necessary for grain refinement in 100 nm grain size Fe-28Al-2Cr by compressive deformation. This also demonstrates that 7 nm grain size microstructures can be produced in bulk Fe-28Al-2Cr by a technique that does not require powder precursors.

The volume fraction of the 7 nm microstructure is quite small for any practical application. The low volume fraction of nanophase microstructure in the present investigation was due to the inability to produce 100 nm microstructure by wrought processing in a large enough sample to carry out further refinement processing.

However, our investigation on the recrystallization behavior of Fe-28Al-2Cr has indicated

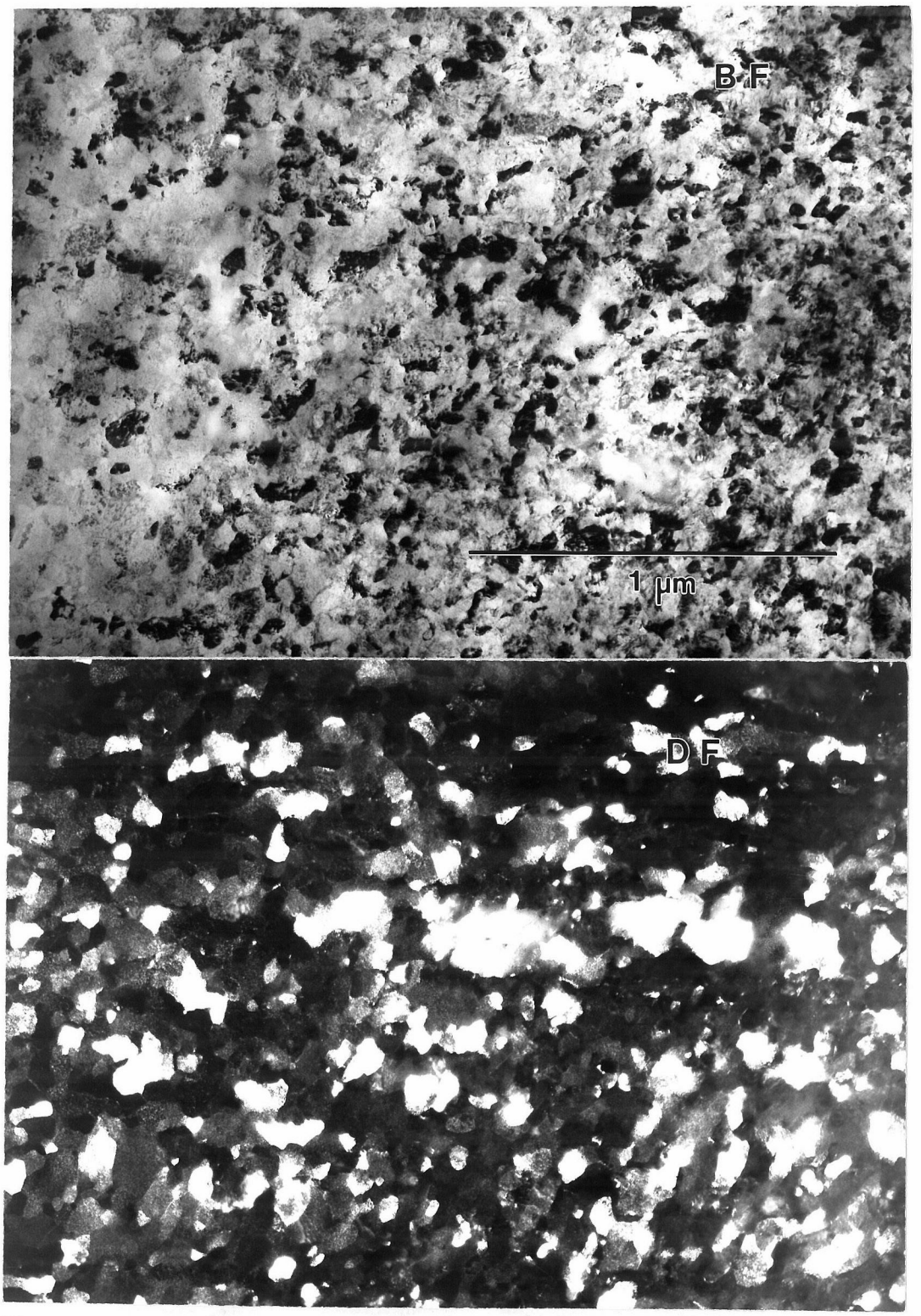

Figure 3.7 Microstructure of ≈175 nm Fe-28Al-5Cr deformed 75% at room temperature and nominal strain rate of 9.6×10^{-3} sec^{-1} and then annealed at 450°C for 2 hrs: (a) bright field image, (b) dark field image. Note the cell structure with sharp boundaries and high dislocation inside the cells.

that this problem can be overcome quite easily. It is clear that the volume fraction of recrystallized microstructure can be increased to 40-50% by rolling Fe-28Al-2Cr at room temperature prior to recrystallization treatment. This suggests that further increase in the volume fraction of recrystallized microstructure can be achieved by rolling the ingot at temperatures below room temperature. More research into the recrystallization behavior of Fe-28Al-2Cr is required to determine whether the volume fraction of the recrystallized microstructure (with grain size $\approx$100 nm) in Fe-28Al-5Cr can be increased closer to 100%.

Since grain refinement is observed in only a fraction of 100 nm grain size microstructure of Fe-28Al-2Cr, it appears that there is a critical grain size below which grain refinement to 7 nm takes place in Fe-28Al-2Cr during compressive deformation at room temperature. This is also consistent with the observations of Chapter 2. However, a deeper understanding of grain refinement process is needed to increase the efficiency of this processing technique.

3.3.2. Deformation Mechanisms in 175 nm Fe-28Al-5Cr

The 175 nm Fe-28Al-5Cr yields at 2.1 GPa and strain hardens very quickly to about 2.55 GPa. The stress strain curve for the 175 nm grain size Fe-28Al-5Cr is very similar to that observed for several other submicron grain materials (Cu and Al alloy) with comparable grain sizes [1,4]. The ultimate strength of 175 nm Fe-28Al-5Cr is slightly higher than that of 80 nm Fe-28Al-2Cr (2.1 GPa). It is not clear whether the increased strength of 175 nm Fe-28Al-5Cr over 80 nm Fe-28Al-2Cr is due to different chemical composition or bigger grain size. It should be noted that yield strength of Fe-28Al-5Cr is very close to that of Fe-28Al-2Cr in micron size microstructures.

In contrast to 100 nm Fe-28Al-2Cr, no grain refinement was observed in 175 nm Fe-28Al-5Cr intermetallic compound during room temperature compressive deformation. This

suggests either the lack of formation of dislocation cell structure in 175 nm Fe-28Al-5Cr or the formed dislocation cell structure is too coarse for any grain boundary sliding during room temperature deformation. The microstructure (Figure 3.4) after room temperature deformation appeared to consist of a homogeneous distribution of dislocations. The cell structure as fine as 10 nm are generally very difficult to resolve by TEM as the thickness of the TEM samples is several times the size cell structure. The microstructure after the room temperature deformation was typical of a heavily cold deformed metal as it contained very high dislocation density. However, formation of cell structure (40-80nm in size) in some parts of the sample was observed after deformation at 450°C (Figure 3.5).

In addition, grain refinement is observed in a part of the microstructure during low strain rate compressive deformation of 175 nm Fe-28Al-5Cr at 450°C. This suggests two possibilities: (1) since the dislocation structure formed in 175 nm Fe-28Al-5Cr is coarser (Figure 3.5) than that formed in 80 nm Fe-28Al-2Cr during room temperature deformation, deformation at higher temperatures and low strain rates is required to initiate grain boundary sliding in the microstructure which results in conversion of dislocation cells into grains, or (2) dynamic recrystallization is the cause of grain refinement as during deformation, because the sample spends a considerable amount of time at high temperature (450°C).

It would be expected that the deformation at room temperature would result in at least the same density of defects (if not more) than the sample deformed at 450°C and therefore the driving force for recrystallization would be the same (if not more) in the sample deformed at room temperature. A fraction of the microstructure in the sample that was deformed 75% at room temperature followed by annealing at 450°C for 2 hours contained a fine structure ranging from 30-150 nm in size with sharp boundaries. It was not clear

whether these boundaries were low angle or high angle grain boundaries. In general, the grains that form as a result of static recrystallization contain a relatively low density of dislocations. However, except for a few, most of these grains/cells contain a high density of dislocations. Hence, it appears that recrystallization is not the primary cause of grain refinement in 175 nm Fe-28Al-2Cr. More research effort in this area is needed to completely resolve this issue.

It therefore appears that the sharp boundaries formed upon annealing at 450°C are low angle cell boundaries. The formation of finer grain microstructure is consistent with the hypothesis that grain boundary sliding is causing increased misorientation among the dislocation cells as grain boundary sliding is preferred mechanism of deformation at higher temperatures and lower strain rates, however, several issues remain unresolved. It is not quite clear whether the formation of sharp cell boundaries is a prerequisite for grain boundary sliding. It is also not clear, whether the deformation at 450°C is required for the formation of sharp cell boundaries or for activation of grain boundary sliding deformation mechanism or both. Further work is also needed to resolve these isuues.

3.4 Conclusions

1. The signatures of final microstructure (7 nm, i.e., the grain size of powder precursor) are not needed for grain refinement from a 80 nm equiaxed grain Fe-28Al-2Cr intermetallic during compressive deformation.

2. The flow strength of 175 nm Fe-28Al-5Cr intermetallic (2.5 GPa) is higher than that of 80 nm Fe-28Al-2Cr intermetallic (2.1 GPa), while the yield strength of both intermetallics quite comparable (2.1 GPa). It is not clear, wether the higher flow strength is due to bigger grain size or slightly different chemical composition.

3. The grain refinement is observed in a significant fraction (40%) 175 nm Fe-28Al-

5Cr during low strain rate deformation at 450°C. The mechanisms responsible for this behavior are not completely clear. However, preliminary investigations indicate that grain boundary sliding among the dislocation cells that form after initial deformation play an important role in the grain refinement process.

References

[1] R. Z. Valiev, N. A. Krasilnikov and N. K. Tsenev, Mater. Sci. engng. A137, 35 (1991).

[2] N. A. Smirnova, V. I. Levit, V. I. Pilyugin, R. I. Kuznetsov, L. S. Davydova and V. A. Sazonova, Fizika Metall. 61, 1170 (1986).

[3] R. Z. Abdulov, R. Z. Valiev and N. A. Krasilnikov, J. Mater. Sci. Lett. 9, 1445 (1990).

[4] R. Z. Valiev, E. V. Kozlov, Y. F. Ivanov, J. Lian, A. A. Nazarov and B. Baudelet, Acta Met., 42, 2467 (1994).

[5] S. Erbel, Met. Technol. 6, 482 (1979).

[6] I. Saunders and J. Nutting, Metal Sc. 18, 571 (1984).

[7] J. Langiullaume, F. Chmelik, G. Kapelski, F. Bordeaux, A. A. Nazarov, G. Canova, C. Esling, R. Z. Valiev and B. Baudelet, Acta Met., 41, 2953 (1993).

CHAPTER IV

PROCESSING OF ULTRAFINE GRAIN 304 STAINLESS STEEL

4.1 INTRODUCTION

As mentioned in Chapter 1, ultrafine grain microstructures are of great technological importance for their significantly improved mechanical properties over coarse grain materials. However, like nanophase materials, these microstructures are highly metastable and therefore very difficult to produce in bulk form. These microstructures are most easily produced by conventional powder metallurgical techniques. There is also significant interest in other processing techniques (that do not require powder precursors) to produce ultrafine microstructures. Unlike powder metallurgical products, ultrafine microstructures produced by ingot metallurgical routes do not suffer with problems of lower ductility, residual porosity and higher processing costs.

Valiev et al. [1-4], Erbel [5], and Saunders and Nutting [6] have shown that microstructures as fine as 100 nm can be produced in metals and intermetallics without powder precursors. However, these processing techniques require large deformations (up to true strains of 7). This puts a serious limitation on the size of the product that can be formed with this processing technique. In addition most materials are incapable of sustaining such high strains under normal conditions and have to be deformed under high pressures to prevent premature fracture.

At this point we are aware of only two other processing techniques that can produce microstructures significantly finer than 1 μm without requiring powder precursors. One

of the techniques was developed by O. D. Sherby et al. [7-9] at Stanford for obtaining equiaxed grain microstructures as fine as 300 nm in ultra high carbon steels. The other processing technique was developed by Moore and Morris [10] of Alcan for obtaining 500 nm grain size microstructure in Al-5%Zn-5%Ca alloy. These techniques were briefly described in Chapter 1 of this thesis.

In Chapter 2, the collapse of microstructure in Fe-28Al-2Cr intermetallic compound from 80 nm to 10 nm was explained in the following manner: It was assumed that the formation of dislocation cells takes place during the early stages of deformation. However, the observed misorientation among the finer grains was significantly higher than predicted by calculations based on dislocation densities. This suggested operation of some other deformation mechanism that is capable of causing an increase in misorientation among the dislocation cells. The core mantel morphology in the finer grained microstructure suggested operation of a mechanism similar to grain boundary sliding. The operation of grain boundary sliding deformation mechanism was used to explain the increase in misorientation between the cells during deformation and the eventual conversion of dislocation cells into medium to high angle misorientation grains.

This provides an idea for the synthesis of ultrafine grain microstructures by ingot metallurgical route. The key steps for this processing route would involve (1) generation of a dislocation cell structure of same size (or finer) to finally desired grain size, and (2) activation of grain boundary sliding in this microstructure leading to conversion of dislocation cells into grains with high angle boundaries. The aim of research described in this chapter was to investigate whether ultrafine grain materials can be synthesized in bulk form by a processing technique based on the above described hypothesis.

During our preliminary investigation, we observed that a significant fraction ($\approx$ 50%) of the microstructure of heavily deformed (at RT) 304 stainless steel after annealing at

500°C consisted of very fine cellular structure. The cell boundaries were quite sharp and the average cell size was approximately 100 nm. Hence 304 stainless steel was chosen as a candidate material for this study.

Grain boundary sliding is often used to explain superplasticity in materials. Mechanical behavior of polycrystalline materials, when governed by grain boundary sliding (GBS) mechanisms, is generally described by the following equation [11-15,21],

$$\dot{\epsilon} = A\frac{DGb}{kT}(\frac{b}{d})^p(\frac{\sigma}{G})^n, \tag{1}$$

where $\dot{\epsilon}$ is the strain rate, A is a mechanism dependent constant, D is the appropriate temperature dependent diffusion constant, G is the shear modulus, T is the temperature, b is the burgers vector, d is the grain size, σ is the stress, p is a grain size exponent that ranges from 1 to 3 depending on the mechanism, and n is the stress exponent that also ranges from 1 to 2 depending on the model. It is clear from Equation (1) that stress required for grain boundary sliding decreases with decreasing grain size for a given strain rate and temperature or decrease in grain size would result in decrease in temperature at which deformation can take place at a given stress and strain rate.

In general, grain boundary sliding and dislocation creep mechanisms are diffusive in nature and operate at higher temperatures as compared to dislocation glide that operates at lower temperatures for similar strain rates. The success of this processing technique will depend on the existence of a temperature and strain rate window (for a given material) in which the following two conditions are satisfied: (1) grain boundary sliding is the predominant mechanism of deformation, and (2) significant grain and/or cell growth does not take place during deformation. Grain boundary sliding is required to convert dislocation cells into grains and significant grain growth during processing may result

in change in deformation mechanism (equation 1) to dislocation glide or creep. *This suggests that the second step of processing should be carried out at lowest possible temperatures (to prevent grain growth) where grain boundary sliding can operate at strain rates to complete the processing in a reasonable amount of time.*

4.2 EXPERIMENTS and RESULTS

4.2.1 Material and Microstructural Characterization

The starting material for this investigation was a commercial grade 304 stainless steel (304 SS). A 3/8" diameter rod of 304 stainless steel was obtained from the central warehouse at Caltech. A small piece of this steel was embedded in epoxy and polished to 6 μm diamond paste. The polished sample was etched by 25% HNO_3, 25% CH_3COOH, 37.5% HCl and 12.5% Glycerol solution to delineate the grain boundaries. The microstructure was examined optically using a Nikon microscope. An optical micrograph of the 304 SS in as-received condition is shown in Figure 4.1. 304 SS in the as-received condition had an average grain size of $\approx$200μm. The x-ray diffraction pattern of the as-received stainless steel collected on an Inel CPS-120 diffractometer system (as described in Chapter 2), is shown in Figure 2.1. The peaks from both bcc and fcc phases are visible in the x-ray diffraction pattern.

The samples for TEM examination (of 304 stainless steel) were made by electro-jet-thinning at -35^{o}C in a 95% methyl alcohol and 5% perchloric acid solution at 35 V and 64 mA. The microstructures were examined on Philips EM301 microscope operating at 100kV.

4.2.2 Processing of Ultrafine Cellular Structure

The 304 SS rod (3/8" in dia) was initially rolled 63% at room temperature to an ingot with

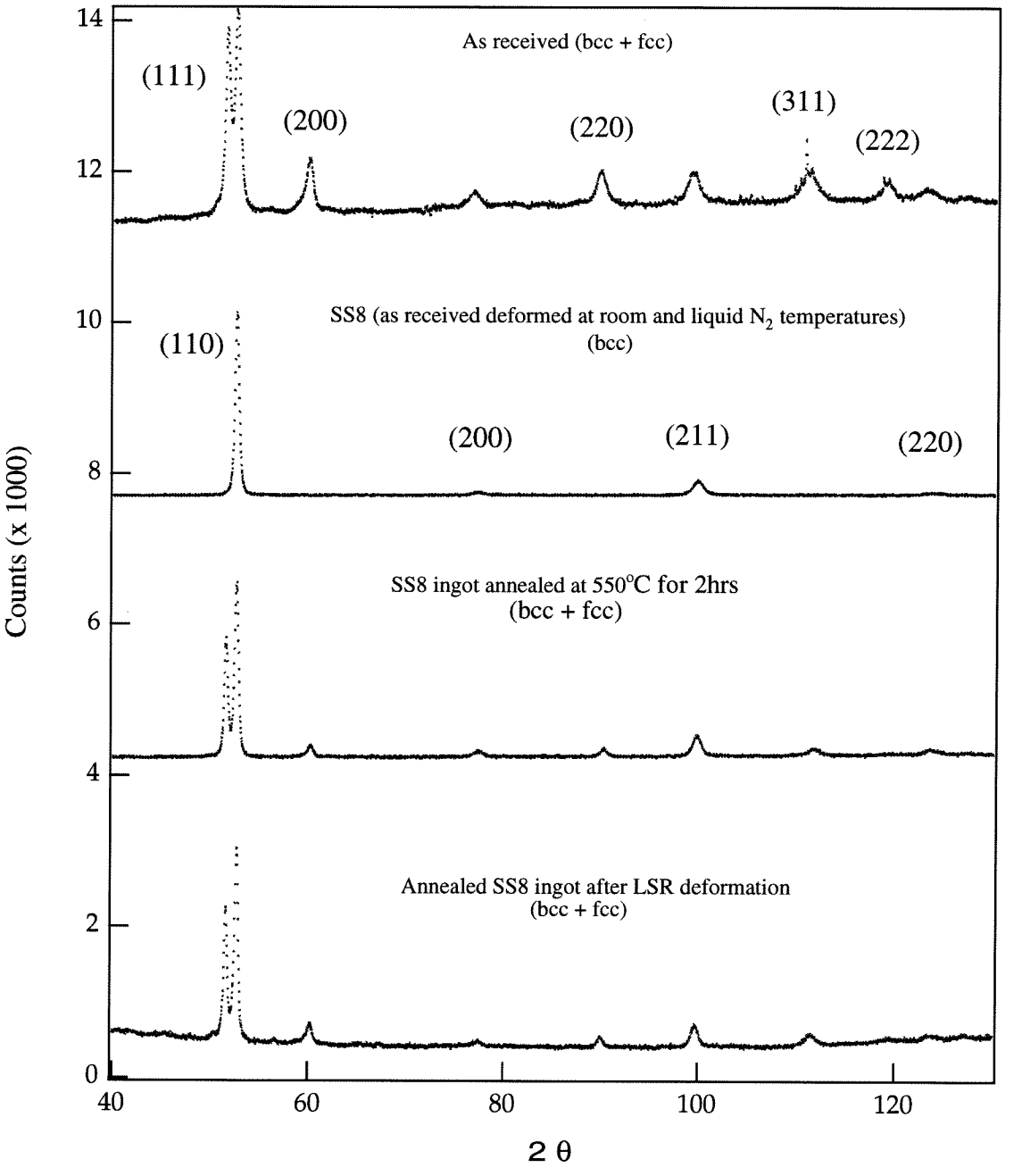

Figure 4.2 X-ray diffraction pattern of 304 stainless steel in as received condition, after deformation at room and liquid N_2 temperature, after annealing at 575°C for 2hrs and after LSR deformation on annealed SS8 ingot.

then immediately rolled. It was found that 304SS becomes very hard at liquid nitrogen temperature and the diagonal of the ingot could be reduced only 0.005"/pass with rolling mill used in the experiment. The ingot was soaked in liquid nitrogen (recooled) after each pass as previously described. The rolling at liquid nitrogen temperature was followed by rolling at room temperature to reduce the cross section to 0.105" $\times$ 0.105". The room temperature deformation was carried out to form ingot into dimensions that are easier to handle during further processing. The total deformation up to this point corresponds to a total strain of 90%. The ingot obtained in this manner will be referred to as SS8 in the rest of the chapter.

The microstructure of the SS8 ingot was examined by TEM and x-ray diffraction in both directions, i.e., in the planes parallel and perpendicular to the axis of rolling. X-ray diffraction scans as obtained by INEL diffractometer are shown in Figure 4.2. The microstructure as examined by TEM is shown in Figure 4.3. The microstructure has a lath morphology, which is quite typical of phases formed by martensitic phase transformations. Furthermore, the morphology of microstructure is approximately the same in both directions, i.e., in the planes perpendicular and parallel to the axis of rolling. However, the martensite phase is extremely fine with laths ranging from 50-100 nm in width and 500-1000 nm in length.

The SS8 ingot was then annealed at 575^{o}C for 2 hrs. The XRD scans of this ingot in planes parallel and perpendicular to the axis of rolling are shown in Figure 4.4. Comparisons of these XRD scans reveal that there is a noticeable difference in the ratio of peak heights from one XRD scan to another. This suggests that microstructure of annealed SS8 ingot is textured. The TEM micrographs are shown in Figure 4.5 and 4.6. The microstructure perpendicular to the axis of rolling appears to consist mostly of equiaxed grains ranging in size from 100-300 nm (Figure 4.5), while the microstructure parallel

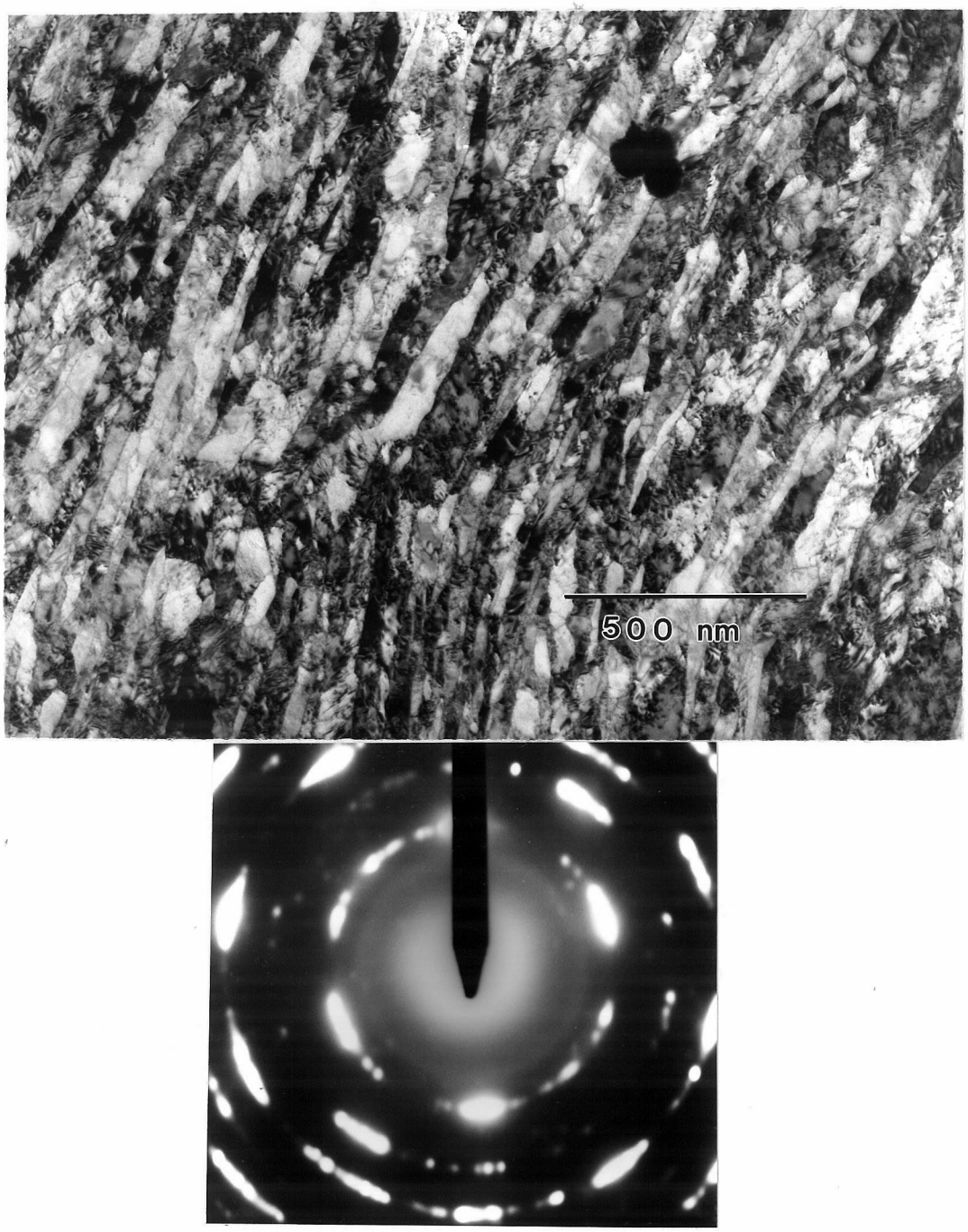

Figure 4.3 Microstructure of 304 stainless steel rolled 63% at room temperature and 65% at liquid N_2 temperature: (a) BF image, (b) Selected area diffraction pattern. The microstructure has lath morphology and consists entirely of BCC phase.

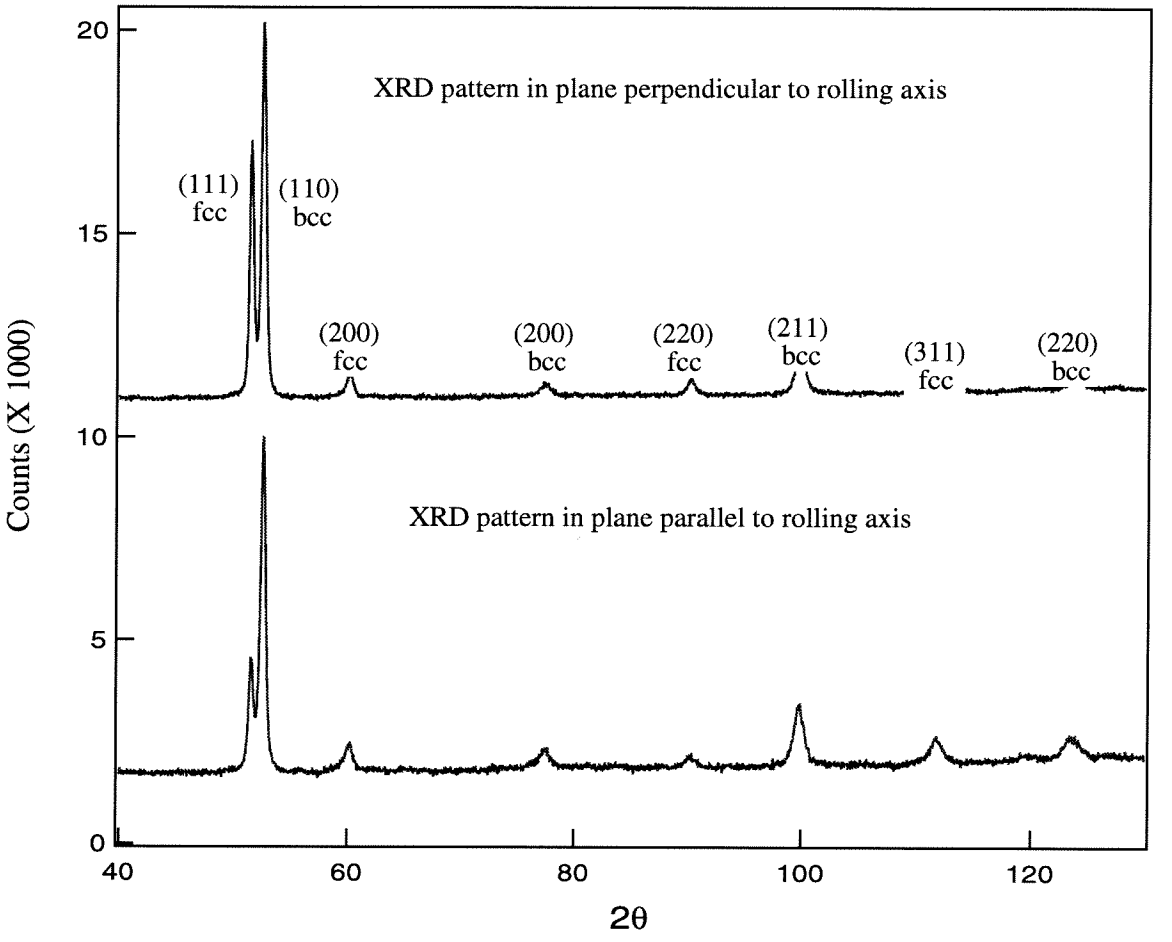

Figure 4.4 X-ray diffraction patterns of SS8 ingot annealed at 575°C for 2 hrs in planes parallel and perpendicular to the axis of rolling.

to the axis of rolling consists of elongated grain with equiaxed cellular structure inside them (Figure 4.6). The elongated grains range 100-300 nm in width and 1000-2000 nm in length and are aligned parallel to the axis of rolling. These microstructural observations indicate that microstructure of annealed SS8 consists of long columnar grains mostly aligned parallel to the axis of rolling. In addition, these columnar grains contain equiaxed cellular structure with sharp cell boundaries. The size of the cells ranges from 100-300 nm and the average cell size is $\approx$200 nm.

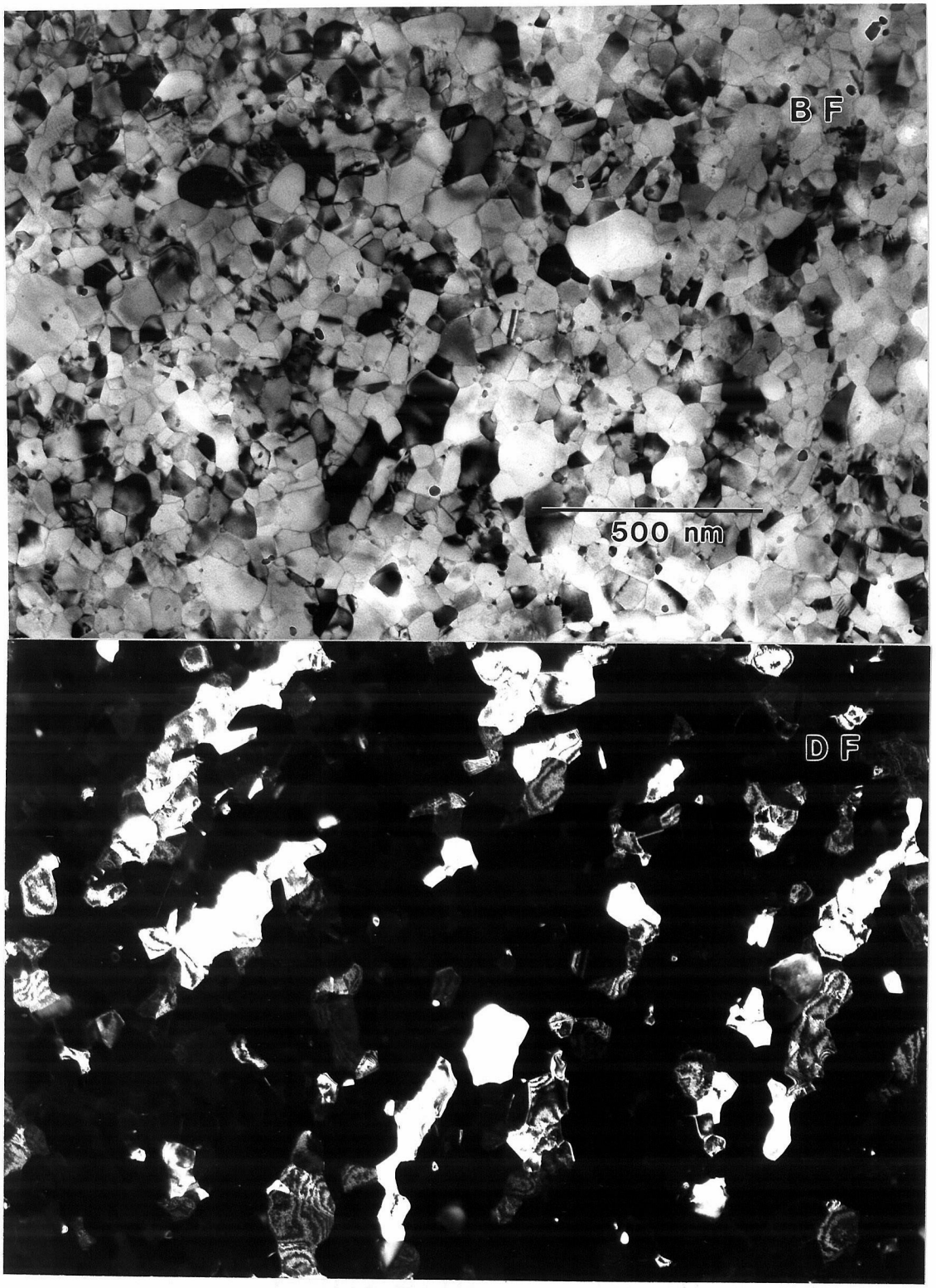

Figure 4.5 Microstructure of the SS8 ingot annealed at 575°C for 2hrs in the plane perpendicular to the axis of rolling: (a) BF, (b) DF.

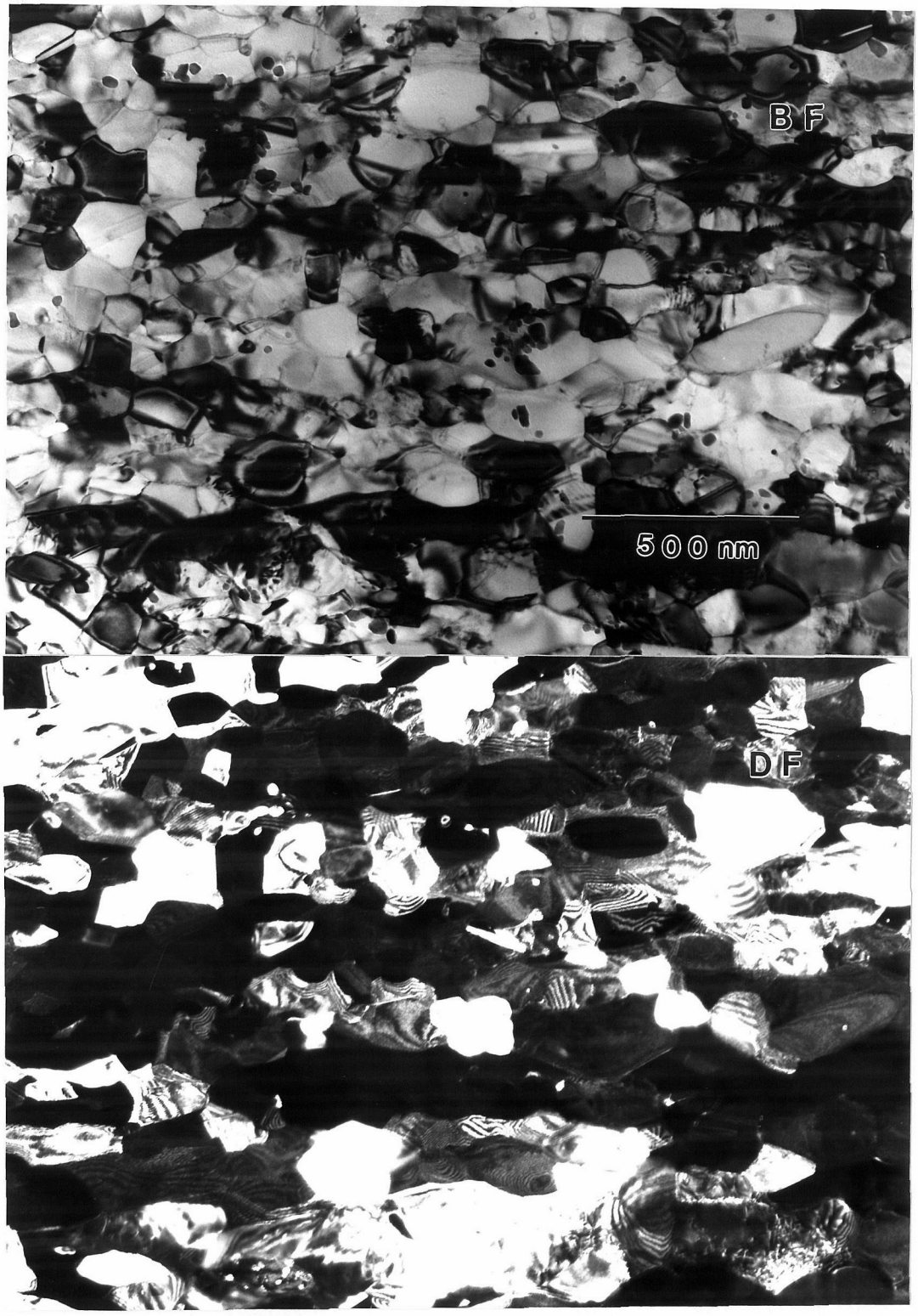

Figure 4.6 Microstructure of the SS8 ingot annealed at 575°C for 2hrs in the plane parallel to the axis of rolling: (a) BF, (b) DF. Comparison with Figure 4.5 reveals the columnar morphology of the microstructure. The columnar grains are aligned parallel to the axis of rolling and contain equiaxed cellular structure.

4.2.3 Low Strain Rate (LSR) Deformation Processing

Several nearly cubical samples were cut out of the annealed SS8 ingot for compression testing. These samples were deformed in compression (opposite to the direction of rolling) at temperatures ranging from 24°C (room temperature) to 575°C at the crosshead speed of 0.0002"/min. This corresponded to nominal strain rate of $\approx 4.4 \times 10^{-5}$ sec^{-1}. A flow stress versus deformation temperature plot for the annealed SS8 ingot at temperatures ranging from 24°C to 575°C is shown in Figure 4.7. The flow stress decreases very slowly from room temperature to about 500°C and decreases abruptly thereafter.

The compression tests were conducted in the following manner. The sample was first sandwiched between two tungsten carbide (WC) discs. WC discs were painted with a high temperature lubricant to minimize friction between the sample and WC discs during the test. The sandwiched sample was then placed between the loading bar and the load cell. A tube furnace was then placed around it. All these steps were carried out at room temperature. The furnace was then heated to the desired temperature. The heating from room temperature to 550°C (the temperature at which most of the mechanical testing described in this chapter was carried out) took approximately 35 to 40 minutes. The temperature was then allowed to homogenize for approximately 10 minutes before the compression test was started at the desired crosshead speed. The load and displacement data during the test was collected through a computer that was linked to load frame. Unloading of the samples was carried out at the crosshead speed of 0.02"/min. The unloading typically took less than 2 minutes. The furnace was immediately removed, sample was unsandwiched and air quenched.

The microstructures after the low strain rate (LSR) deformation were examined by TEM in both directions, i.e., in the planes perpendicular as well as parallel to the axis of rolling. Note that LSR deformation was carried out opposite to the direction of rolling

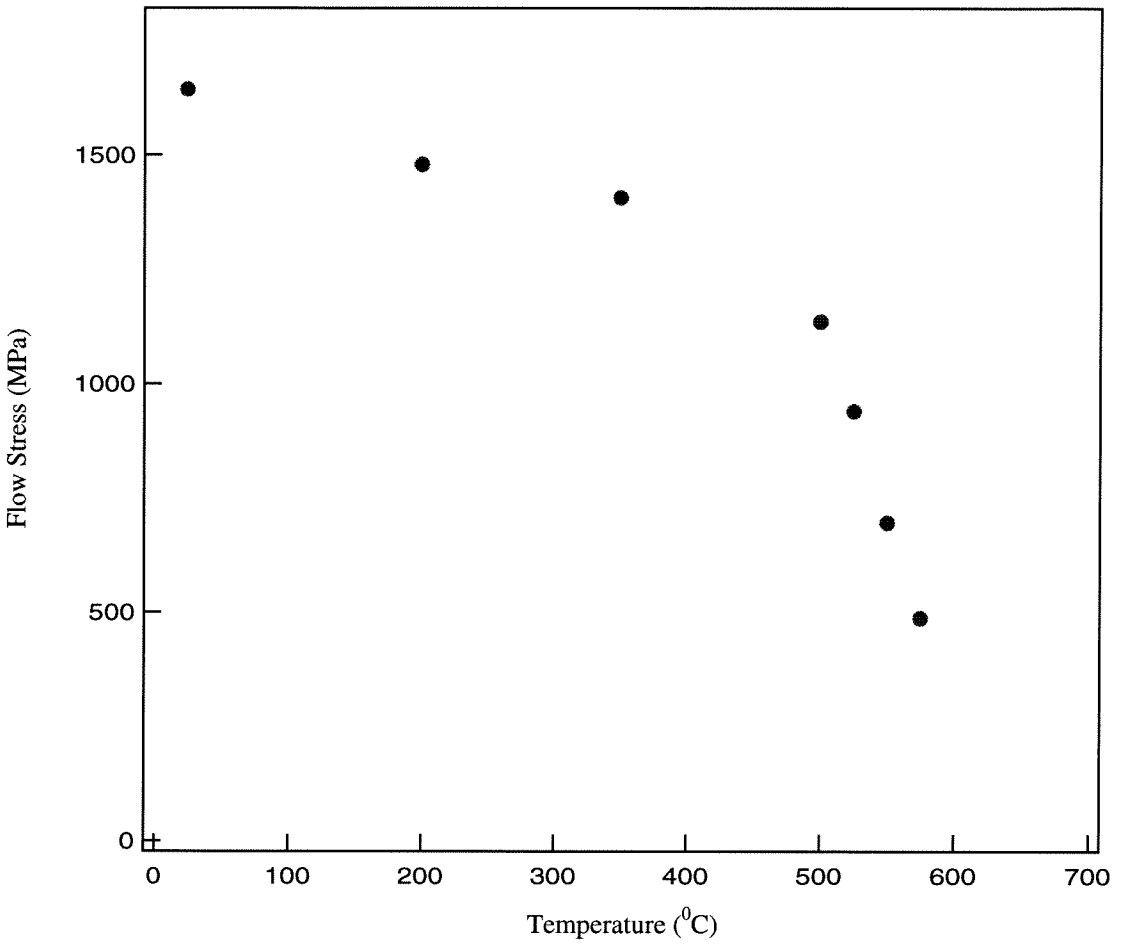

Figure 4.7 Flow stress vs temperature curve for annealed SS8 ingot deformed at the nominal strain rate of $\approx 4.4 \times 10^{-5}$ sec^{-1}. Note that the flow stress drops abruptly after 500°C.

deformation. The representative microstructure of the annealed SS8 sample deformed at 550°C and the crosshead speed of 0.0002"/min (nominal strain rate 4.4×10^{-5} sec^{-1}) is shown in Figure 4.8 and 4.9. The microstructure after deformation at 550°C and nominal strain rate 4.4×10^{-5} sec^{-1} consists primarily of equiaxed grains ranging from 100-300 nm with the average grain size of $\approx$200 nm (Figure 4.8,4.9). The microstructure was similar in both directions and dislocation density in the microstructure was quite low.

The microstructure parallel to the axis of the rolling of the annealed SS8 sample that was deformed at 450°C and nominal strain rate of 4.4 $\times$ 10^{-5} sec^{-1} (crosshead speed 0.0002"/min) is shown in Figure 4.10. In contrast to the microstructure of SS8 sample deformed at 550°C this microstructure consists primarily of elongated grains similar to observed before LSR deformation.

During the compression test at 550°C the sample spent approximately 7 hrs in the furnace (including the heating time). In addition, SS8 ingot was annealed at 575°C for two hrs prior to compression testing, so the sample spent approximately 9 hrs significantly above room temperature. Therefore, for the purpose of comparison a small piece of SS8 ingot was annealed at 575°C for 12 hrs. The microstructure of this ingot was examined in the plane parallel to the axis of rolling by TEM. The representative micrographs are shown in Figure 4.11. The microstructure after 12 hrs of annealing consists mostly of elongated grains with cellular structure and is very similar to microstructure after two hrs of annealing.

To examine the effect of strain rate on grain refinement process a sample from the SS8 ingot annealed for 2 hrs at 575°C was deformed at the crosshead speeds of 0.002"/min and 0.02"/min. This corresponds to nominal strain rate of $\approx$4.4 $\times$ 10^{-4} sec^{-1} for the crosshead speed of 0.002"/min and nominal strain rate of $\approx$4.4 $\times$ 10^{-3} sec^{-1} for the crosshead speed of 0.02"/min. The microstructures were again examined by TEM in both directions, i.e., in the planes parallel as well as perpendicular to the axis of rolling. The micrographs representative of the microstructure are shown in Figures 4.12 to 4.14. It is clear from Figure 4.12 and 4.13 that the microstructure after deformation at the crosshead speed of 0.002"/min (i.e., nominal strain rate of 4.4 $\times$ 10^{-4} sec^{-1}) consists primarily of equiaxed grains in both directions. This microstructure is very similar to that

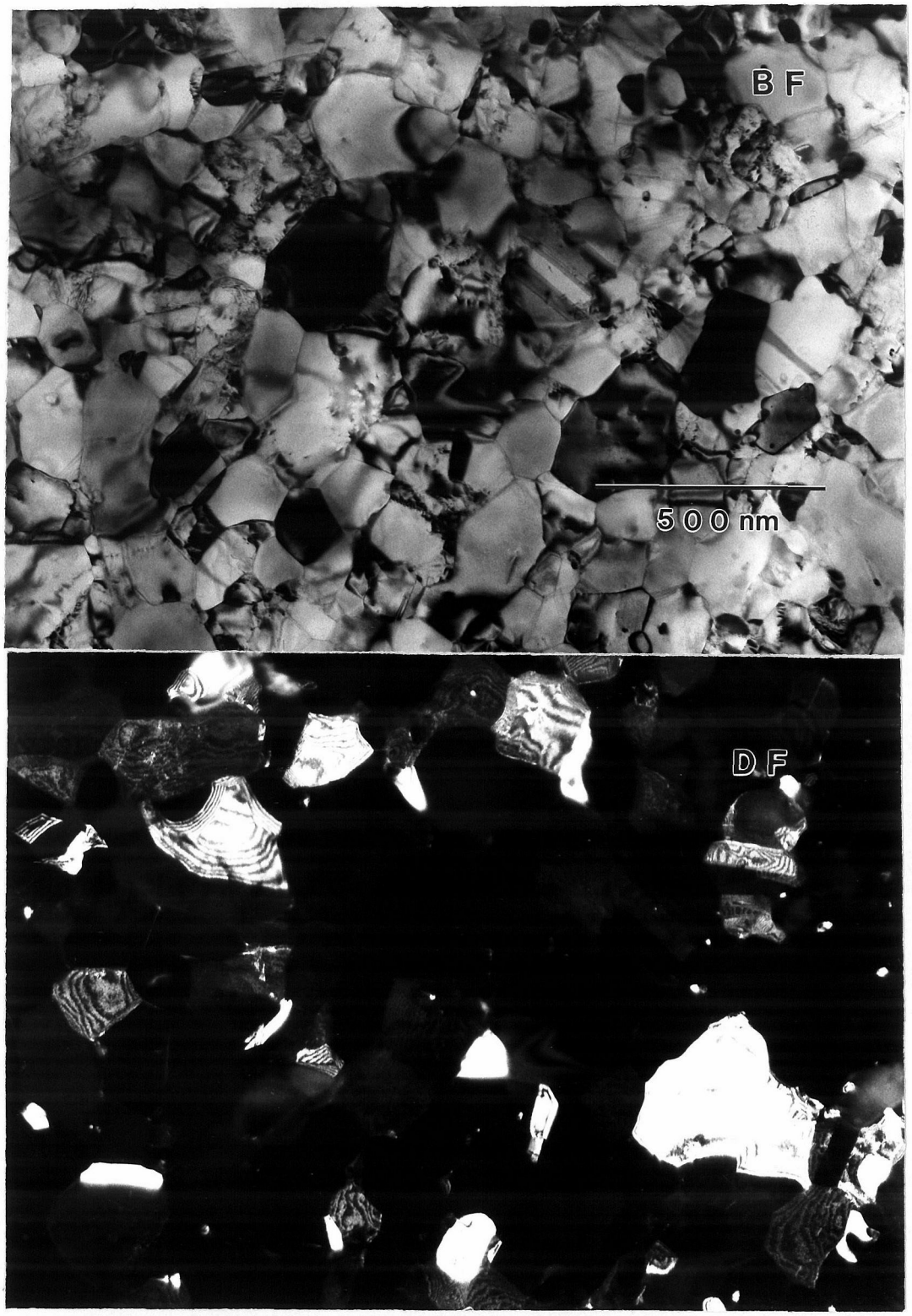

Figure 4.8 Microstructure in the plane perpendicular to the axis of rolling for the annealed SS8 ingot deformed at 550°C and nominal strain rate of $\approx 4.4 \times 10^{-5}$ sec^{-1}: (a) BF, (b) DF.

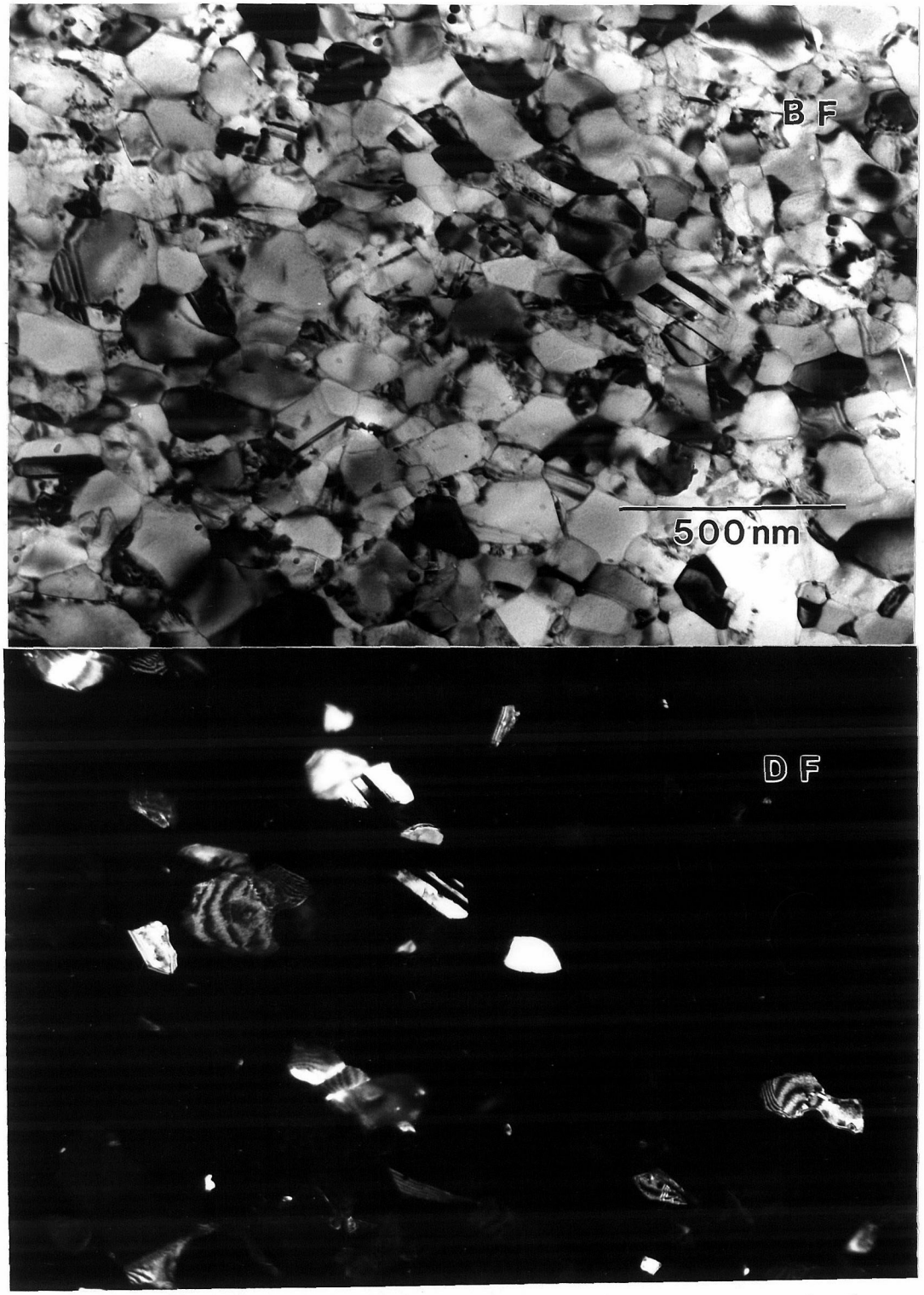

Figure 4.9 Microstructure in the plane parallel to the axis of rolling for the annealed SS8 ingot deformed at 550°C and nominal strain rate of ≈4.4 $\times$ 10^{-5} sec^{-1}: (a) BF, (b)DF. Comparison with Figure 4.8 reveals that grains are equiaxed, also note the low defect density in the microstructure.

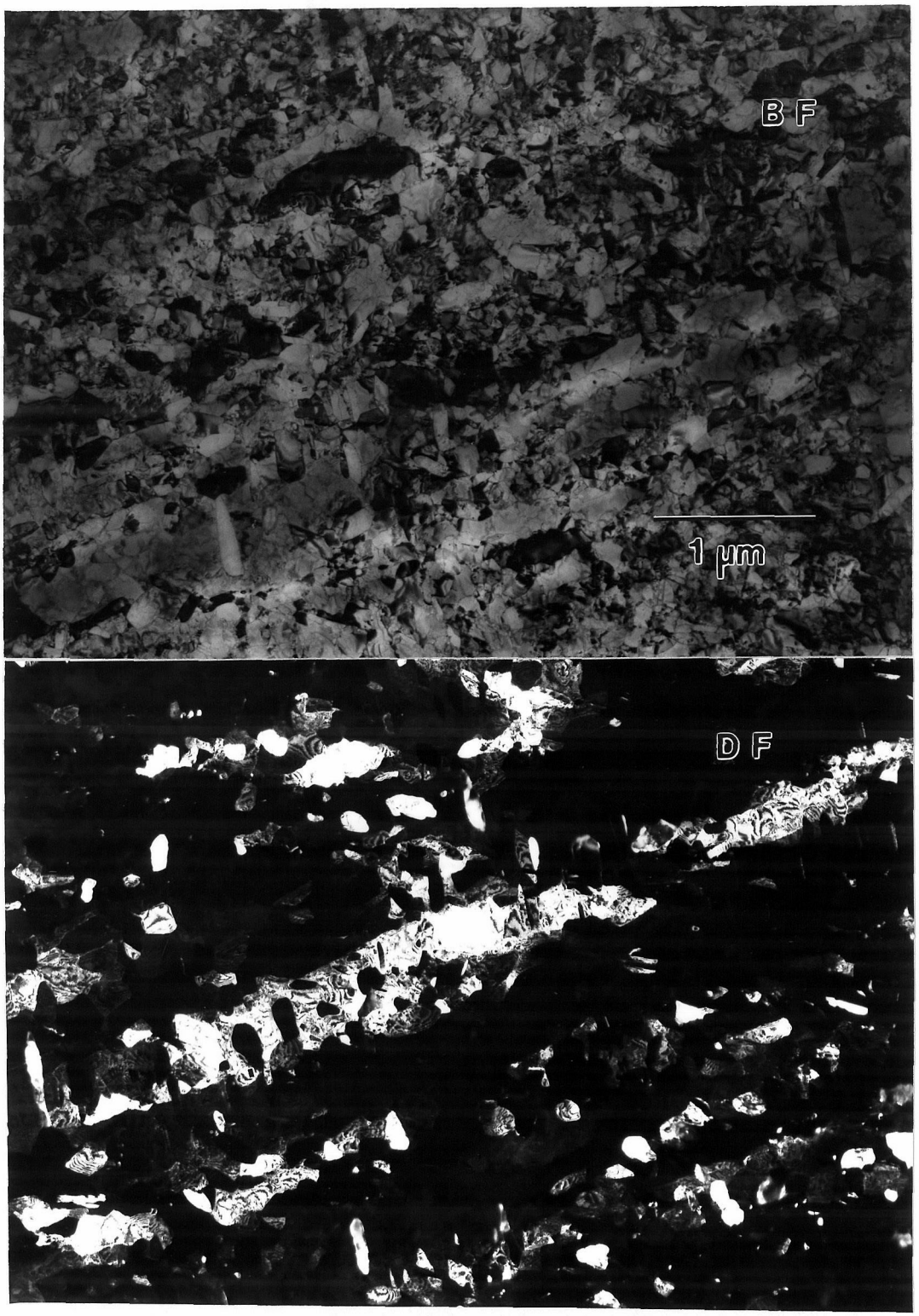

Figure 4.10 Microstructure in the plane parallel to the axis of rolling for the annealed SS8 ingot deformed at 450°C and nominal strain rate of ≈4.4 $\times$ 10^{-5} sec^{-1}: (a) BF, (b) DF. Note the columnar morphology similar to that of annealed SS8 ingot (Figure 4.6).

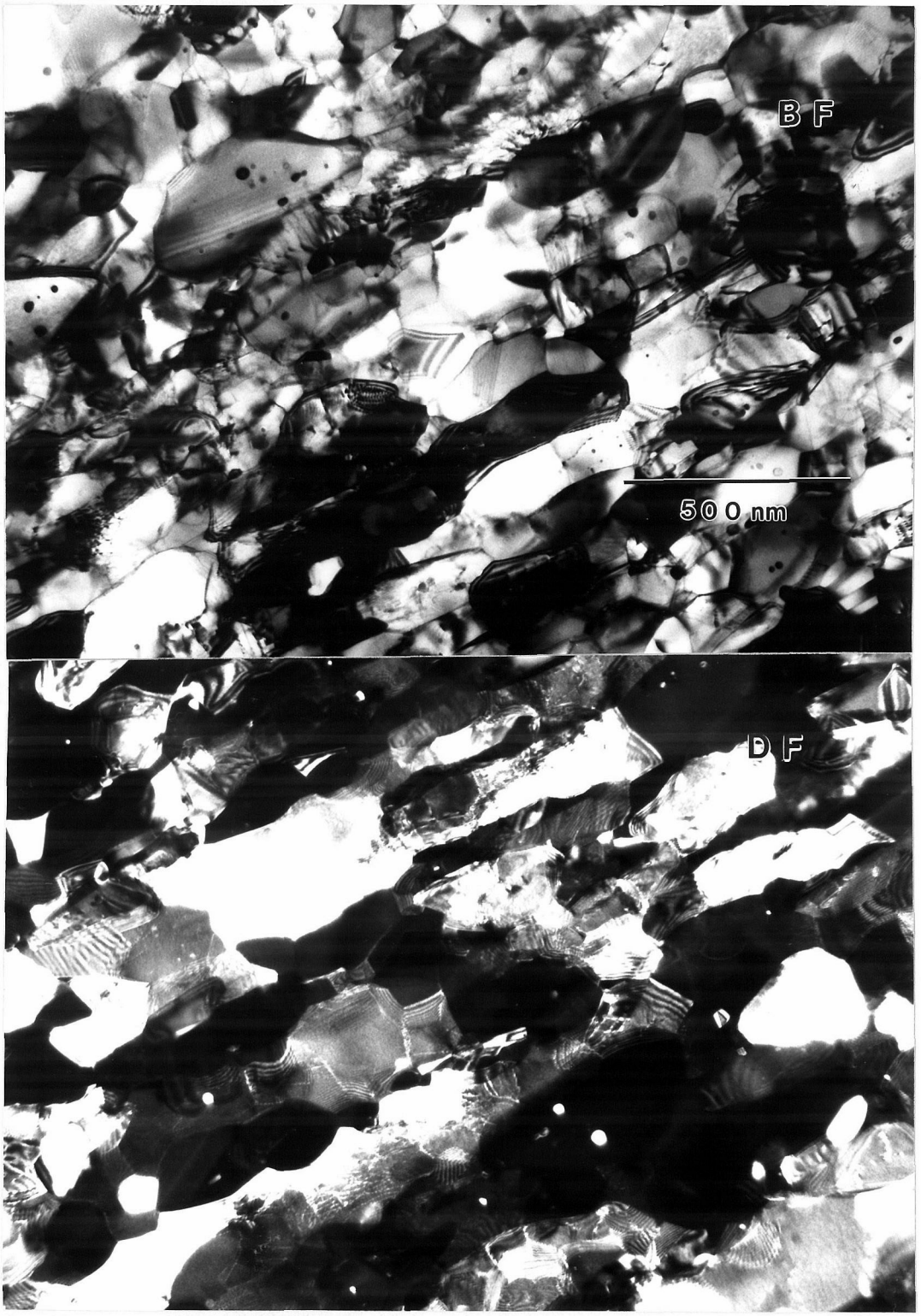

Figure 4.11 Microstructure in the plane parallel to the axis of rolling for the SS8 ingot annealed at 575°C for 12hrs: (a) BF, (b) DF. The longer annealing time does not result in any change in the morphology of the microstructure.

after deformation at the crosshead speed of 0.0002"/min (nominal strain rate 4.4 $\times$ 10^{-5} sec^{-1}) with average grain size of approximately 200 nm. However, the microstructure (Figure 4.14) after LSR deformation at the crosshead speed of 0.02"/min (nominal strain rate 4.4 $\times$ 10^{-3} sec^{-1}) consists mostly of smaller columnar grains (compared to annealed SS8 ingot) and a small fraction consists of equiaxed grains. The investigation for the crosshead speeds higher than 0.02"/min could not be conducted as the samples sheared very early during the deformation.

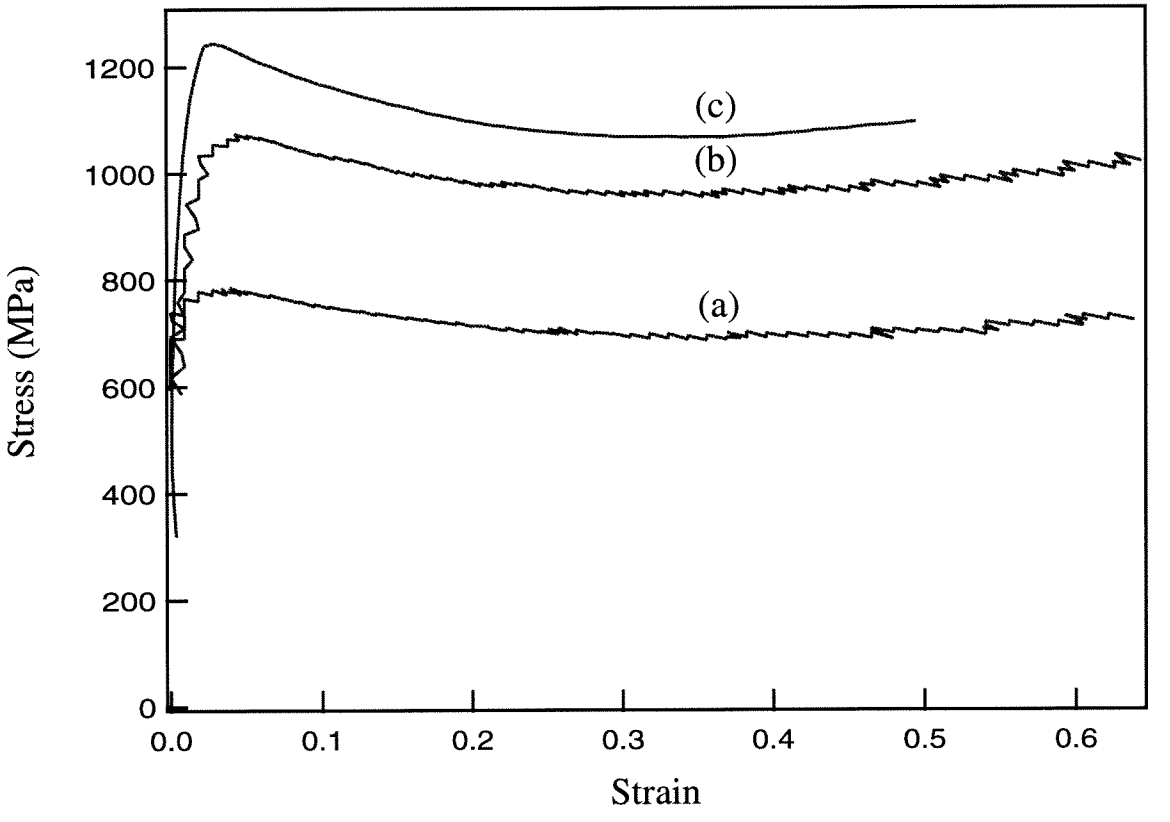

Figure 4.15 Stress-strain response of annealed SS8 ingot at 550°C and nominal strain rates of (a) 4.65 $\times$ 10^{-5} (b) 4.65 $\times$ 10^{-4} (c) 4.65 $\times$ 10^{-3}.

Several samples from the annealed SS8 ingot were deformed at 550°C and crosshead

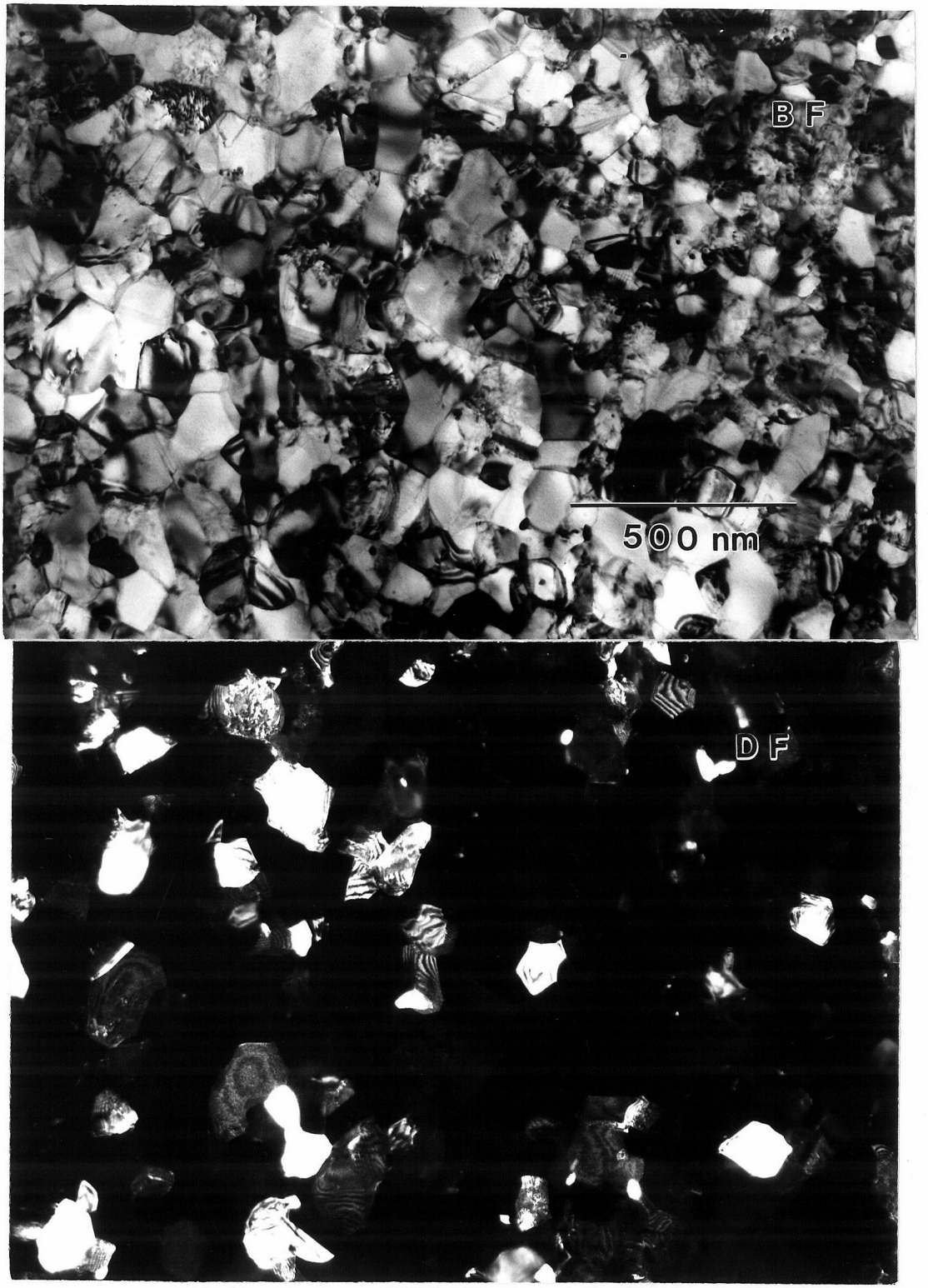

Figure 4.12 Microstructure in the plane perpendicular to the axis of rolling for the annealed SS8 ingot deformed at 550°C and nominal strain rate of $\approx 4.4 \times 10^{-4}$ sec^{-1}: (a) BF, (b) DF.

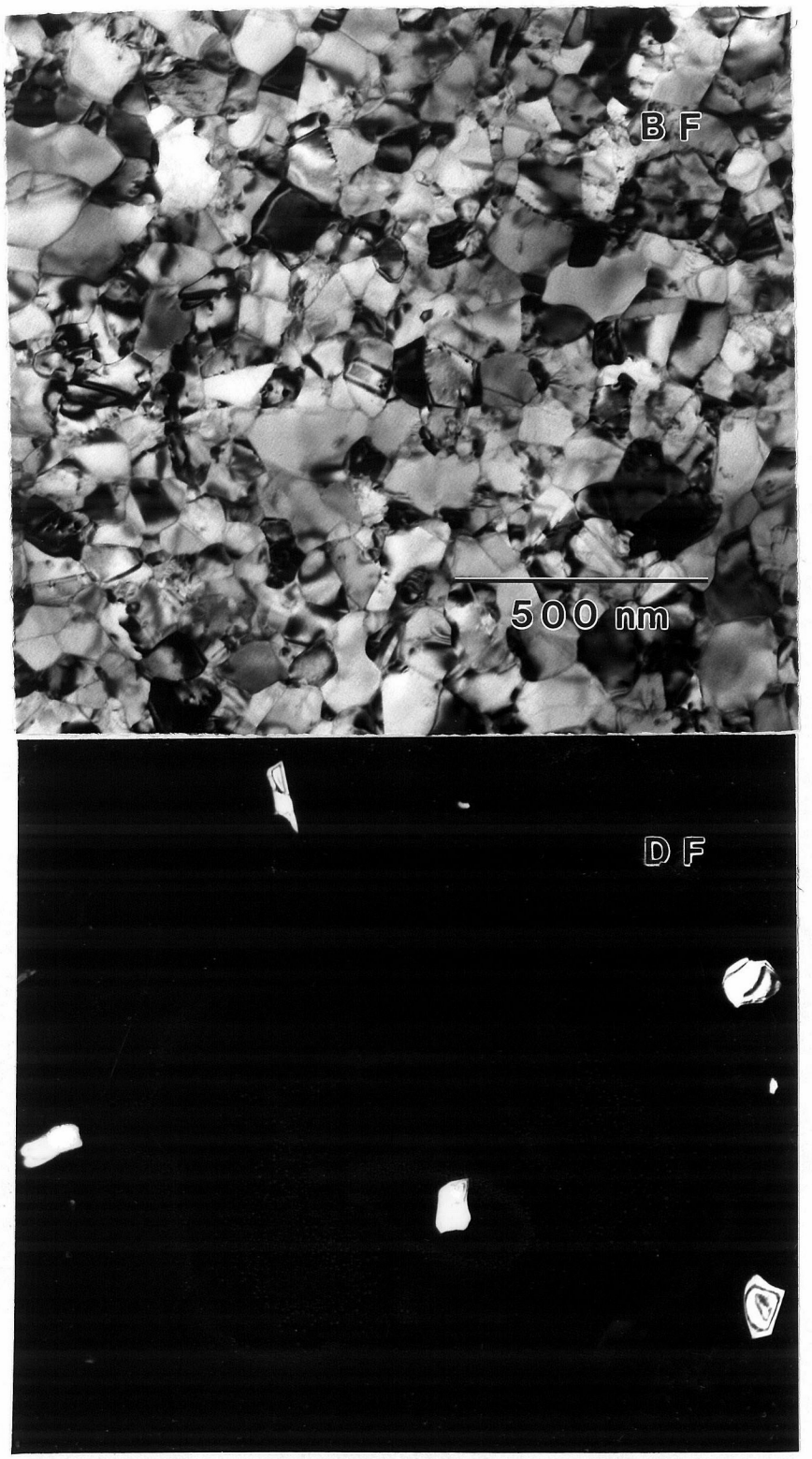

Figure 4.13 Microstructure in the plane parallel to the axis of rolling for the annealed SS8 ingot deformed at 550°C and nominal strain rate of ≈4.4 $\times$ 10^{-4} sec^{-1}: (a) BF, (b) DF. Notice the equiaxed grain microstructure and low defect density.

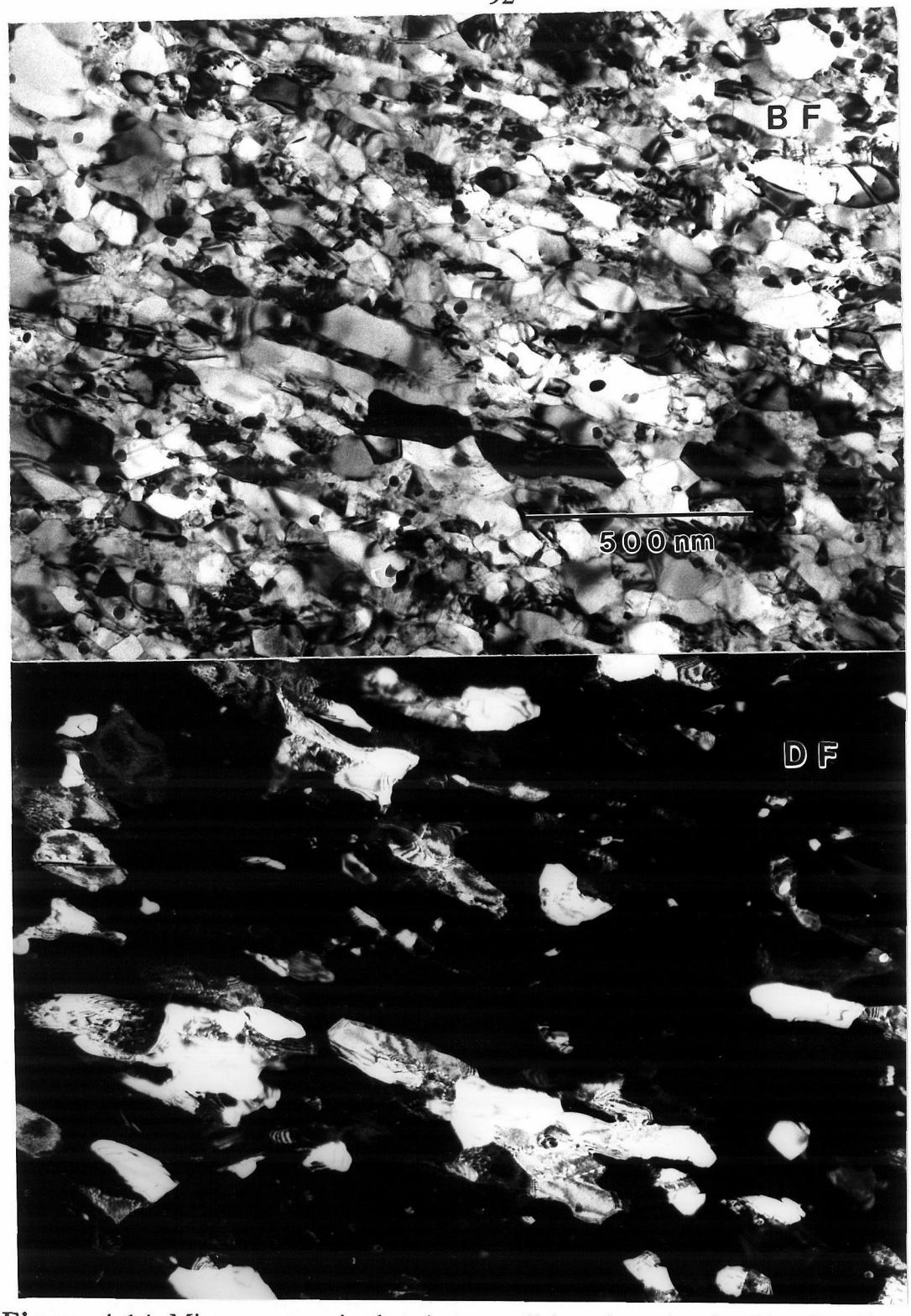

Figure 4.14 Microstructure in the plane parallel to the axis of rolling for the annealed SS8 ingot deformed at 550°C and nominal strain rate of ≈4.4 $\times$ 10^{-3} sec^{-1}: (a) BF, (b) DF. Notice the partially broken elongated grains and some equiaxed grains. The defect density also appears to be higher compared to samples deformed at lower strain rates (Figure 4.8-4.9 and Figure 4.12-4.13).

speeds ranging from 0.0001"/min to 0.02"/min. These crosshead speeds correspond to strain rates ranging from 1.47×10^{-5} to 3.0×10^{-3} sec^{-1}. Some of the representative stress strain curves in compression are shown in Figure 4.15. The shapes of the stress strain curves in the strain rate range of 1.47×10^{-5} to 3.1×10^{-4} sec^{-1} were very similar to each other, i.e., the flow stress decreased slowly after yielding, then plateaus around strain of 30% and starts rising at true strains of about 50%. The rise in the flow stress towards the end of the test is probably due to frictional effects as the aspect ratio of the samples is below 0.5 at this point. Figure 4.16 plots the plateau stress (flow stress at 30% strain) against the instantaneous strain rate on a log-log scale, for annealed SS8 ingot during deformation at 550°C. The experimental data in the strain rate range of 1.47×10^{-5} to 3.1×10^{-4} sec^{-1} falls on a straight line with a corresponding stress exponent of n = 5.76. However, one data point for strain rate above 3.1×10^{-4} sec^{-1} does not fall on this line. Microstructure of the sample deformed at this strain rate was examined in the plane parallel to the axis of rolling by TEM. This microstructure is shown in Figure 4.14 and it consists mostly of elongated grains that are about 200 nm wide and about 500-700 nm long. These grains are aligned parallel to the direction of rolling and are smaller (in length) compared to grains in annealed SS8 ingot before the LSR deformation.

A SS8 sample that was annealed at 575°C for 2 hrs was also deformed at the crosshead speed of 0.002"/min (nominal strain rate 4.4×10^{-4}) at room temperature to a strain of ≈40%. This sample was then annealed for 1.5 hrs (including the heating time) at 550°C in the same furnace that was used for the compression testing. The annealing time of 1.5 hr was chosen, because the total time spent by the sample in furnace during the compression testing at the crosshead speed of 0.002"/min (nominal strain rate 4.4×10^{-4} sec^{-1}) was always slightly less than 90 minutes. The microstructure in the

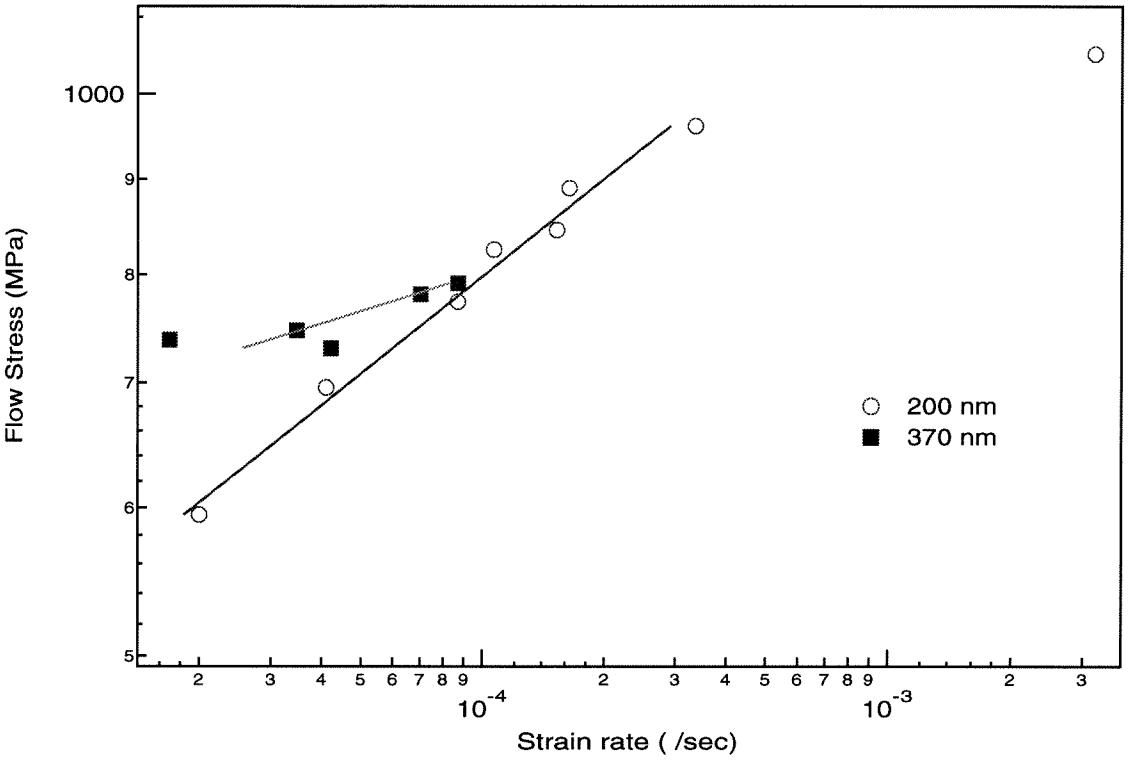

Figure 4.16 Flow stress vs strain rate plot for 200 nm and 370 nm 304 stainless steel. Note that the stress exponent for steel with grain size of 370 nm is higher than that with grain size of 200 nm.

plane parallel to the axis of rolling was examined by TEM and is shown in Figure 4.17. The microstructure consists mostly of grains with cellular structure and some pancaked grains approximately 150 nm in size. In addition, the microstructure has considerable dislocation density. It should be noted that this microstructure is very different from the microstructure of the sample that was deformed at 550°C and crosshead speed of 0.002"/min (nominal strain rate 4.4×10^{-4} sec^{-1}).

Figure 4.18 shows the selected area diffraction patterns from the same aperture of microstructures before and after deformation at the crosshead speeds of 0.0002"/min, 0.002"/min and 0.02"/min, i.e., nominal strain rates of 4.65×10^{-5} sec^{-1}, 4.65×10^{-4}

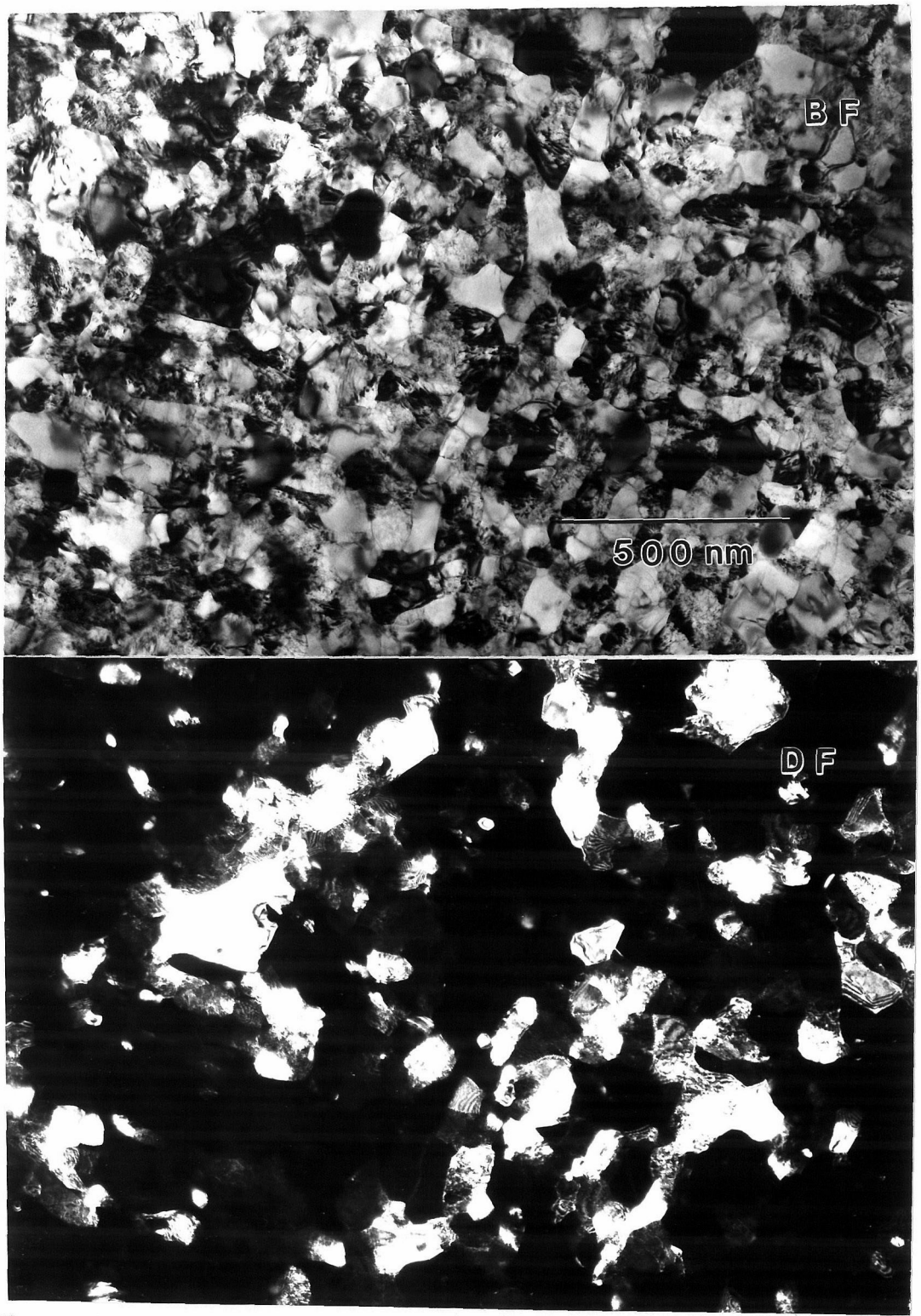

Figure 4.17 Microstructure in the plane parallel to the axis of rolling for the annealed SS8 ingot deformed at 22°C and nominal strain rate of $\approx 4.4 \times 10^{-4}$ sec^{-1}, and followed by annealing for 90 mins (including heating time) at 550°C: (a) BF, (b) DF. Note the very high dislocation density and absence of equiaxed grain microstructure.

sec^{-1} and 4.65 $\times$ 10^{-3} sec^{-1} respectively.

One sample from the annealed SS8 ingot was deformed in the same direction as rolling deformation at 550°C and crosshead speed of 0.0002"/min (nominal strain rate 4.0 $\times$ 10^{-5} sec^{-1}). The microstructure after this deformation was examined in the plane parallel to the axis of rolling by TEM. The microstructure after deformation was a mixture of columnar grains with dislocation cells (although columnar grains were smaller than those in annealed SS8 ingot), and equiaxed grains approximately 200 nm in diameter. The dark field micrographs of these microstructures are shown in Figures 4.19a and 4.19b respectively.

4.2.4 Determination of Mass Fractions of Bcc and Fcc Phases

The mass fractions of bcc and fcc phases after various stages of processing were determined by measuring magnetic moments in a constant magnetic field by a "Vibrating Sample Magnetometer". The magnetometer used in the present investigation operates on the following principle: a sample is allowed to vibrate in a homogeneous magnetic field. The direction of vibration is kept perpendicular to the applied magnetic field. The homogeneous magnetic field magnetizes the sample and the vibration of magnetized sample induces a voltage in the inductor coils placed around the sample. This induced voltage can be easily measured and it is directly proportional to the magnetic moment of the sample. The details of the operating principle for a Vibrating Sample Magnetometer are described in Reference 16.

The magnetic moments (induced voltages) of samples at various stages of processing were measured in two orientations: (i) with rolling axis in the horizontal plane, and (ii) with rolling axis in the vertical plane (in this case rolling axis is perpendicular to the applied magnetic field). These magnetic moments are listed in Table 4.1 and 4.2 respectively.

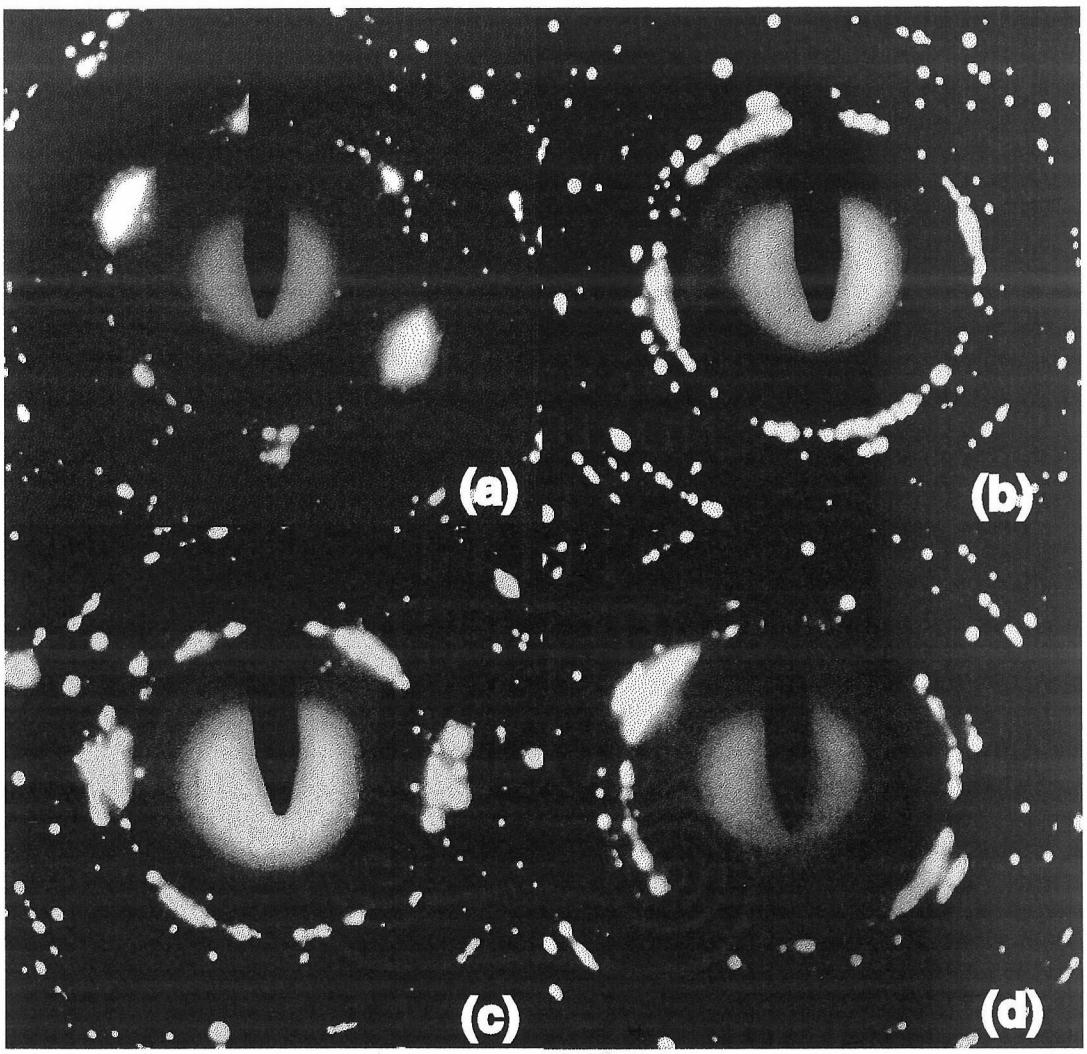

Figure 4.18 Selected area diffraction patterns (aperture size $\approx 0.75\ \mu m^2$) of (a) annealed SS8 ingot and after LSR deformation at average strain rates of (b) 4.65×10^{-5} (c) 4.65×10^{-4} (d) 4.65×10^{-3} sec^{-1}.

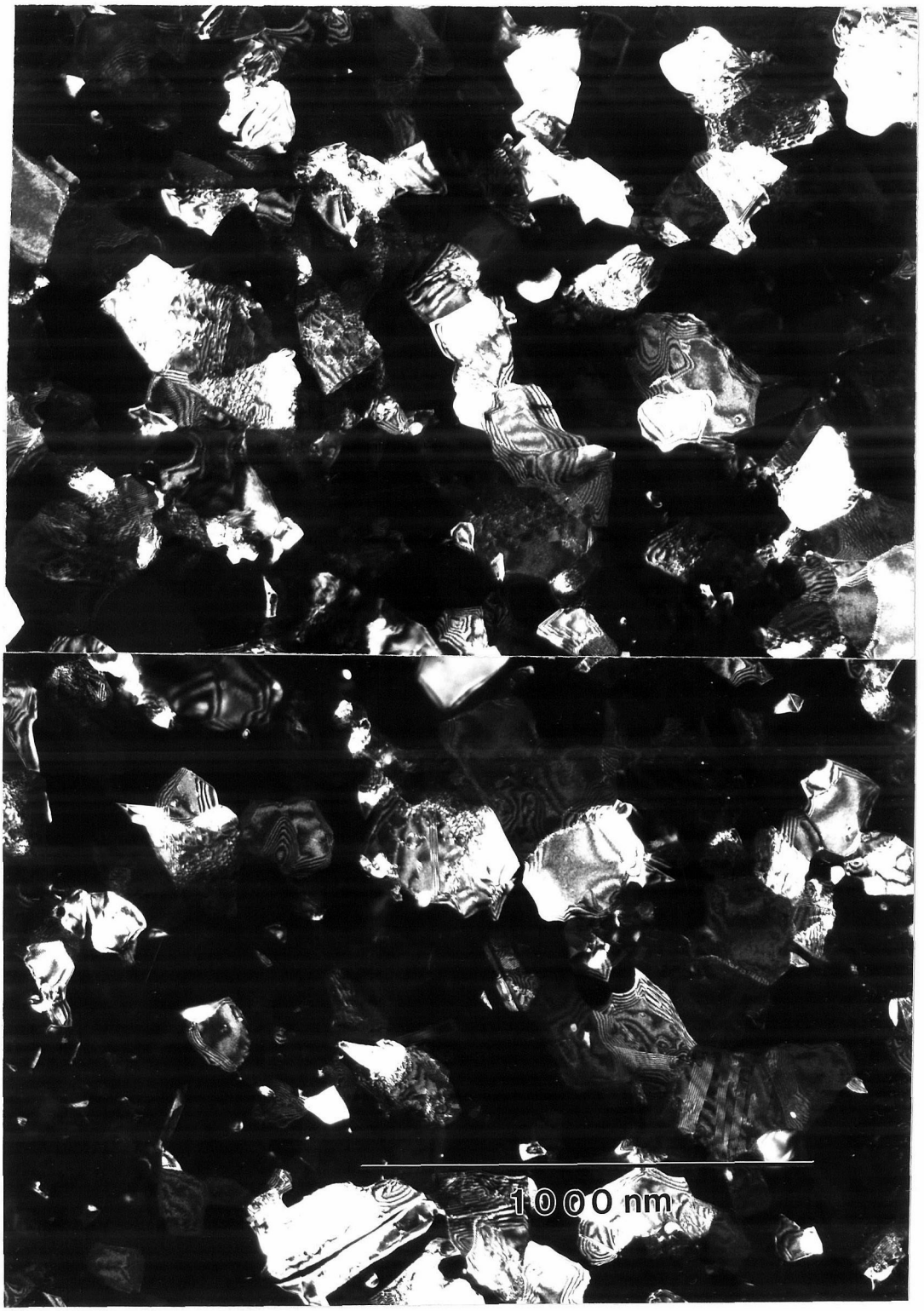

Figure 4.19 Microstructure (dark field images) in the plane perpendicular to the axis of rolling for annealed SS8 ingot deformed parallel to the direction of rolling at 550°C and nominal strain rate of 4.0×10^{-5} sec^{-1}. Microstructure consists of a mixture of (a) elongated grains and (b) 200 nm equiaxed grains.

It was determined by XRD that sample SS8 consisted entirely of bcc phase and sample SS8 annealed at 1050°C for 0.5 hrs consisted entirely of fcc phase. Since only the bcc phase of 304 stainless steel is ferromagnetic, the mass fraction of bcc phase in various samples was obtained by assuming that induced voltage (which is directly proportional to the magnetic moment of the sample) varies linearly with the mass fraction of bcc phase. These mass fractions are also listed in Table 4.1 and 4.2.

Sample Designation	Induced Voltage (mV/gm)	Mass Fraction of the Bcc Phase
SS8	66.63	100%
SS8A1050°C/0.5h	0.00	0%
SS8A575°C/2h	42.88	64%
SS8A575°C/2h deformed at 550°C and nominal strain rate of 4.65×10^{-5} sec^{-1}	44.10	66%
SS8A575°C/2h deformed at 550°C and nominal strain rate of 4.65×10^{-4} sec^{-1}	41.32	62%

Table 4.1 Induced voltages (directly proportional to the magnetic moments) and mass fractions of bcc phase, as measured by vibrating sample magnetometer for samples at various stages of processing. Note that the rolling axis of samples was kept perpendicular to the direction of vibration for these measurements.

It is clear from Table 4.1 and 4.2 that mass fractions of bcc phase as determined by the comparison of magnetic moments in the present investigation are dependent on the orientation of sample (with respect to the applied magnetic field). This is not surprising, because SS8 (which is 100% bcc) and SS8A575°C/2h ingots are highly textured (Figures 4.3,4.5,4.6), while other samples contain a varying degree of texture. It is well known

Sample Designation	Induced Voltage (mV/gm)	Mass Fraction of the Bcc Phase
SS8	56.26	100%
SS8A1050°C/0.5h	0.00	0%
SS8A575°C/2h	41.52	74%
SS8A575°C/2h deformed at 550°C and nominal strain rate of 4.65×10^{-5} sec^{-1}	47.93	84%
SS8A575°C/2h deformed at 550°C and nominal strain rate of 4.65×10^{-4} sec^{-1}	47.05	85%

Table 4.2 Induced voltages (directly proportional to the magnetic moments) and mass fractions of bcc phase, as measured by vibrating sample magnetometer for samples at various stages of processing. Note that the rolling axis of samples was kept parallel to the direction of vibration for these measurements.

that crystallographic texture can significantly alter the magnetic properties of materials, because certain crystallographic orientations of magnetic materials are more easily magnetized than others. Since the samples at various stages of processsing contain varying degrees of texture, the mass fractions of the bcc phase determined using this method may not be accurate. Nevertheless, these measurements provide an upper bound on the degree of phase transformation during the deformation processing. The data from Table 4.1 and 4.2 suggests that the amount of phase transformation (fcc $\Leftrightarrow$ bcc) during the LSR processing at 550°C and nominal strain rates of 4.65×10^{-5} sec^{-1} or 4.65×10^{-4} sec^{-1} is no more than $\approx$11%.

4.2.5 High Temperature Mechanical Testing on 370 nm Grain Size 304SS

For the purpose of comparison, compression tests were also performed on samples with average grain size bigger than 200 nm. These samples were produced in the following manner: A 0.375" diameter stainless steel rod was first rolled 75% at -197°C into an ingot with square cross section. This ingot was further rolled at room temperature to reduce the cross section to 0.135" × 0.135". Several compression test samples with an aspect ratio of ≈1.1 were cut from this ingot. These samples were then deformed at 560°C and nominal strain rate of 8.6×10^{-5} sec^{-1}. This processing resulted in a microstructure that was a mixture of ≈200 nm equiaxed grains and columnar grains. This ingot was annealed at 650°C for 2 hrs to obtain uniform equiaxed grain microstructure with average grain sizes of ≈370 nm. Coarser microstructures were obtained by annealing these samples at higher temperatures.

The 304 stainless steel samples with grain size of 370 nm were also deformed at 550°C and crosshead speed ranging from 0.0001"/min to 0.0004"/min. These crosshead speeds correspond to strain rates ranging from 1.75×10^{-5} to 1.2×10^{-4} sec^{-1}. In contrast to the annealed SS8 ingot, the stress-strain curve of 370 nm 304 stainless steel at 500°C and similar strain rates exhibits an elastic-perfectly plastic behavior. A typical stress-strain curve for deformation of 370 nm 304 stainless steel at 550°C and nominal strain rate of 3.5×10^{-5} sec^{-1} is shown in Figure 4.20. The flow stress (at 20% strain) data from these experiments is also plotted in Figure 4.16. Fitting a straight line through this data gives a stress exponent of n = 14.58. However, the scatter in this data is considerably higher as compared to data from the annealed SS8 sample.

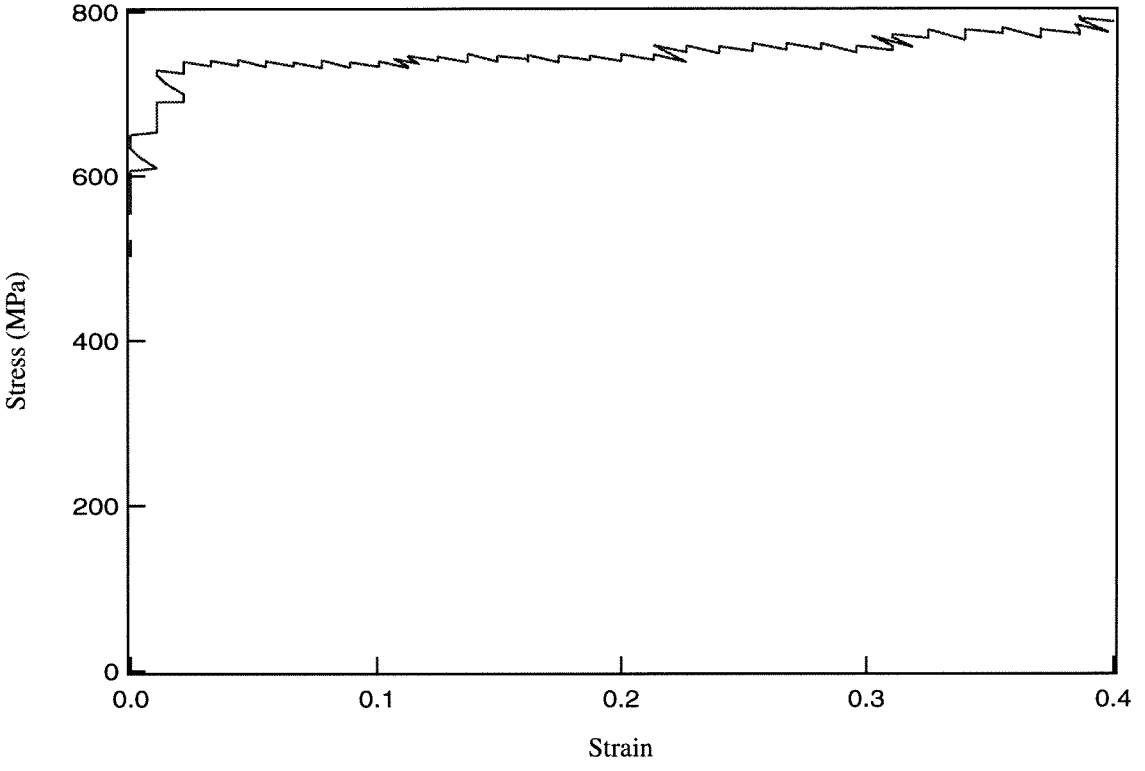

Figure 4.20 Stress-strain curve for the deformation of 370 nm grain size 304 stainless steel at 550°C and nominal strain rate of 3.5×10^{-5} sec^{-1}

4.3 DISCUSSION

It is clear from the dark field images in Figures 4.8-4.9 and 4.12-4.13, and selected area diffraction patterns in Figure 4.18 that microstructures with average grain size as fine as 200 nm can be formed in bulk 304 stainless steel by a processing route that does not require powder precursors. The uniformity of the diffraction rings in the SAD pattern (aperture diameter approximately 0.75 μm) suggests that the misorientation among the grains is large and that the grain boundaries are medium to high angle grain boundaries. The starting material for this processing technique is 304 stainless steel with a grain size of 200 μm and this processing technique requires a total strain of only 94%. The remainder of discussion section deals with the mechanisms that are responsible for the

refinement of microstructure. The processing of sub-micron-grain 304 stainless steel can be divided into two parts: (i) formation of sub micron columnar grains with equiaxed cellular structure, and (ii) break up of columnar grains and conversion of dislocation cells into grains with medium to high angle grain boundaries.

4.3.1 Formation of Cellular Structure

The first step in the processing of ultrafine grain 304SS involves deformation of an 304SS ingot in as-received condition (average grain size $\approx$ 200 μm) at room and liquid N_2 temperature. The microstructure after this deformation treatment consists entirely of bcc phase with a lath like morphology, while the microstructure before the deformation consisted of a mixture of bcc and fcc phases. Hence it is clear that a phase transformation took place in at least a part of the microstructure during the low temperature deformation. Since, all the deformation was carried out at 24°C (room temperature) and lower temperatures, and because the melting point for 304SS is $\approx$1400°C, the phase transformation takes place at the homologous temperatures of less than 0.175 T_m. Since it is highly unlikely that any diffusive phase transformation would take place at such low homologous temperatures, it is concluded that the phase transformation from fcc to bcc phase is martensitic in nature. This is not surprising as 304 stainless steel is known to undergo deformation induced martensitic phase transformations [17]. The lath morphology of the bcc phase formed after low temperature rolling is also quite typical of martensitic phase transformations. The deformation at liquid N_2 temperature during processing is critical for the generation of microstructure that is fully bcc as rolling at room temperature did not result in complete transformation of fcc phase into bcc phase.

Following the formation of the martensitic phase, the ingot was annealed at 575°C for 2 hrs. The BF images of the microstructure in the planes parallel and perpendicular to the axis of rolling after this annealing treatment gives an impression that the microstructure

consists of equiaxed grains ≈200 nm in size. However, it is obvious from the DF images, especially in the plane parallel to the axis of rolling, that the microstructure after the annealing treatment consists mostly of long columnar grains (with sub grains inside) aligned parallel to the axis of rolling. These columnar grains were ≈200 nm in diameter and about 1000-2000 nm long and contain equiaxed sub grains approximately 200 nm in size. A very small fraction of the microstructure also consisted of equiaxed grains ≈200 nm in size.

Clearly the ultrafine morphology of bcc phase formed by deformation at liquid N_2 temperature was critical towards formation of ultrafine cellular structure as the smallest dimension of the BCC laths (thickness) was smaller than cellular structure formed after annealing at 575^{o}C.

4.3.2 Conversion of Cell Boundaries into Grain Boundaries

The cellular structure of annealed SS8 ingot changes substantially after the low strain rate deformation (opposite to the direction of rolling deformation) at 550^{o}C. The transformed microstructure consists primarily of equiaxed ultrafine grains (grain size ≈ 200 nm). The salient features of this microstructure after LSR deformation are as follows:

1. The grain size and shapes are quite similar in both directions, i.e., in planes parallel and perpendicular to the axis of LSR deformation. This suggests that the grains are equiaxed and not pancaked.

2. The diffraction rings (Figures 4.18b, 4.18c) after deformation at 550°C and nominal strain rate of 4.65×10^{-5} sec^{-1} and 4.65×10^{-4} sec^{-1} are more uniform than those (Figure 4.18a) before deformation. Comparison of SAD patterns from the same aperture before and after LSR deformation indicates that misorientation among neighboring cells/grains has increased during the LSR deformation at 550°C.

3. The grain size after LSR deformation at both strain rates, i.e., 4.65 $\times$ 10^{-5} sec^{-1} and 4.65 $\times$ 10^{-4} sec^{-1} is approximately the same (200 nm). Note that the lower strain rate deformation took $\approx$7 hrs. to complete, while the higher strain rate test took approximately 90 minutes.

4. The grain size after the LSR deformation is very close to the cell size before the LSR deformation.

5. The microstructure after LSR deformation is quite typical of a well annealed microstructure, i.e., equiaxed grains with sharp grain boundaries and low dislocation density.

6. The final microstructure after LSR deformation is a mixture of the bcc and the fcc phases.

7. Formation of ultrafine grain microstructure is dependent on the strain rate at which LSR deformation is carried out. Microstructure of the sample that was deformed at nominal strain rate of 4.4 $\times$ 10^{-3} sec^{-1} consisted mostly of partially broken columnar grains. In contrast, the microstructure of the samples that were deformed at strain rates lower than 4.4 $\times$ 10^{-4} sec^{-1} consisted primarily of equiaxed grains approximately 200 nm in size.

The precipitous drop in flow stress of annealed SS8 ingot (at nominal strain rate of 4.4 $\times$ 10^{-5} sec^{-1}) with temperature, starting at 500^{o}C (Figure 4.7) suggests a change in deformation mechanism at this temperature. However, this data alone does not clarify whether the change in deformation mechanism is caused by change in microstructure or is a result of changed microstructure. Since, most metallic materials deform by the dislocation glide (deformation mechanism) at room temperature, it is not unreasonable to assume that dislocation glide is the primary deformation mechanism in annealed SS8 sample at room temperature. This is further corroborated by the fact that flow stress

at room temperature is virtually insensitive to strain rate. Hence it appears that the deformation mechanism in annealed SS8 ingot changes from dislocation glide to some creep mechanism at about 500°C and nominal strain rate of 4.4×10^{-5} sec^{-1}.

Since LSR deformation was carried out at relatively high temperature (550^{o}C), there are two variables, i.e., (i) annealing at higher temperature, and (ii) deformation, that are possibly affecting the development of microstructure. A possibility therefore exists that independent action either variable is causing the break up columnar grains.

4.3.3 Critical Evaluation of Mechanisms for the Break up of Columnar Grains

(i) *Refinement of microstructure due to phase transformation during LSR processing*: Jin, Morris and Zackay [18] and Syn, Jin and Morris [19] have shown in Fe-12Ni-0.25Ti and Fe-9Ni-0.1C-0.9Mn steels respectively that the microstructure can be refined by alternate phase transformations in the γ and $(\alpha + \gamma)$ range. This processing involves heating of these steels to temperatures above the A_s temperature, followed by cooling below the M_f temperature. This cycle is repeated several times to obtain the desired microstructure. The heating above A_s temperature results in complete or partial austenization of steel depending on the final temperature, and cooling below M_f temperature results in complete transformation of austenite into martensite. This thermal cycling results in succesive refinement of the microstructure. The refinement of the microstructure by this processing technique is attributed to the facts that martensite formed on cooling is finer than the parent austenite and that the martensite grains that forms in the successive cycles have a different orientations than those of the previous cycles. As a result preferential orientation of the grains is largely eliminated during the successive cycles. Microstructures with grain sizes as fine as 2μm were obtained by this technique.

As discussed previously, it is clear that the formation of an ultrafine lath structure (laths approximately 100 nm in width) is a result of martensitic phase transformation during liq-

uid N_2 temperature rolling of 304 stainless steel. Some of this martensite phase transforms into fcc during annealing at 575°C for 2hrs. The microstructure after this processing has a columnar morphology and is still heavily textured. However, these columnar grains break up during the LSR processing at 550°C. Magnetic measurements (Table 4.1 and 4.2) reveal that the amount of material that undergoes any phase transformation during LSR processing at 550°C at nomimal strain rate of 4.64×10^{-5} sec^{-1} or 4.64×10^{-4} sec^{-1} is less than 11% in both cases. It is highly unlikely that a phase transformation in only 11% of microstructure can change the morphology of the entire microstructure. Hence, it appears that the mechanism for the refinemnent of 304 stainless steel (observed in the present investigation) is different than that of Morris et al. [18,19].

(ii) *Static recrystallization*: If static recrystallization is the primary cause for the formation of 200 nm grain size microstructure, then annealing of SS8 sample for longer periods of time should yield the same equiaxed grain microstructure that resulted after LSR deformation. However, the microstructure (Figure 4.11) of SS8 sample annealed at 575^0C for 12 hrs (more than the time SS8 ingot spent in furnace during and prior to the LSR deformation) is very similar to the microstructure before the LSR deformation, i.e., columnar grains containing a cellular structure with the exception that the columnar grains are wider. This indicates that static recrystallization is not the primary cause for the formation of 200 nm grain size microstructure in 304 stainless steel.

(iii) *Breakage of columnar grains into grains of the size of cells during compressive deformation*: If the fine grain microstructure is formed by breaking apart of cells in the columnar grains during compressive deformation (along the axis parallel to columnar grains), then the temperature and strain rate at which LSR deformation is carried out should be irrelevant. However, it is evident from Figure 4.10 that the microstructure of the sample deformed at 450°C and nominal strain rate of 3.3×10^{-5} sec^{-1} consists primarily

of elongated grains aligned parallel to the axis of rolling. This microstructure is very similar to that of starting material for the LSR deformation. In addition, microstructure of the SS8 ingot deformed at 550°C and nominal strain rate of 4.4×10^{-3} sec^{-1} does not consist of equiaxed grains. This eliminates the possibility that compressive deformation alone (along the axis parallel to elongated grains) is the primary cause for the break up columnar grains into smaller equiaxed grains.

The observations indicate that both variables, i.e., annealing at 550°C and LSR compressive deformation opposite to direction of rolling, are necessary for the break up of columnar grains into equiaxed grains. Hence, mechanisms that take into account both variables should be considered.

(iv) *Dynamic recrystallization*: Accumulation of defects (dislocations) is a necessary step for recrystallization [20]. Therefore, relatively dislocation free microstructure after LSR deformation suggests that recrystallization took place in the entire sample towards the end of the mechanical test. This is unlikely, because recrystallization is a known to be a thermally activated process. Therefore, if continuous "dynamic recrystallization" is the cause for grain refinement, then microstructure after the LSR deformation should contain a mixture of microstructures at various stages of recrystallization, i.e., some parts of the microstructure should contain higher dislocation density, while the rest of the microstructure should comprise of relatively dislocation free equiaxed grains.

In another scenario, the formation of the small grains might have taken place during the early stages of deformation by dynamic recrystallization and the mode of deformation after formation of fine equiaxed grains is such (dislocation glide and creep or grain boundary sliding) that it did not result in accumulation of dislocations in the microstructure. Since recrystallization did not take place in the starting material for LSR deformation on annealing at higher temperatures for longer times, it appears that the defect density

was not high enough for recrystallization to take place at 550^{o}C in the starting material for LSR deformation. Therefore, if dynamic recrystallization is the predominant cause for the formation equiaxed grains then these defects must have been introduced during the LSR deformation. In general, the deformation at lower temperature results in higher density of line defects in the microstructure (at comparable strain rates). Hence the driving force for recrystallization would be higher (or at least the same) in a sample that is deformed at lower temperatures. This means that the driving force for recrystallization in the annealed SS8 ingot deformed to 40% engineering strain at room temperature would at least be the same or higher compared to the driving force for recrystallization during (or after) LSR deformation at 550^{o}C at the same strain rates. Note that annealed SS8 sample was deformed 40% during LSR deformation. Hence annealing of this sample for the same amount of time as the duration of testing time for LSR deformation test at 550^{o}C should have resulted in a microstructure very similar to that obtained by LSR processing. However, the microstructure after deformation consisted primarily of elongated grains with high dislocation density (Figure 4.17). This suggests that dynamic recrystallization is not the predominant mechanism for the formation of the observed microstructure.

(v) *Grain boundary sliding*: Since the grain size of the microstructure after LSR deformation at 550^{o}C is very close to the cell size before LSR deformation, it appears that dislocation cells somehow transformed into grains with high angle boundaries during LSR deformation at 550^{o}C. Furthermore, the microstructure after LSR deformation consists primarily of equiaxed grain microstructure with low dislocation density. These observations strongly suggest that the deformation at low strain rate and high temperature took place by some mechanism of grain boundary sliding similar to the one put forth by Ashby and Verrall in 1973 [21]. A 2-D schematic of this model is shown in figure 4.21. Gifkins [22] and Langdon [23,24] have further developed Ashby's model by fixing

some of its shortcomings and extending it to three dimensions. It is clear from figure 4.21 that this mode of deformation would result in increased misorientation among the dislocation cells as the cells slide with respect to each other and interchange neighbors. The salient features of this model of creep deformation are that (i) minimal changes in the shape of grains take place during the deformation, (ii) change in grain shape does not reflect macroscopic deformation, and (iii) grains change neighbors during deformation. This mode of deformation is most generally observed to operate when the grain boundaries are high angle grain boundaries, however there are a few instances where it is observed in microstructures consisting of cells with low angle boundaries (e.g., Tsuzaki et al. [25]). This explanation is consistent with all the microstructural observations of present investigation, i.e., equiaxed grains and low dislocation density. Furthermore, this model also explains the break up of columnar grains and conversion dislocation cells into grains with medium to high angle grain boundaries. There are a few examples in literature where this mechanism is believed to operate in materials with sharp dislocation cell boundaries. It was observed by Tsuzaki et al. [25] that the misorientation among dislocation cells (2-5 μm) increased progressively during the low strain rate deformation of 25Cr-7Ni-3Mo ferrite/austenite duplex stainless steel at 1000^{o}C and eventually resulted in conversion of dislocation cells into grains with high angle boundaries.

The stress-strain curve observed by Tsuzaki et al. [25] during this transition of microstructure is very similar to that observed in our experiments (Figure 4.15), i.e., the stress rises initially with plastic deformation and then drops slowly and eventually plateaus out with the exception that the ratio of peak to plateau stress is much higher in our investigation. It is quite possible that this peak to plateau stress ratio is related to the details of initial cellular structure.

It appears that grain boundary sliding (GBS) is difficult initially due to low misorientation

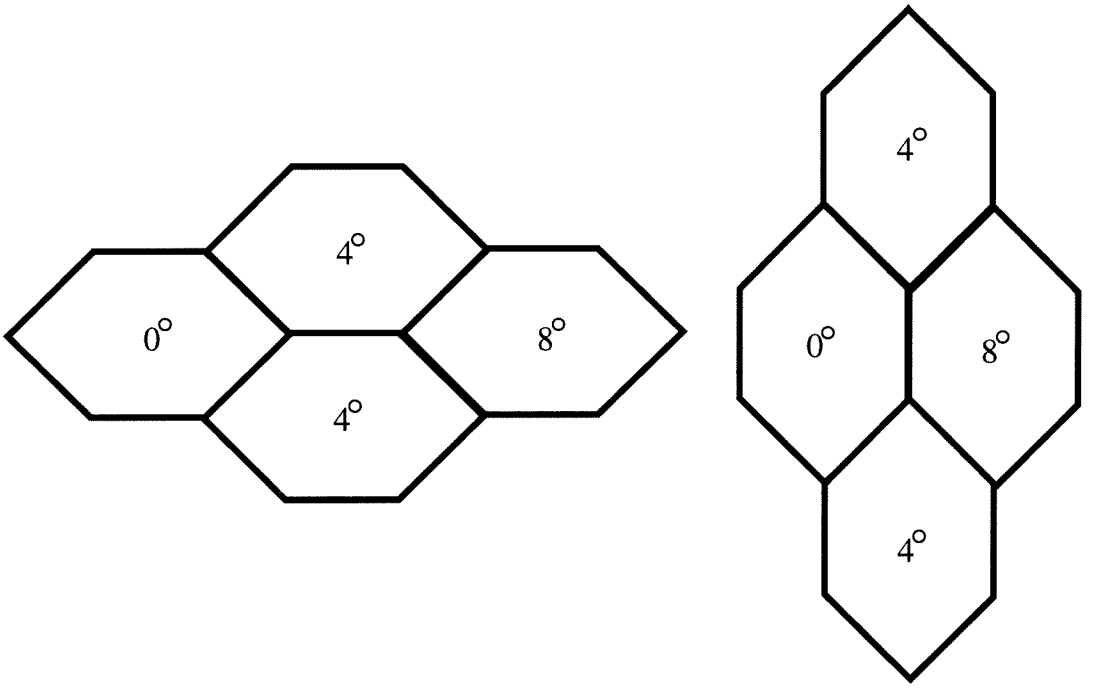

Figure 4.21 A schematic of grain boundary sliding model of Ashby and Verrall. The strain of 55% required to move from state (a) to state (b). Notice that grain change neighbors from state (a) to state (b).

among the dislocation cells. However, as the GBS progresses, the misorientation among the cells increases and GBS becomes easier. Consequently, the flow stress in initially higher, but decreases as the misorientation among the dislocation cells increases. This is consistent with the observations of Weinberg [26]. Weinberg [26] has observed that the grain boundary sliding in aluminum tricrystals does not take place below a certain misorientation ($\approx 5°$), and the rate of grain boundary sliding increases with increasing misorientation up to about 17° for constant shear stress. This was attributed to strong bonding among atoms at small angle boundaries, because these boundaries can be described with dislocation arrays. In the current study misorientation among the dislocation cells could not be quantified due to the very small size of the cells. However, because of the very fine nature of the microstructure, the stress required for plastic flow (by dis-

location glide) would be much higher compared to that in a tricrystal. Therefore grain boundary sliding may start at much lower misorientations.

If grain boundary sliding is the primary cause for the break up of columnar grains then the direction in which LSR deformation is carried out should not affect the grain refinement process. However, while the LSR deformation opposite to direction of rolling resulted in complete break up of columnar grains, LSR deformation in the direction of rolling resulted in a partial break up of columnar grains and formation of an ultrafine equiaxed grain microstructure in only a fraction of the sample. Since all the other microstructural evidence suggests that grain boundary sliding is the primary cause for the break up columnar grains, it appears that the anisotropic behavior during processing is a result of differences in the nature of boundaries (cell and/or columnar grain) in two directions. It is clear from Figures 4.5 and 4.6 that columnar grains are aligned parallel to the rolling axis and hence boundaries parallel to the axis of rolling are mostly higher angle grain boundaries (columnar grains) as compared to the boundaries perpendicular to the direction of rolling, which are low angle cell boundaries. Since the stress required for grain boundary sliding decreases with increasing misorientation, grain boundary sliding can initiate much easily when high angle grain boundaries are aligned parallel to the axis of LSR deformation. Consequently, the break up of columnar grains is expected to be easier when they are aligned parallel to the axis of LSR deformation.

4.3.4 Mode of Deformation after the Break up of Columnar Grains

The stress-strain curves (Figure 4.15) for the deformation of the annealed SS8 ingot at 550°C and strain rates below 5.8×10^{-4} sec^{-1} indicate that the flow stress declines initially during the deformation and a plateau in flow stress is reached at a true strain of about 0.3. This suggests that a steady state has been reached at this strain and that the break up of columnar grains is essentially complete and misorientations among grains

have exceeded the point where stress required for deformation (by grain boundary sliding) is dependent on misorientation among grains. Hence it is postulated that the plateau stress (flow stress at strain of 0.3 and beyond) is representative of the operating deformation mechanism in the fine grain steel.

Since the break up of columnar grains into smaller equiaxed grains was attributed to grain boundary sliding, it is reasonable to assume that the mode of deformation after the break up of columnar grains (i.e., in the later stages of mechanical test) is also grain boundary sliding, because the conditions (i.e., temperature and strain rate) under which deformation is taking place do not change substantially during the test. However, stress exponents for deformation governed by grain boundary sliding fall in range of 1 to 2 (for most materials). Stress exponents as high as 3 were observed in some ceramics recently for deformation by grain boundary sliding [27]. Most theories of grain boundary sliding also predict stress exponents ranging from 1 to 2 [11-15,21]. Hence, the very large stress exponent (n = 5.76) observed for LSR deformation of annealed SS8 ingot at 550°C in the strain rate range of 1.4×10^{-5} to 5.8×10^{-4} sec^{-1} cannot be explained by any existing mechanism of grain boundary sliding.

High stress exponents, such as in the range of 3 to 7, are generally associated with dislocation creep [28]. As discussed in the last section, the break up of columnar grains in the present circumstances can not be easily explained by known dislocation mechanisms, because recrystallization was eliminated as a mechanism for the formation of 200 nm equiaxed grain microstructure. This suggests the possibility that the break up of columnar grains takes place during the early stages of deformation, and that the mode of deformation changes from grain boundary sliding to dislocation creep following the break up of columnar grains. If this is the case, then cause for the transition in deformation mechanism is not clear, because the conditions of deformation do not change significantly during the

mechanical test. In addition, any deformation that takes place by dislocation glide or creep usually results in (a) change in shape of grains that reflect macroscopic shape change, and (b) a significant increase in dislocation density in the microstructure. In contrast, the microstructural observations of the present investigation indicate the presence of equiaxed grains with relatively low dislocation density after deformation. Several arguments can be made to explain these apparent contradictions: For example, it has been suggested that the higher curvature of pancaked (elongated) grains provides an additional driving force for grain growth and results in conversion of pancaked (elongated) grains into equiaxed grains. This scenario has been used to explain the observation of equiaxed grain microstructures in several materials where elongated grains are expected after deformation. The occurrence of grain growth would also explain the low dislocation density in the microstructure as it would suggest that there is enough thermal activation for dislocations to move to the grain boundaries. However, significant grain growth is not expected at 550°C, because the grain size after LSR deformation at the crosshead speed of 0.0002"/min is approximately the same as that after LSR deformation at the crosshead speed of 0.002"/min. It should be noted that the sample spends approximately 6.5 hrs at 550°C for deformation at the crosshead speed of 0.0002"/min compared to 0.5 hrs at the crosshead speed of 0.002"/min.

Lange and Raj [29] have proposed a model that can explain retention of an equiaxed microstructure without grain growth during dislocation creep. They have suggested that pancaking (or elongation) of grains during deformation governed by dislocation mechanisms results in the distortion of equilibrium angle between the grain boundaries at the triple points. The distortion of the angle between grain boundaries away from the equilibrium position provides a driving force for movement of grain boundaries in the manner that results in conversion of pancaked grains into equiaxed grains. They have

also pointed out that pancaking (or elongation) of grains also results in changes in grain curvature that aids this process, i.e., retention of equiaxed microstructure. Although the presence of an equiaxed microstructure during deformation by dislocation creep can be explained by Lange and Raj's mechanism, it is unclear how dislocation creep can operate without dislocations. Hence, it appears that traditional mechanisms of dislocation creep or grain boundary sliding can not effectively explain the deformation behavior of 200 nm grain size 304 stainless steel.

In addition, the stress exponent of n = 14.58, for the deformation of 370 nm 304 stainless steel at 550°C and strain rates ranging from 1.75×10^{-5} to 1.2×10^{-4} sec^{-1} is much higher than that for 200 nm 304 stainless steel under similar conditions. Such a high stress exponent is too high for dislocation creep and too low for dislocation glide. Furthermore, the flow stress at the lower end of strain rates (in which testing was performed) is higher than that for 200 nm 304 stainless steel at comparable strain rates. However, we realize that mechanical data for 370 nm grain size 304 stainless steel is available only in a limited range of strain rates and there is considerable scatter in this data. Hence any conclusions drawn from this data should be treated with caution.

This leaves two possibilities, (i) that deformation after break up of columnar grains is taking place by some other (not commonly known or modeled) mechanism of dislocation creep that does not result in accumulation of dislocations in the microstructure, while the equiaxed nature grains is maintained due to the operation of Lange and Raj's mechanism. One such mechanism can be easily proposed, if it is assumed that dislocations inside the grains are relatively unstable due to the combined effect of high mobility and shorter distances to the grain boundaries. This can be thought of as a direct consequence of the small grain size and relatively high temperature of deformation. This means that dislocations, if not strongly pinned are quickly absorbed by the grain boundaries. This

model also assumes that dislocations needed for deformation are generated from the grain boundaries. Once the dislocations are generated at grain boundaries, they travel relatively uninhibited to other grain boundaries. Hence the deformation is accomplished by glide or climb of dislocations, while generation of dislocations from grain boundaries is the rate determining process. According to this mechanism the grains would remain relatively dislocation free at lower strain rates. In contrast, deformation at higher strain rates would require creation of greater number of dislocations in the microstructure. If the strain rates are too high then more dislocations would have to be generated from the grain boundaries and chances for dislocation pinning and hence becoming immobile would increase. As a result the dislocation density in the microstructure would progressively increase. (ii) The other possibility is that the mode of deformation in 304 stainless steel at 550°C is grain boundary sliding with an unusually high stress exponent of 5.76. The microstructural evidence of this investigation is fully consistent with the mechanism of grain boundary sliding. However, there is no model of grain boundary sliding that predicts such high stress exponent. This would probably be the first instance where such high stress exponent is observed for grain boundary sliding. Stress exponents as high as 3 are observed in several ceramic materials for deformation by grain boundary sliding, while there are no existing models of grain boundary sliding that predict stress exponent of 3.

4.4 CONCLUSIONS

1. An ultrafine grain microstructure (grain size $\approx$ 200 nm) can be formed in bulk 304 stainless by a deformation processing technique that does not require powder precursors. In addition this processing requires only 95% (e = 3) total strain and is amenable to scale up. This is in to large strains (e = 7) required by other processing techniques.

2. The first step of the two step processing technique requires deformation at room

and liquid N_2 temperature followed by annealing at 575^{o}C and the final step involves deformation at low strain rates and high temperatures.

3. The deformation at room and liquid N_2 temperature results in complete transformation fcc phase into bcc phase martensitically. The microstructure after this deformation consists entirely of bcc phase with a ultrafine lath morphology ($\approx$ 100 nm thick and 500 to 1000 nm in other two dimensions). This microstructure on annealing at 575^{o}C for 2 hrs transforms to a mixture of bcc and fcc phases with columnar grain morphology. The columnar grains were aligned parallel to the direction of rolling and contain a dislocation cell structure (equiaxed). The dislocation cells were of the same size as the width of columnar grains.

4. The conditions of the second step of processing were chosen to initiate grain boundary sliding during deformation. The deformation by grain boundary sliding causes the misorientation among the dislocation cells to increase and results in formation equiaxed grain microstructure.

5. The mechanism of deformation after the break up of columnar grains at 550°C and strain rates ranging from 1.4×10^{-5} sec^{-1} to 5.8×10^{-4} sec^{-1} are not entirely clear. The microstructural evidence indicates that mode of deformation is grain boundary sliding, but the related stress exponent (n = 5.76) is too high to be explained by any existing model of grain boundary sliding.

6. The mechanical behavior of 200 nm grain size 304 stainless steel at 550°C and strain rates lower than 5.8×10^{-4} sec^{-1} cannot be explained by any existing models of dislocation creep.

REFERENCES

[1] R. Z. Valiev, N. A. Krasilnikov and N. K. Tsenev, Mater. Sci. engng A137, 35 (1991).

[2] N. A. Smirnova, V. I. Levit, V. I. Pilyugin, R. I. Kuznetsov, L. S. Davydova and V. A. Sazonova, Fizika Metall. 61, 1170 (1986).

[3] R. Z. Abdulov, R. Z. Valiev and N. A. Krasilnikov, J. Mater. Sci. Lett. 9, 1445 (1990).

[4] R. Z. Valiev, E. V. Kozlov, Y. F. Ivanov, J. Lian, A. A. Nazarov and B. Baudelet, Acta Met., 42, 2467 (1994).

[5] S. Erbel, Met. Technol. 6, 482 (1979).

[6] I. Saunders and J. Nutting, Metal Sc. 18, 571 (1984).

[7] O. D. Sherby, C. M. Young, B. Walser and E. M. Cady, Jr.,"Superplastic Ultrahigh Carbon Steel", U.S. patent 3,951,697, (April 20, 1976).

[8] O. D. Sherby and T. Oyama,"Ultrahigh Carbon Steel Alloy & Processing Thereof", U.S. patent # 4,533,390 (August 6, 1985).

[9] O. D. Sherby, D. W. Kum, T. Oyama and J. Wadsworth,"Ultrahigh Carbon Steels Containing Aluminum", U.S. patent # 4,769,214 (September 6, 1988).

[10] D. M. Moore and L. R. Morris, Mat. Sc. Engng., 43, 85 (1992).

[11] J. W. Edington, K. N. Melton and C. P. Cutler, Prog. Mat. Sc. 21, 61 (1976).

[12] R. C. Gifkins, Met. Trans. 7A, 1225 (1976).

[13] R. Raj and M. F. Ashby, Met. Trans. 2, 1113 (1971).

[14] A. K. Mukherjee, Mat. Sc. Engng. 8, 83 (1971).

[15] T. G. Langdon, Phil. Mag. (1970)

[16] S. Foner, Rev. Sci. Instr. 30, 548 (1959).

[17] R. P. Reed, in Austenitic Steels at Low Temperatures (edited by R. P. Reed and

T. Horiuchi), p. 41, Plenum Press, New York (1983).

[18] S. Jin, J. W. Morris, Jr. and V. F. Zackay, Met. Trans 6A, 141 (1975).

[19] C. K. Syn, S. Jin and J. W. Morris, Jr., Met. Trans 7A, 1827 (1976).

[20] H. J. Mcqueen and J. J. Jonas, in Treatise on Materials Science and Technology (edited by R. J. Arsenault), p. 393, vol. 6, Academic Press, New York (1975).

[21] M. F. Ashby and R. A. Verrall, Acta metall. 21, 149 (1973).

[22] R. C. Gifkins, J. Mater. Sci., 13, 1926 (1978).

[23] T. G. Langdon, Metals Forum 4, 14 (1981).

[24] Idem, Mater. Sci. Eng. A 137, 1 (1991).

[25] K. Tsuzaki, H. Matsuyama, M. Nagao and T. Maki, Mat. Trans. JIM 31, 983 (1990).

[26] F. Weinberg, Trans. TMS-AIME 212, 808 (1958).

[27] D. M. Owen and A. H. Chokshi, to be published in J. Mat. Sc.

[28] J. P. Poirier, Creep of Crystals (Cambridge Earth Science Series), p. 94-144, Cambridge University Press, Cambridge (1985).

[29] R. Raj and F. F. Lange, Acta Metall. 33, 699 (1985).

CHAPTER V

Mechanical Behavior in Bulk Ultrafine Grain Steel

5.1 INTRODUCTION

It is well known that yield strength of materials increases with decreasing grain size. Empirically, the yield strength of materials exhibits following relationship with grain size,

$$\sigma_y = \sigma_o + kd^{-n}, \quad (1)$$

where σ_y is yield stress, σ_o is frictional stress, k is positive material constant (hardening coefficient), d is the grain size, and n represents the grain size hardening exponent. Hall-Petch dislocation pileup mechanism [1-4] is most commonly used to describe grain boundary strengthing in materials. This model predicts a grain size exponent of $\frac{1}{2}$. It is for this reason that most of the grain size hardening data is plotted against inverse square root of grain size. However, the validity of this mechanism has not been conclusively verified. Baldwin [5] has pointed out that general scatter normally observed with the mechanical strength and grain size data, in many cases, gives equally good linear fit between σ_y and $d^{-\frac{1}{3}}$, $d^{-\frac{1}{3}}$, $d^{-\frac{1}{2}}$ or d^{-1}. Several existing models predict grain size hardening exponents of $\frac{1}{4}$, $\frac{1}{3}$, $\frac{1}{2}$ and 1. Furthermore, there is considerable debate about the applicability of Hall-Petch relationship to ultrafine microstructures. Several authors have reported significant deviations from Hall-Petch relationship in materials with grain sizes finer than 1 μm [6-10].

Chokshi et al. [8], Chang et al. [9], and Lu et al. [10] have observed negative hardening

coefficient for the HPR in nanophase materials at room temperature. These authors and others have attributed this behavior to deformation mechanisms that are diffusive in nature (e.g., Coble and Nabbaro Herring creep or grain boundary sliding). Although, diffusive mechanisms of deformation predict this trend i.e., decreased strength with decreasing grain size, they do not predict HPR with negative hardening coefficient. In addition, the data of Nieman, Weertman and Siegel [11], Hughes et al. [12], Jang and Koch [13], and Ganapathi and Rigney [14] for nanocrystalline materials follow normal HPR with the exception that the hardening coefficient is lower than that for coarse grain counterparts. Some authors have attributed this to breaking down of assumptions made in the derivation of Hall-Petch mechanism with decreasing grain size (especially below 1μm) [15-17]. Others have proposed that the decrease in hardening coefficient is a result of a change in grain boundary structure [18] or simultaneous operation of other softening mechanism [6]. Valiev et al. [6] have observed a change (decrease) in the hardening coefficient at about 500 nm in a fully dense Mg-1.5Mn-0.3Ce alloy for sub-micron grain materials. They have attributed this behavior to the accelerated absorption of lattice dislocations by the grain boundaries.

Fougere et al. [19] have observed both softening and hardening with decreasing grain size in nanophase materials depending on whether annealing was used to obtain coarser microstructures. Valiev et al. [7] and Fougere et al. [19] have also pointed out that microstructural factors other than grain size (such as structure of grain boundaries, grain shape, dislocation substructure in the grain interior, porosity etc.) may have significant effect on the mechanical behavior of ultrafine grain materials. These factors were not taken into account in most of these studies.

The goal of the research described in this chapter was to examine the mechanical behavior of 200 nm bulk 304 stainless steel and explore validity of Hall-Petch relationship over

a broad range of grain sizes (ranging from 200 nm to 200 μm) in 304 stainless steel with well-defined microstructures (i.e., grain shape, dislocation substructure etc.) and no residual porosity.

5.2 EXPERIMENTS

5.2.1 Processing of Fine Grain Microstructures

The 304 stainless steel samples with the grain size of 200 nm were produced by the processing technique described in Chapter 4. These samples were annealed at 600°C for 2 hrs to obtain an equiaxed grain microstructure with an average grain size of 280 nm.

The samples with grain sizes coarser than 280 nm were produced by a variation of technique described in the previous chapter. A 0.375" diameter stainless steel rod was first rolled 75% at -197°C into an ingot with square cross section. This ingot was further rolled at room temperature to reduce the cross section to 0.135" $\times$ 0.135". Several compression test samples with an aspect ration of $\approx$1.1 were cut out of this ingot. These samples were then deformed at 560°C and nominal strain rates of 8.6×10^{-5} sec^{-1}. This processing resulted in a microstructure that was a mixture of $\approx$200 nm equiaxed grains and columnar grains. This ingot was annealed at temperatures ranging from 650°C to 800°C to obtain uniform equiaxed grain microstructures with average grain sizes ranging from 370 nm to 2000 nm.

5.2.2 Microstructural Examination

The microstructures of the samples used for mechanical testing were examined by transmission electron microscopy (TEM). The samples for TEM examination were made by electro-jet-thinning. To prepare the TEM foils, several thin slices in the plane parallel to the axis of rolling were cut by a diamond saw. Several 3 mm discs were punched out of

these slices. These 3 mm discs were polished to 600 grit on both sides. The thickness of discs after polishing ranged from 50 to 80 μm. These polished discs were dimpled using 6 μm diamond paste until the thinnest region in the disc was about 20μm. The dimpled discs were then electro-jet-thinned at -35^{o}C in a 95% methanol + 5% perchloric acid solution at 35 volts and 64 milliamps. TEM examination was carried out on Philips EM301 microscope operating at 100kV.

The grain size in the microstructure was determined by the line intercept method. This method employs measurement of mean intercept length (N_L) of random test lines as a measure of grain size. The mean intercept length was calculated in the following manner: the number of intersections made by several random test lines with the grain boundaries were counted. The mean intercept length was obtained by dividing the total length of the test line by the number grain boundaries intersected. Smith and Guttman [20] have shown that grain boundary area per unit volume (S_V) can be calculated without making assumptions regarding the shape and size distribution of grains from the measurement of mean intercept length by the following equation,

$$\mathbf{S_V} = \mathbf{2N_L}. \tag{2}$$

If it is assumed that all the grains are spherical and that each grain boundary is shared by two grains then the average grain size is given by,

$$\mathbf{2S_V} = \frac{\mathbf{4\pi(D/2)^2}}{\mathbf{4\pi/3(D/2)^3}}$$

or

$$\mathbf{D} = \frac{\mathbf{3}}{\mathbf{S_V}} = \frac{\mathbf{3}}{\mathbf{2N_L}}. \tag{3}$$

5.2.3 Mechanical Testing

The load and displacement data during the test was collected by a personal computer linked to the load frame through an IEEE interface. The load data is the actual load on the sample. But the displacement data includes contribution from the sample and rest of the load train (compliance of the load frame and accessories). So the as-collected load displacement data needed to be corrected to obtain true load displacement curve for the sample. The load train was assumed to consist of two non linear springs connected to each other in series. The first spring corresponds to the sample while the other to the rest of the load train. Load displacement data for the second spring (i.e., load train minus the sample) was collected under the same conditions (i.e., same cross head speed, temperature etc.). Denote the load-displacement curve for spring 2 (load train minus the sample) by

$$d_2 = g_2(F)$$

and for spring 1 (sample) by

$$d_s = g_s(F)$$

and for the load train including the sample by

$$d = g(F)$$

where d represents the displacement and F represents load. Then the load displacement curve for the sample is given by

$$d_s = d - d_2 = g_2(F) - g(F) = g_s(F).$$

A computer program was written to perform these calculations and obtain the true load-displacement data for the sample.

Approximately cube shaped samples for compression testing at room temperature were cut out by diamond saw. Each side of the samples were polished to 600 grit paper before mechanical testing. The room temperature mechanical testing was carried out on a 10,000 lbs Instron 4204 load frame at the constant cross head speed of 0.02"/min, which corresponded to nominal strain rate of 4.0×10^{-3} sec^{-1}.

Several pieces of SS8 ingot were rolled on a rolling mill with flat rolls into a plate approximately 0.04" in thickness. Tensile test samples were electro-discharge-machined (EDM) from these plates. These samples were then annealed at 575°C for 2 hours. Following the annealing, these samples were polished on all sides to 600 grit emery paper. Tensile tests samples were pulled to failure at room temperature in specially designed grips to minimize bending and torsion.

5.3 RESULTS

A stress-strain curve in compression for 304 stainless steel with 215 nm equiaxed grained microstructure is shown in Figure 5.1. The 215 nm 304 stainless steel yielded at 1700 MPa and flowed virtually without any strain hardening thereafter. No cracks or any other signs of failure were observed in the sample up to the true strain of 0.7, when the test was stopped. The microstructure of 304 stainless steel with the average grain size of 215 nm is shown in Figure 5.2 and with the grain size of 370 nm is shown in Figure 5.3. These microstructures consist of equiaxed grains with very low dislocation density. The microstructure of other samples with coarser grain sizes were very similar to the microstructures in Figure 5.2 and 5.3, i.e., they consisted of equiaxed grains with low dislocation density.

The compressive yield stress of 304 stainless steel for various grain sizes (200 nm to

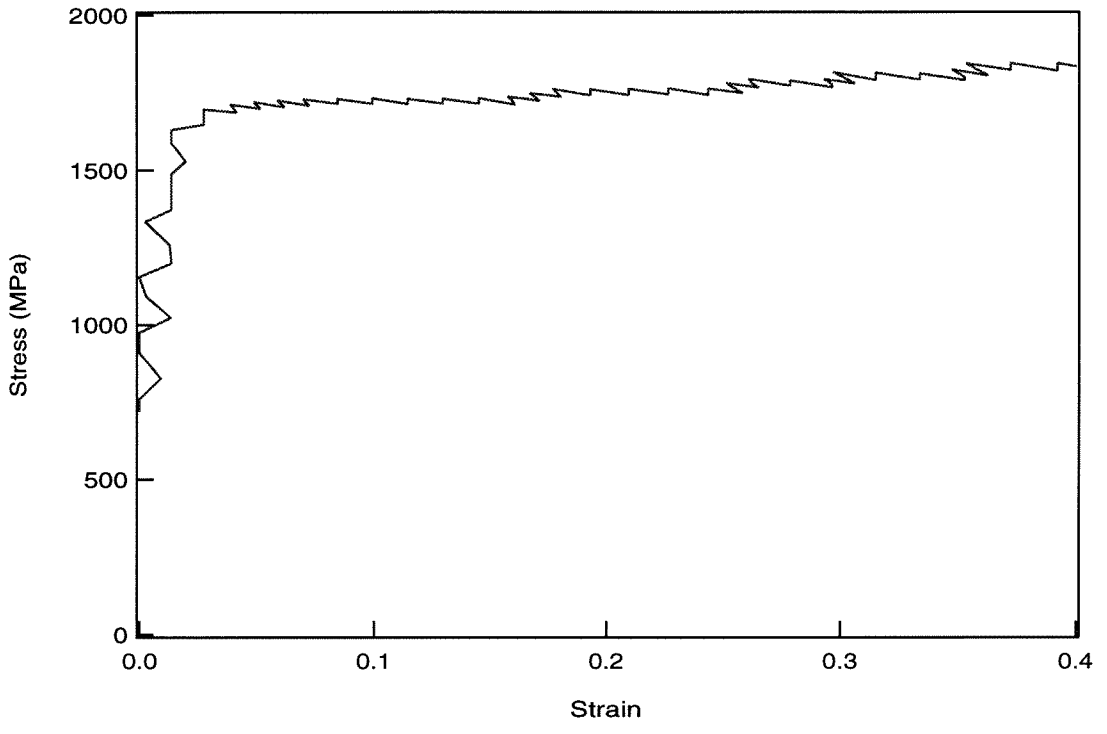

Figure 5.1 Stress-strain curve of 215 nm 304 stainless steel during compressive deformation at room temperature and nominal strain rate of 4.0×10^{-3} sec^{-1}.

2000 nm) is plotted against d^{-1}, $d^{-\frac{1}{2}}$, $d^{-0.417}$, and $d^{-\frac{1}{3}}$ in Figure 5.4, where d represents the grain size. A reasonably good fit was obtained between σ_y and d^{-1}, $d^{-\frac{1}{2}}$ or $d^{-\frac{1}{3}}$ and the best linear fit was obtained between σ_y and $d^{-0.417}$.

The behavior of annealed SS8 plate in tension was as expected. The sample yielded at $\approx$ 1600 MPa and started to neck immediately. This type of behavior is expected from a material whose stress strain curve is elastic-perfectly plastic.

5.4 DISSUSSION

5.4.1 Hall-Petch Hardening in Ultrafine Grain 304 Stainless Steel

It is clear from Figure 5.4 that almost equally good linear fit can be obtained between σ_y

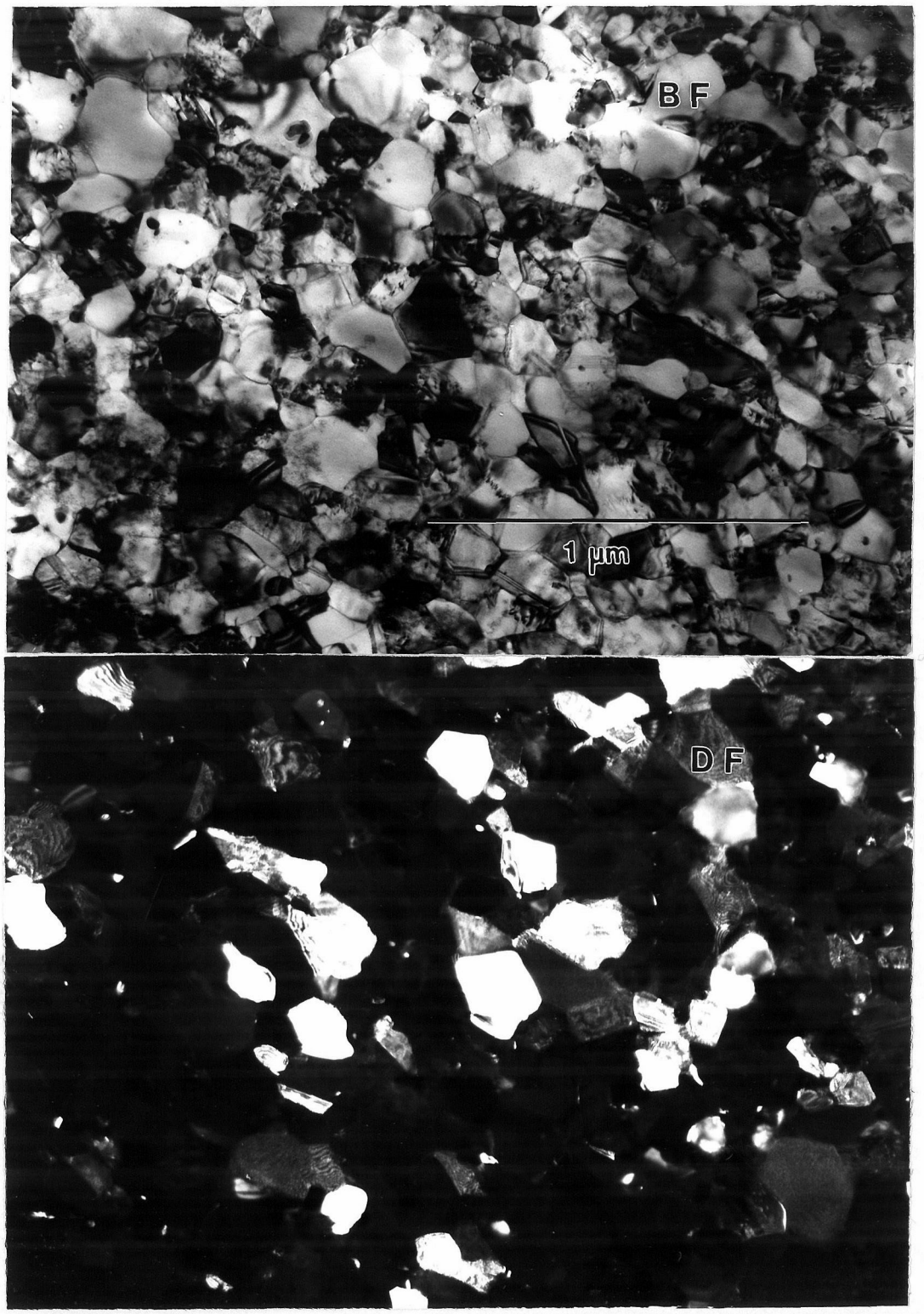

Figure 5.2 Microstructure of 304 stainless steel with the average grain size of ≈ 215 nm.

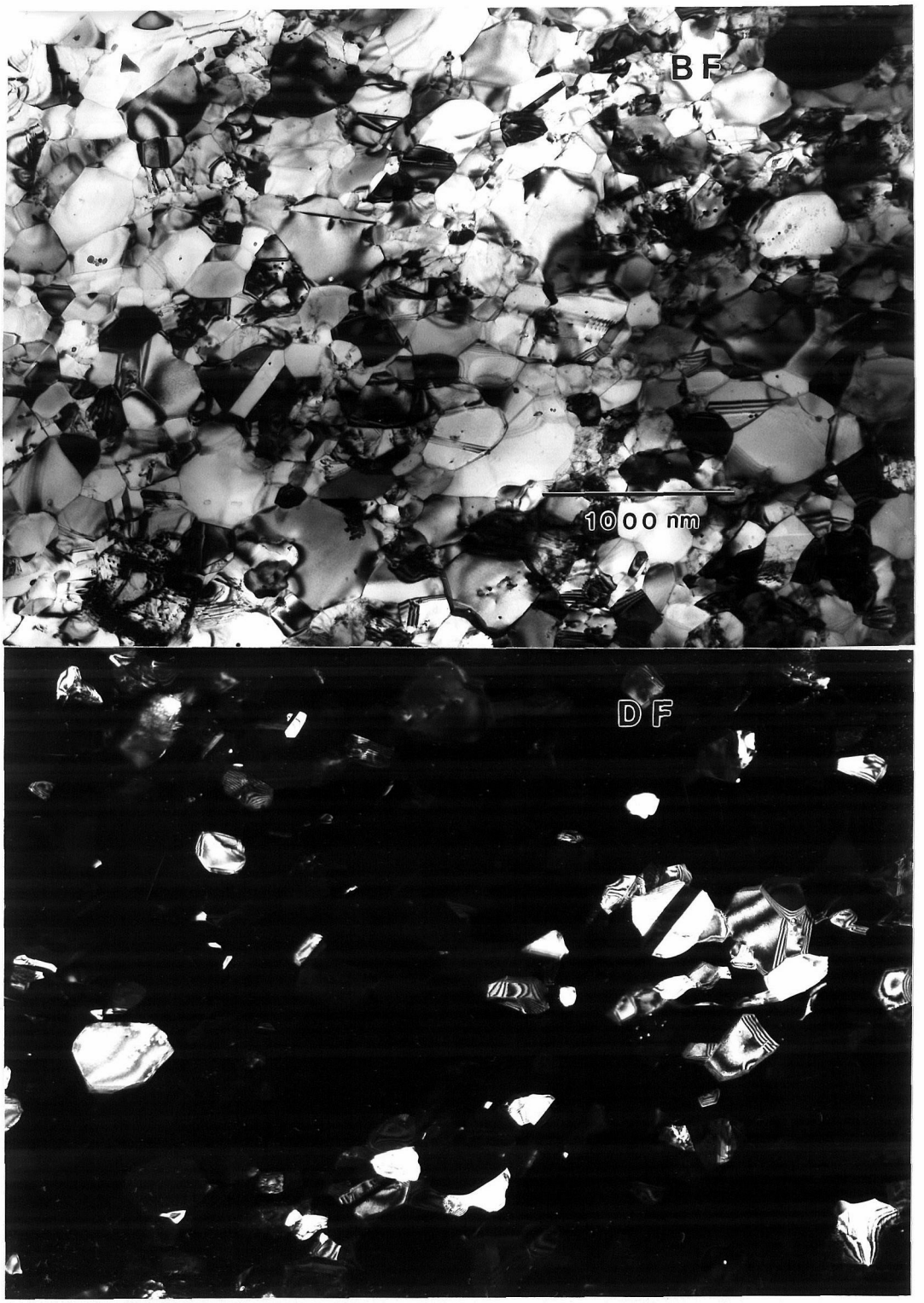

Figure 5.3 Microstructure of 304 stainless steel with the average grain size of ≈ 370 nm.

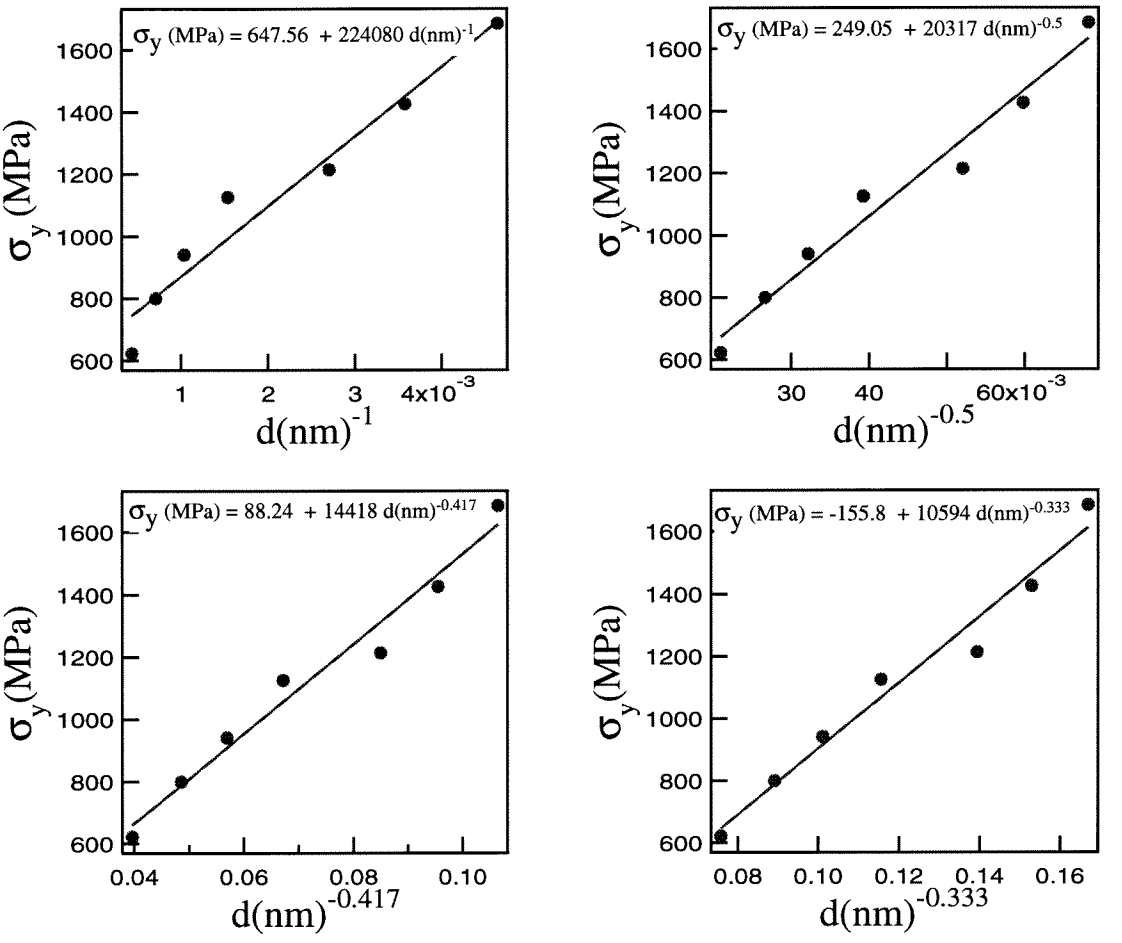

Figure 5.4 Plots of yield stress(σ_y) vs (a) d^{-1}, (b) $d^{-\frac{1}{2}}$, (c) $d^{-0.417}$, and (d) $d^{-\frac{1}{3}}$ for 304 stainless steel for grain sizes ranging from 215 nm to 2000 nm. Note d is average grain size.

and $d^{-\frac{1}{3}}$ or $d^{-0.41}$ as between σ_y and $d^{-\frac{1}{2}}$ or d^{-1} for 304 stainless steel (in the grain size range of 215 nm to 2μm). This is a result of inherent scatter in mechanical property data that makes drawing conclusions about the exact mechanism of grain size hardening a difficult task. Similar observations were made by Baldwin [5] for a variety of other materials. In most of the studies the yield strength data is plotted for a limited range of grain size. Christman [21] has suggested that plotting of grain size hardening data

over a larger range of grain size can provide deeper insight into grain size hardeening mechanisms.

Hence, the yield strength data of Ulvan and Koursaris [21] for 304 stainless steel along with data from the present investigation is plotted against $d^{-\frac{1}{3}}$, $d^{-0.4247}$, $d^{-\frac{1}{2}}$ and d^{-1} in Figure 5.5. This gives us hardening data for 304 stainless steel over a wide range of grain sizes i.e., from 200 nm to 200μm. It is clear from Figure 5.5 that σ_y does not exhibit a linear dependece with d^{-1}, while a reasonably good linear fit can be obtained between σ_y and $d^{-\frac{1}{3}}$, or $d^{-\frac{1}{2}}$. This is helpful as it eliminates the possibility that Bragg hardening law governs the grain size hardening behavior of 304 stainless steel. However, there is still significant scatter in the data to justify inverse square root or inverse cube root dependence of yield stress on the grain size.

The best linear fit for the combined data (i.e., our's and that of Ulvan and Koursaris [21]) was obtained between σ_y and $d^{-0.4247}$. In comparison, the best linear fit for our data only was obtained between σ_y and $d^{-0.417}$. The significance of a grain size exponent $\approx$ 0.42 is not clear, because no existing hardening mechanism predicts an exponent of 0.42. However, this grain size exponent is close to both $\frac{1}{3}$ and $\frac{1}{2}$ and several existing grain size hardening mechanisms predict these exponents. Christman [21] has observed (over a broad range of grain sizes) that fcc metals exhibit a grain size exponent close to $\frac{1}{3}$, while bcc metals exhibit a grain size exponent close to 0.55. It is noteworthy that the grain size exponent for 304 stainless steel (n = -0.4247) lies between -0.33 and -0.55. It is not clear whether this is related to the fact that 304 stainless steel used in the present investigation was a mixture of bcc and fcc phases.

As mentioned previously, several authors have observed a decrease in slope (hardening coefficient) of HPR at room temperature for grain sizes below 1μm. Although, the exact mechanism of grain size hardening in 304 stainless steel could not be determined from

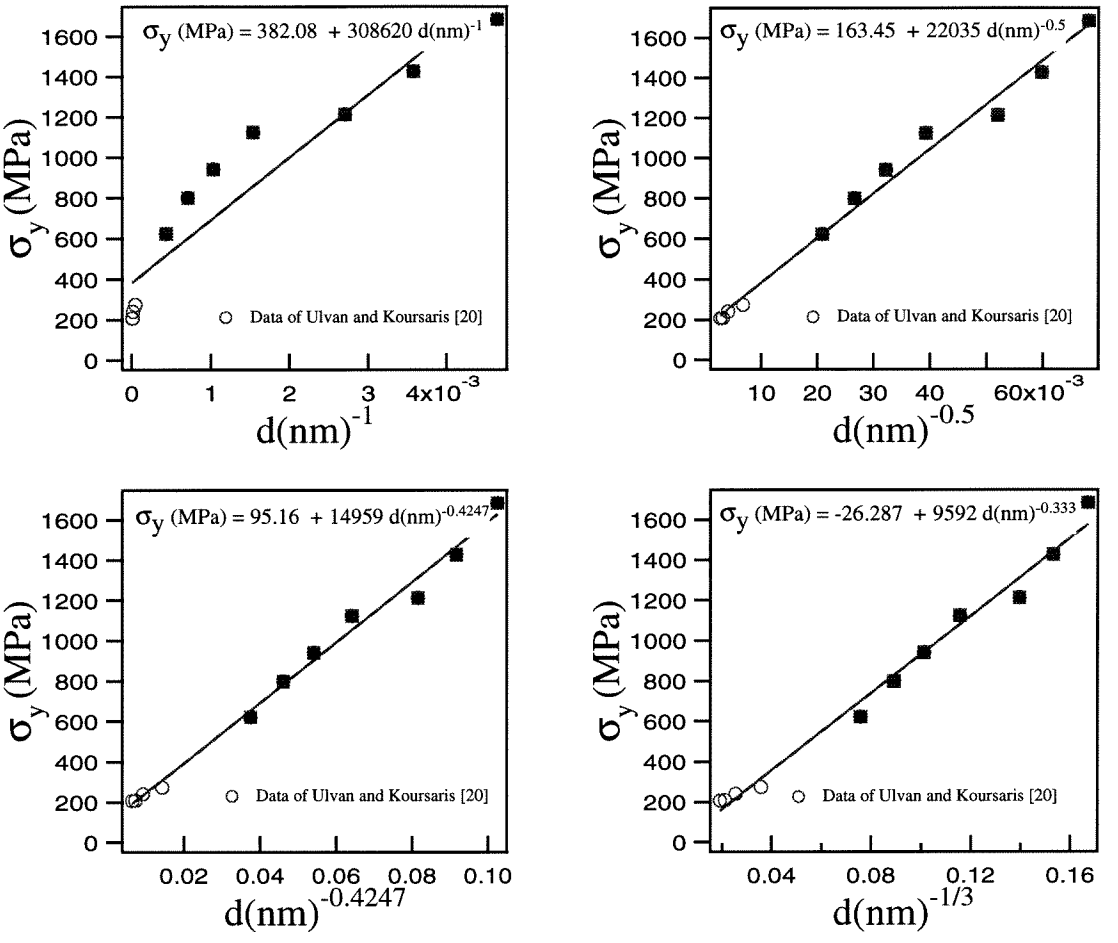

Figure 5.5 Plots of yield stress(σ_y) vs (a) d^{-1}, (b) $d^{-\frac{1}{2}}$, (c) $d^{-0.4247}$, and (d) $d^{-\frac{1}{3}}$ for 304 stainless steel for grain sizes ranging from 215 nm to 200 μm. Note d is average grain size.

the present investigation, it is clear from the plots of σ_y and $d^{-\frac{1}{3}}$, and σ_y and $d^{-\frac{1}{2}}$ that the hardening coefficients (slope of the straight line) do not change over the entire range of grain size (i.e., from 2μm to 200 nm). Two possible explanations can be proposed to explain this behavior: (i) the materials (i.e., Al and Mg alloys) in which a decrease in slope of HPR is observed are fairly low melting point alloys [6,7]. For magnesium, room temperature corresponds to an homologous temperature of $0.32T_M$, while for 304 stain-

less steel, room temperature corresponds to significantly lower homologous temperature of $0.175T_M$. Hence simultaneous operation of diffusive mechanisms such as accelerated absorption of lattice dislocations by the grain boundaries (suggested by Valiev et al. [6]) that may be responsible for decrease in slope of HPR in the magnesium alloy at room temperature may not be able to operate in 304 stainless steel of comparable grain size, consequently the change in slope of HPR will not be observed in 304 stainless steel until much finer grain sizes at room temperature; (ii) while, Christman [21] has showed for the Valiev et al. data from Mg alloy (for which decrease in hardening coefficient is observed at lower grain sizes) that σ_y exhibits a linear dependence with $d^{-\frac{1}{3}}$ over the entire grain size range and he therefore questions applicability of HPR to this alloy.

The absence of strain hardening in 215 nm 304 stainless steel is quite typical of ultrafine grain and nanophase materials and is observed by several authors [6,23]. One aspect of this investigation that remains puzzling is why the peak strength of 215 nm steel (in this case also yield strength) is lower than the peak strength for coarse grained (grain size 150μm) steel. More research into mechanisms of strain hardening are needed to resolve this issue.

5.5 CONCLUSION

The mechanism of grain size hardening in 304 stainless steel could not be conclusively identified from the present investigation. A reasonably good linear fit was obtained between σ_y and $d^{-\frac{1}{3}}$ or $d^{-\frac{1}{2}}$ over the grain size range of 200 nm to 200μm. Furthermore, there was no evidence of change in hardening slope (over the entire range of grain size i.e., 200 nm to 200μm) for inverse square root as well as cube root dependence of yield strength on grain size. The best fit between σ_y and d^{-n} in 304 stainless steel was obtained for n = 0.4247.

References:

[1] R. W. Armstrong, Met. Trans. 1, 1170 (1970)

[2] E. O. Hall, Proc. Phys. Soc. London B64, 747 (1951).

[3] N. J. Petch, J. Iron Steel Inst. 174, 25 (1953).

[4] A. H. Cottrell, The Mechanical Properties of Matter, John Wiley & Sons, New York, NY, 282 (1964).

[5] W. M. Baldwin Jr., Acta Met. 6, 139 (1958).

[6] R. Z. Valiev, N. A. Krasilnikov and N. K. Tsenev, Mat. Sc. Engng. A137, 35 (1991).

[7] R. Z. Valiev, F. Chmelik, F. Bordeaux, G. Kapelski and B. Baudelet, Scripta Met. 27, 855 (1992).

[8] A. H. Chokshi, A. Rosen, J. Karch and H. Gleiter, Scripta Met. 23, 1679 (1989).

[9] H. Chang, H. J. Hofler, C. J. Altstetter and R. S. Averback, Scripta Met. 25, 1161 (1991).

[10] K. Lu, W. D. Wei, and J. T. Wang, Scripta Met. 24, 2319 (1990).

[11] G. W. Nieman, J. R. Weertman and R. W. Siegel, Scripta Met. 23, 2013 (1989).

[12] G. D. Hughes, S. D. Smith, C. S. Pande, H. R. Johnson and R. W. Armstrong, Scripta Met. 20, 93 (1986).

[13] J. S. C. Jang and C. C. Koch, Scripta Met. 24, 1599 (1990).

[14] S. K. Ganapathi and D. A. Rigney, Scripta Met. 24, 1675 (1990).

[15] R. W. Armstrong, Y. T. Chou, R. M. Fischer and N. Louat, Phil. Mag. , 943 (1966).

[16] T. G. Nieh and J. Wadsworth, Scripta Met. 25, 955 (1991).

[17] J. R. Weertman, Mat. Sc. Engng. A166, 161 (1993).

[18] K. Lu and M. L. Sui, Scripta Met. 28, 1465 (1993).

[19] G. E. Fougere, J. R. Weertman, R. W. Siegel and S. Kim, Scripta Met. 26, 1879 (1992).

[20] G. E. Dieter, Mechanical Metallurgy, 2nd edition, p. 197, McGraw Hill (1976).

[21] T. Christman, Scripta Met. 28, 1495 (1993).

[22] E. Ulvan and A. Koursaris, Met. Trans. 19A, 2287 (1988).

[23] M. Jain and T. Christman, Acta Met. 42, 1901 (1994).

CHAPTER VI

Future Work and Remaining Issues

The high ductility of nanocrystalline Fe-28Al-2Cr in compression is promising. However, this is of limited technological importance until the ductility can be acheived in tension. The lack of tensile ductility in nanocrystalline Fe-28Al-2Cr was attributed to the limitations of the powder consolidation technique (particularly the presence of inter-particle boundaries). Therefore, it would be of interest to explore whether the inter-particle boundaries can be effectively broken by post consolidation processing (e.g., extrusion etc.) to yield higher strength and/or ductility in tension. The issue of inter-particle boundaries can be completely avoided by producing nanocrystalline Fe-28Al-2Cr by wrought processing. Our preliminary work in this regard appears promising as we were able to obtain $\approx$100nm microstructure in about 40% of the microstructure by recrystallization. The preliminary experimental trends suggest that the volume fraction of this microstructure can be increased by introducing more deformation at lower temperatures (below RT) prior to annealing. These experiments could not be completed due to the restriction on the size of sample that could be rolled by the rolling mill available to us. However, this problem can be overcome quite easily and it would be worthwhile to explore whether the volume fraction of $\approx$ 100 nm microstructure could be increased close to 100%.

The mechanism for grain refinement in 80 nm Fe-28Al-2Cr during compressive deformation is not entirely clear. It is not clear, whether the formation of amorphous phase along the grain boundaries is critical to the refinement of microstructure. Experiments on other material systems are needed to resolve this issue. Our microstructural evidence suggests

that grain boundary sliding plays an important role in the grain refinemnt process. Experimental evidence also suggests that there is a critical grain size below which grain refinement takes place at a certain temperature. More experiments, in particular, carefully designed creep tests combined with microstructural examination are needed to ascertain these hypotheses and completely resolve these issues. The real motivation behind this work is to find out what material systems would exhibit such behavior and whether this refinement mechanism can be used to produced fine nanophase ($\approx$ 10nm) microstructures without powder precursors.

It would also be of interest to explore whether the processing techniques to produce 200 nm 304 stainless steel can be applied to other materials to obtain ultrafine microstructures. A few obvious candidates for this investigation would be other 300 series stainless steels, as most of these steels undergo deformation induced martensitic phase transformation. Ability to produce ultrafine cell structures is critical for the success of this processing technique. Our experiments also suggest that microstructural details of dislocation cells (such as average misorientation among the cells, sharpness of cell boundaries, stacking fault energy, etc.) play a crucial role towards the success of this processing technique. A better understanding of the impact of these microstructural details would significantly aid the identification of other material systems that can undergo microstructural refinement by this processing technique.

A detailed knowledge of the mechanical properties would be useful in ascertaining the real technological importance of this ultrafine grain 304 stainless steel. Properties of particular interest are cryogenic and room temperature fracture toughnesses, cryogenic temperature strength and ductility, room temperature formability, etc. It would also be worthwile exploring whether this steel exhibits superplasticity. This steel fulfills several important prerequisites for superplasticity. Our experiments indicate that superplasticity is

not expected in 304 stainless steel until 550°C (because the stress exponent is too high ≈ 6), however they do not preclude the possibility of superplasticity at higher temperatures. Creep experiments above 550°C are needed to resolve this issue.